The Crustal Stress Field in Southern California and its Implications for Fault Mechanics

Thesis by

Jeanne L. Hardebeck

In Partial Fulfillment of the Requirements
for the Degree of
Doctor of Philosophy

California Institute of Technology
Pasadena, California

2001
(Submitted 8/10/2000)

Acknowledgements

I would like to thank Egill Hauksson for being an excellent advisor to me throughout my graduate school career. Hiroo Kanamori was also a good advisor, and I thank him for numerous interesting discussions about my research. I thank the rest of my thesis committee, Joann Stock, Tom Heaton, and Mike Gurnis, for their many helpful comments on my work. Everyone in the Seismo Lab community contributed to an open and intellectually stimulating environment which I greatly enjoyed. Special thanks to: Don Anderson, Magali Billen, Emily Brodsky, Rob Clayton, Jishu Deng, Jane Dmochowski, Sue Hough, Ken Hudnut, Miriam Jackson, Chen Ji, Lucy Jones, Sharon Kedar, Tim Melbourne, Rosemary Miller, Julie Nazareth, Mark Simons, Eh Tan, Anu Venkataraman, and David Wald. I thank Ellen and Harry Hardebeck, Christopher Campbell, Aife, Sid, and Jane for all the emotional support they have given me.

Abstract

A high-resolution image of crustal stress orientation, determined from the inversion of earthquake focal mechanisms, provides insights into the mechanics and evolution of faulting in southern California. The plate boundary region is a wide, complex zone of deformation, and the stress field also appears to be spatially heterogeneous. Temporal variations in stress orientation are observed as well. The observed stress rotations due to the 1992 Landers earthquake are used to make an order of magnitude estimate of the deviatoric stress magnitude at seismogenic depths. The inferred deviatoric stress is on the order of 100 bar, an order of magnitude less than the fault strength predicted from laboratory experiments, implying that active faults in southern California are weak. The San Andreas Fault does not appear to be weaker than other faults, as it is well-oriented for failure in the stress field of its immediate surroundings. Earthquakes both modify and respond to the stress field. The 1992 Landers and 1994 Northridge earthquakes caused observable rotations of the stress axes, and the mainshock-induced static stress changes appear to have triggered some aftershocks. The number of aftershocks consistent with static stress triggering in each sequence is significantly greater than the number that would be expected to appear consistent by chance. Since small earthquakes are a response to the stress field, one might expect their stress drops to scale with effective normal stress. However, the stress drops of a set of small events do not appear to scale with depth, and therefore normal stress, in most of the seismogenic crust.

Contents

List of Figures

List of Tables

Summary

The stress in the Earth's crust is an important part of earthquake physics, as earthquakes both respond to and modify the stress field. In this thesis, I determine stress orientations in southern California at high spatial resolution, and make an order of magnitude estimate of the deviatoric stress magnitude at seismogenic depths. I study the impact of faulting on the stress field by observing the rotation of the principal stress axes due to major earthquakes, and explore the effects of stress on faulting by looking for correlations between stress magnitude and earthquake stress drop and between mainshock-induced stress changes and aftershock triggering.

In Chapter 1, a high-resolution image of the orientations of the principal stress axes at seismogenic depths is found from the inversion of earthquake focal mechanisms (Appendix A explains and verifies the inversion technique.) The stress field appears to be very spatially heterogeneous, implying that the complexity of faulting in southern California is not simply the response of a heterogeneous crust to a homogeneous stress field. The heterogeneous stress field may both promote and be promoted by complex faulting. Temporal variations in stress orientation are also observed, and are dominated by stress rotations caused by major earthquakes. Tectonic loading of faults is too gradual to be detected with the ~20 years of data used in this study.

The observed stress rotations due to major earthquakes can be used to estimate the magnitude of the deviatoric stress. This is because the rotation is controlled by the ratio of the magnitude of the stress change caused by the earthquake to the magnitude of the deviatoric stress, as well as the relative orientation of the two stress tensors. In Chapter 2, I estimate the deviatoric stress at seismogenic depths in southern California to be on the order of 100 bar. Laboratory experiments predict fault strength to be on the order of 1 kbar, so the active faults in southern California must be weak if they operate at shear stresses of ~100 bar.

The major fault in southern California, the San Andreas, appears to be of similar

strength to other faults in the region. Previous work found that the San Andreas is at high angle to the regional compressive stress axis, implying that relatively little shear stress is resolved on the fault, and that it must be weak relative to other faults. In Chapter 3, however, I find that within ~2-30 km of the San Andreas in southern California, the compressive stress axis is $\sim 45^{o}$ to the fault. This indicates that the San Andreas is not weak in a relative sense. It may still be weak in an absolute sense, as the results of Chapter 2 suggest that most active faults in southern California are weak.

In Chapter 4, I investigate the relationship between earthquake static stress drop and the effective normal stress on the fault. A simple model of fault friction predicts that maximum static stress drop should scale linearly with effective normal stress, and therefore depth, assuming hydrostatic pore pressure. The maximum observed stress drops of small aftershocks scale approximately linearly with depth in the upper 5 km. Below 5 km depth, however, there is no increase in maximum observed stress drop with depth, indicating that either the simple friction model or the assumption of hydrostatic pore pressure does not hold at seismogenic depths. This suggests that faults are weak due to either dynamic friction drop or high pore fluid pressure.

In Chapter 5, I quantitatively test the hypothesis that aftershock sequences are triggered by the static stress changes due to the mainshock. Static stress changes appear to play a role in triggering, as the number of aftershocks consistent with static stress triggering is significantly greater than the number that would be expected to appear consistent purely by chance. The model works best for stress changes between 0.1 bar and 100 bar. Since many aftershocks are not explained by static stress changes, however, other mechanisms must also contribute to the triggering of aftershocks.

Chapter 1 Stress Orientation in Southern California

1.1 Introduction

The boundary between the Pacific and North American plates in southern California is a >100 km wide zone of complex deformation. The right-lateral, strike-slip San Andreas is the major fault, but there are many other important strike-slip, reverse and normal faults (Figure 1.1). Knowledge of the forces acting on this system is necessary to understand the mechanics of its deformation. Therefore, it is important to determine the state of stress in the crust. Of particular interest is whether the stress field is as spatially complex as the faulting, or whether the stress field is relatively homogeneous and the complexity of deformation derives from the heterogeneity of crustal structure.

Numerous borehole stress measurements have been made in southern California at shallow ($\leq$3.5 km) depths [*Hickman et al.*, 1988; *Stock and Healy*, 1988; *Shamir and Zoback*, 1992; *Zoback and Healy*, 1992; *Zoback*, 1992; *Kerkela and Stock*, 1996; *Wilde and Stock*, 1997]. Stress orientations at seismogenic ($\leq$15-25 km) depths have been determined from inversions of earthquake focal mechanisms [*Michael*, 1987b; *Jones*, 1988; *Hauksson*, 1990, 1994; *Hartse et al.*, 1994; *Wyss and Lu*, 1995; *Castillo and Zoback*, 1995; *Zhao et al.*, 1997; *Abers and Gephart*, 1997]. However, since most of these studies focus on an earthquake sequence or a major fault, the spatial coverage of southern California is incomplete.

The goal of this chapter is to determine stress orientations at seismogenic depths over the entire southern California plate boundary region using a uniform methodology. Because of the high seismicity rates and dense instrumentation in southern California, there are tens of thousands of well-recorded earthquakes which can be

used to infer stress orientation, and most seismically active regions can be studied with a spatial resolution of 5-20 km.

The resulting model of stress orientation can then be used to study the mechanics and evolution of faulting in southern California. Stress field patterns can indicate whether earthquakes are responding to a heterogeneous or generally homogeneous stress field. Temporal changes in stress orientation provide information about how stress evolves through time and how faulting affects the stress field. Stress rotations caused by major earthquakes can also be used to estimate the magnitude of deviatoric stress at seismogenic depths (Chapter 2). Stress magnitude and orientation are important for earthquake physics because they constrain the absolute and relative magnitude of stress on active faults (Chapter 2, Chapter 3).

1.2 Data and Method

The data set consists of ~50,000 earthquakes recorded by the Southern California Seismic Network (SCSN) between January 1, 1981, and December 31, 1999 (Figure 1.2). Events from the 1975 Galway Lake and 1979 Homestead Valley sequences are also included. The events were relocated by Egill Hauksson using a three-dimensional seismic velocity model [*Hauksson*, 2000]. Focal mechanisms were determined from the SCSN first-motion data and the recomputed takeoff angles, using the FPFIT software package [*Reasenberg and Oppenheimer*, 1985]. All events have location uncertainties of $\leq$1 km, $\geq$12 first-motion picks, and maximum azimuthal gap $\leq 135^o$.

Inversions for stress orientation are performed at points on a three-dimensional grid with 5 km spacing. An inversion includes all events within 5 km of the point if there are $\geq$50 such events. Otherwise, the 50 events closest to the grid point are used. Clearly, the spatial resolution will vary with seismicity rate. The spatial resolution is quantified by defining the 1σ level of spatial uncertainty to be the root-mean-square distance of the events used in the inversion.

The earthquake focal mechanisms are inverted for stress using the method developed by *Michael* [1984, 1987b]. The inversion returns the orientation of the 3

principal stress axes and a measure of their relative magnitude; or, equivalently, a normalized deviatoric stress tensor. The absolute stress magnitudes are not found because the inversion uses only geometrical information. Appendix A demonstrates that this inversion method produces accurate stress orientations with reasonable uncertainty estimates.

A variation of the relative magnitude parameter, A_ϕ, indicating which principal stress is most vertical, was introduced by *Simpson* [1997]. If the maximum principal stress, σ_1, is vertical, $0< A_\phi <1$; if the intermediate principal stress, σ_2, is vertical, $1< A_\phi <2$; and if the least principal stress, σ_3, is vertical, $2< A_\phi <3$. Vertical σ_1 corresponds to a normal faulting regime, vertical σ_2 to a strike-slip regime, and vertical σ_3 to a thrust faulting regime [*Anderson*, 1951].

1.3 Observations

The maximum horizontal stress direction and A_ϕ in southern California are shown in Figure 1.3, Figure 1.4 and Figure 1.5. Results are presented only for locations with spatial uncertainty $\leq$20 km (1σ), and stress orientation uncertainty $\leq 20^o$ (1σ). Most seismically active regions are covered at this level of resolution.

Typically, the intermediate stress axis, σ_2, is most vertical, and the maximum horizontal stress, σ_H, is oriented NNE, consistent with a right-lateral transform plate boundary trending ~N40W. The distribution of σ_H directions is shown in Figure 1.3. The mean orientation is N7E, but the local direction of σ_H varies greatly, from ~N30W to ~N45E. If the orientation of σ_H is not distinguishable from N7E at the 95% confidence level of the inversion, it is shown in Figure 1.4 as N7E. The spatial heterogeneity in stress orientation is therefore statistically significant. There are also regions in which σ_1 or σ_3 is most vertical, consistent with the presence of active normal and thrust faults.

The most vertical stress axis is generally not exactly vertical. The trend and plunge of this axis shows no coherent signals, however, suggesting that the deviation from vertical is due primarily to noise. The most-vertical axis is significantly different

from vertical at the 95% confidence level for less than 1/3 of the inversion results, and these points are spatially scattered.

1.3.1 Transverse Ranges

In the Transverse Ranges, the San Andreas Fault strikes WNW, forming a large-scale contractional bend. The orientation of σ_H in the Transverse Ranges is typically ~N7E. Near Tejon Pass and in the San Bernardino Mountains, σ_H trends NNW, and north of Los Angeles, there is a region of NNE orientation. West of Cajon Pass, σ_3 is often vertical, consistent with mapped thrust faults and uplift of the ranges. The observed region of vertical σ_3 is predominately on the Pacific Plate side, mirroring the asymmetry of the deformation.

In the Cajon Pass region, there is a local σ_1-vertical stress regime. *Jones* [1988] also observed normal faulting near Cajon Pass, and attributed this extension to an unstable triple junction where the San Jacinto Fault obliquely joins the San Andreas. *Jones* [1988] also speculates that the rupture of the 1857 M≈8 earthquake on the San Andreas may have stopped at Cajon Pass due to the change in stress state, as a fault in a normal faulting regime should be at lower stress than a fault in a strike-slip regime, and therefore less capable of propagating earthquake rupture. The stress observations are consistent with the presence of normal faults near Cajon Pass [*Weldon and Springer*, 1988].

Stress orientations observed at 3.5 km depth in the Cajon Pass borehole appear to imply left-lateral shear stress on the San Andreas [*Shamir and Zoback*, 1992; *Zoback and Healy*, 1992]. However, I do not observe left-lateral orientations. A shear-wave splitting study indicates that the observed left-lateral stress orientations are local to the upper few km of the borehole site [*Liu et al.*, 1997]. Figure 1.4 and Figure 1.5 show that the stress state along the San Andreas changes abruptly near Cajon Pass, which may result in local stress anomalies such as that observed in the borehole.

In the Transverse Ranges east of Cajon Pass, σ_2 is generally vertical. Although the steep topography of the San Bernardino Mountains implies recent uplift, the observed

faulting regime is primarily strike-slip. Focal mechanism studies by *Hauksson* [1994] and *Unruh et al.* [1996] also observed a strike-slip regime. The most recent major earthquake in the San Bernardino Mountains, the M6.2 1992 Big Bear event, was strike-slip [*Hauksson et al.*, 1993]. This suggests that the oblique convergence across the San Bernardinos is partitioned into strike-slip and thrust earthquakes. The thrust faults along the northern boundary of the mountains strike approximately perpendicular to the σ_H direction, so they may fail in thrust events even though the stress regime is strike-slip.

1.3.2 Eastern California Shear Zone

The Eastern California Shear Zone (ECSZ) is a zone of strike-slip faulting east of the San Andreas, which takes up ~15% of the relative plate motion [*Dokka and Travis*, 1990]. The ECSZ south of the Garlock Fault has a distinct stress state, with σ_H oriented ~N20-45E. The NNE orientation of σ_H was previously observed by *Hauksson* [1994], and the kinematic axis of maximum shortening is also oriented NNE [*Johnson et al.*, 1994; *Unruh et al.*, 1996; *Shen-Tu et al.*, 1998]. North of the Garlock Fault, this orientation continues only in a narrow zone along the eastern edge of the Sierra Nevada Mountains. The σ_2 axis is vertical throughout most of the ECSZ, although patches of σ_1-vertical stress regime appear, especially in the southeastern portion.

The 1992 M7.3 Landers earthquake [*Sieh et al.*, 1993], a right-lateral strike-slip event in the ECSZ, caused a clockwise rotation of σ_H in most of the crust surrounding the rupture (Figure 1.6). East of the northern portion of the rupture, however, the σ_H axis rotated counterclockwise. The general clockwise rotation is consistent with the observations of *Hauksson* [1994]. *Hauksson* [1994] also observed that the northern part of the rupture zone after the event couldn't be fit by a single stress tensor, consistent with the large variations in orientation over short distances and the difference in rotation direction on the two sides of the fault observed here. *Hauksson* [1994] concluded from the heterogeneous stress orientation that the northern portion of the Landers rupture experienced complete stress drop. The stress orientations

found here are also consistent with this conclusion, as they imply little resolved shear stress.

The Landers earthquake also caused some changes in the style of faulting. Before the event, the region was predominately strike-slip. After the earthquake, local thrusting and normal faulting regimes appear to the NW and SW of the rupture, respectively, consistent with the static stress changes due to a right-lateral dislocation in an elastic medium [*King et al.*, 1994]. A localized patch of normal faulting also appears to the SE of the rupture, however, inconsistent with the elastic dislocation model. Additionally, the Landers earthquake shut off an area of thrust faulting at the junction of the Pinto Mountain Fault with the San Andreas, near the location of the oblique-thrust 1986 M5.9 North Palm Springs earthquake [*Jones et al.*, 1986]. Inspection of the focal mechanisms shows that the change in faulting style from thrust to strike-slip occurred at the time of the Landers mainshock.

The Landers earthquake ruptured parts of five faults and changed strike by $\sim 35^o$ along its length [*Sieh et al.*, 1993]. In the south, where rupture initiated, the surface trace cuts across the predominate fault fabric of the ECSZ, while the northern portion of the rupture bends to follow it. *Nur et al.* [1993] observed that the faults in the ECSZ are poorly oriented for failure in the current stress state, and proposed that the southern Landers rupture, and several other ECSZ earthquakes, represent a new fault trend at a more favorable orientation.

The observed pre-event stress state confirms that for the southern portion of the rupture, the mapped faults are poorly oriented for failure, $\sim 70^o$-80^o from σ_H, while the southern Landers rupture is oriented $\sim 30^o$-40^o from σ_H, optimal for failure. However, in the northern portion of the rupture area, σ_H trends more northerly and the major mapped faults, which the rupture followed, are $\sim 60^o$ to σ_H, adequately oriented for failure on preexisting faults.

1.3.3 Southern Sierra Nevada

The Sierra Nevada Mountains and the San Joaquin Valley to the west form a relatively stable microplate. The stress regime in the southern Sierra Nevada is predominately σ_1-vertical with $\sigma_2 \approx \sigma_3$. The wide variation in orientation of σ_H in this area is an artifact of the horizontal stresses being of similar magnitude. This stress state is consistent with a high mountain range in which the stress state is primarily controlled by the excess overburden pressure.

Another σ_1-vertical zone, much of which is also pure dilatation, occurs along the Garlock fault to the southeast of the Sierra Nevada. This extension is due to a left step in the left-lateral Garlock Fault, where the Fremont Valley is being down-dropped. I also observe a change in stress orientation along the southern Garlock Fault, with NW σ_H orientations south of the Sierras changing to NE orientations near the intersection with the San Andreas Fault.

Spatial stress variations in the Tehachapi Mountains and the southern San Joaquin Valley may be related to the 1952 M7.7 earthquake on the White Wolf Fault [*Ellsworth*, 1990]. *Castillo and Zoback* [1995] studied the state of stress along the White Wolf Fault, and identified two clusters of seismicity: one to the southwest with σ_H at ~N25E, and one to the northeast with σ_H at ~N10E. In contrast, I observe σ_H to be indistinguishable from N7E in the southwest, and at ~N20W in the northeast. Additionally, *Castillo and Zoback* [1995] observed a strike-slip regime everywhere, while I observe a thrust regime in the southwest. The 1952 mainshock was left-lateral with a significant thrust component [*Stein and Thatcher*, 1981; *Bawden*, 2000], so a mix of stress regimes is not unexpected.

The Basin and Range extensional province begins east of the Sierra Nevada. The stress orientations east of the Sierras are primarily strike-slip, with a few σ_1-vertical zones. *Bellier and Zoback* [1995] also observed that the stress regime in the western Basin and Range is currently predominately strike-slip. The mix of strike-slip and normal faulting regimes is consistent with the oblique extension observed in the region [*Hearn and Humphreys*, 1998].

As mentioned previously, the eastern edge of the Sierra Nevada is also a zone of rotated stress, with σ_H oriented ~N20-45E. This stress orientation makes the ~N striking faults well-oriented for strike-slip failure. In contrast, σ_H trends ~N to the east and west of this zone, indicating that right-lateral faulting on ~N-striking faults is localized to the eastern edge of the Sierras. The Indian Wells Valley and southern Owens Valley may be a region of weak lithosphere, relative to the mountain ranges to the east and west, which concentrates tectonic strain and localizes the associated shear stress.

1.3.4 Greater Los Angeles Area

The greater Los Angeles Area is in the southern end of the thrust regime related to the Transverse Ranges. Both σ_2-vertical and σ_3-vertical stress states are observed in the L.A. area, with σ_2-vertical dominating near the surface and σ_3-vertical dominating at depth. *Kerkela and Stock* [1996] observed a strike-slip regime at shallow depths in the San Fernando Valley and reverse faulting at depth, which is a clear feature of my model. *Hauksson* [1990] also observed a mixture of strike-slip and reverse faulting in the L.A. area.

Walls et al. [1998] present a kinematic model, based on geologic and geodetic measurements, in which most of the ~N-S contraction across the L.A. area is balanced by ~E-W extension, and faulting is primarily on conjugate strike-slip faults. *Argus et al.* [1999] present a counter-model, also based on geodetic data, with little E-W extension, and the ~N-S contraction balanced by thrust faulting and crustal thickening. Both models are essentially two-dimensional and assume that the style of faulting at the surface is the same as at depth. The stress field indicates that a three-dimensional model would be more appropriate, in which faulting style may vary with depth.

The σ_H orientation in the L.A. area is predominately indistinguishable from N7E. However, there are regions in which σ_H is oriented ~N25-45E in the San Fernando Valley, the Long Beach area, Santa Monica Bay, and at depth beneath Los Angeles.

Similar orientations were observed by *Hauksson* [1990]. The San Fernando Valley rotation corresponds to the locations of the 1971 M6.5 San Fernando [*Ellsworth*, 1990] and 1994 M6.7 Northridge [*Hauksson et al.*, 1995a] earthquakes, while the Long Beach rotation corresponds to the location of the 1933 M6.3 Long Beach earthquake [*Ellsworth*, 1990].

The thrust-faulting Northridge event altered the stress state in the San Fernando Valley region (Figure 1.7), contributing to the NNE stress orientation. The σ_H orientations before the event were spatially heterogeneous, generally indistinguishable from ~N7E in the mountains north of the earthquake, and ~N25E in the valley to the south. After the mainshock, the σ_H axis rotated clockwise up to $\sim 20^o$ to the southeast of the rupture, where the post-event σ_H direction is ~N25-45E. A few counterclockwise rotations also occurred, such as to the southwest and to the northeast of the mainshock fault plane.

Zhao et al. [1997] observed a counterclockwise rotation of $\sim 20^o$ immediately after the Northrigde earthquake, and a slow return to the original stress orientation. The discrepancy with this study appears to be due to differences in inversion methodology. I obtained a list of the earthquakes used by *Zhao et al.* [1997] (D. Zhao, written communication, 1999), and, using the events from this list for which I could determine quality focal mechanisms (about 90% of the events), attempted to reproduce their results. I used first-motion focal mechanisms found using takeoff angles computed from the seismic velocity models of *Hauksson* [2000] and *Zhao and Kanamori* [1995] (Y. Sugihara, written communication, 1999). In both cases, I observe a clockwise stress rotation at the time of the mainshock, and no return to the pre-mainshock orientation (Figure 1.8.) Since my data set based on the *Zhao and Kanamori* [1995] seismic velocity model should be almost identical to the data set used by *Zhao et al.* [1997], the difference seems to come from the difference in inversion technique. Additionally, Y. Sugihara and I inverted identical data sets and obtained different results. In this case, the difference must be due to the inversion techniques. I use the inversion method of *Michael* [1984, 1987b], whereas *Zhao et al.* [1997] used the inversion method of *Horiuchi et al.* [1995]. Since the method of *Michael* [1984, 1987b] has been shown to

produce accurate results even for very noisy data (Appendix A), it is probable that the Northridge earthquake caused a general clockwise, rather than counterclockwise, stress field rotation.

1.3.5 Peninsular Ranges

The San Jacinto and Elsinore faults, two major strike-slip faults which parallel the San Andreas, cut obliquely through the Peninsular Ranges. The stress state is generally strike-slip with σ_H oriented ~N7E, consistent with right-lateral shear stress resolved on these faults. There are also a number of patches where the σ_H axis is oriented ~N10-30W, most of which are elongate in the direction of the fault strike.

There is an anomalous region near Anza where σ_H trends ~N30E. The anomaly is primarily at shallow depths and corresponds to the Cahuilla cluster of seismicity. *Hartse et al.* [1994] also observed this distinct stress state of the Cahuilla cluster. This stress anomaly is located directly to the west of a slip gap in the San Jacinto Fault, so it may be a signal of a locked patch on the fault. However, it is unclear why σ_H would be approximately perpendicular to a locked segment, as this implies little resolved shear stress on the fault, and a locked segment should have accumulated significant tectonic stress.

The Salton Trough, to the east of the Peninsular Range, has experienced significant extension and crustal thinning [*Fuis and Mooney*, 1990], and current deformation has a very high strain rate [*Johnson et al.*, 1994]. The stress regime is predominately σ_2-vertical, consistent with historical strike-slip earthquakes along the Imperial Fault [*Ellsworth*, 1990]. There is a patch of σ_1-vertical to the east of the Salton Sea, corresponding to an area of pure dilatation observed geodetically by *Johnson et al.* [1994]. Seismicity rates to the east of this area are low, so the eastern extent of this zone cannot be observed using stress orientations inferred from earthquake focal mechanisms.

1.3.6 Temporal Evolution of the Stress Field

Earthquakes and tectonic loading may affect the stress field and may cause temporal changes in stress orientation. To investigate how the stress field in southern California changes through time, I invert for stress during four ~5 year time periods: 1981 through 1985, 1986 through 1990, 1991 through 1994, and 1995 through 1999. The inversions are performed as described before, except only events occurring within the given time period are used.

The distribution of σ_H orientations appears to change over the 19 years of this study (Figure 1.9). In 1981-1985 and 1986-1990, the σ_H direction for the majority of grid points trends between due north and N10E. In 1991-1994 and 1995-1999, σ_H for many points trends between N3W and N7E. The gradual rotation may be related to interseismic stress accumulation, as it is consistent with increasing shear stress on planes parallel to the relative plate motion. In the later time periods, there is also a more pronounced peak at ~N20E. This secondary peak is due to the clockwise rotations caused by the Landers and Northridge earthquakes (Figure 1.6 and Figure 1.7), and increased activity in the ECSZ, where σ_H is typically oriented ~N20E.

The stress rotation between one time period and the next at a given location can be quite large, up to $\sim 20^o$ (Figure 1.10 (A)-(C)). The distribution of rotations is approximately Gaussian, with a mean of $\sim 0^o$ and a standard deviation of $\sim 9^o$, suggesting that much of the variation may be noise. The spatial pattern of stress rotations changes significantly between time intervals, again indicating a large component of noise.

Temporal changes in the trend of σ_H are also studied by fitting a constant rotation rate to the observations for the 4 time intervals (Figure 1.10 (D)). This significantly reduces the scatter of the observations. The standard deviation of the rotation rate distribution is $\sim 0.8^o$/yr, compared to $\sim 9^o$ over ~5 years, or $\sim 2^o$/yr, for the rotations between time intervals.

Many of the regions which exhibit a rotation rate greater than the 2σ level of the distribution ($\sim 1.5^o$/yr) are in the vicinity of major earthquakes: the 1992 Landers

sequence, the 1994 Northridge earthquake, the 1987 Elmore Ranch-Superstition Hills sequence just south of the Salton Sea [*Wald et al.*, 1990], and the 1995 Ridgecrest earthquake sequence [*Hauksson et al.*, 1995b]. Other areas which exhibit high rotation rates are at the southern end of the Elsinore Fault, scattered locations near Cajon Pass, along the Garlock Fault near Tejon Pass, and along the San Andreas north of the Salton Sea.

Rotations associated with the tectonic loading of an individual fault may be difficult to detect given the duration of the study. The most that the σ_H axis could rotate would be from $\sim 90^o$ to the fault immediately following a major earthquake to $\sim 45^o$ by the time of the next event. If σ_H rotates $\sim 45^o$ over ~ 200 years, equivalent to a rate of $\sim 0.2^o$/yr, or $\sim 4^o$ over the duration of this study, the rotation could not be reliably resolved.

1.3.7 Modeling the Temporal Evolution of the Stress Field

The temporal evolution of the stress field is often modeled for use in earthquake stress triggering studies (Chapter 5). This modeling typically includes earthquake-induced stress changes and sometimes tectonic loading. Comparisons between models and observed stress orientations are complicated by the fact that the stress field in seismically active areas is comprised of two parts: the transient seismic cycle stresses due to tectonic loading and earthquake stress release, and the long term stress state on which these are superimposed. Models of stress evolution include only the first part, and assume that the second part is homogeneous.

I compare the stress field observed in southern California with the stress evolution model of *Deng and Sykes* [1997], which includes the cumulative effects of tectonic loading and $M \geq 7$ earthquakes from 1812 to 1992. The tectonic stress accumulation is modeled using virtual negative displacements on all major faults, which is equivalent to assuming that each fault is loaded by aseismic slip on its downward continuation. *Deng and Sykes* [1997] published their results in terms of Coulomb stress changes on planes of a given orientation, but they provided me with the stress change tensors (J.

Deng, written communication, 1999).

Predicted stress orientations in 1812 (Figure 1.11) can be found by subtracting the stress change tensors of *Deng and Sykes* [1997] from the observed stress field for 1992. The differences between Figure 1.11 and Figures 1.4 and 1.5 reflect ~200 years of seismic cycle stress changes due to tectonic loading and earthquake stress release. Along the San Andreas Fault south of Cajon Pass, for instance, σ_H rotated from a high angle to the fault in 1812 to a low angle in 1992, as shear stress built up on the fault due to tectonic loading while none was released in major earthquakes. North of Cajon Pass, however, σ_H is of similar orientation in 1812 and 1992 because the tectonic stress accumulation was approximately balanced by the stress release in the 1812 and 1857 earthquakes.

The similarity between Figure 1.11 and Figures 1.4 and 1.5 implies that most of the major features of the observed stress field are not explained by the model. Either the major features of the stress field today were present prior to 1812, these features derive from seismic-cycle stresses on unmodeled faults, or another process causes stress changes on a ~200 year time scale. In any case, it is clear that the total stress field cannot be modeled from only tectonic loading and major earthquakes, even if the earthquake catalog can be extended back for hundreds of years. It should be understood when using stress evolution models that only the seismic cycle stress changes are modeled, not the entire stress field.

1.4 Discussion

The high-resolution stress orientation model presented in this chapter demonstrates that the stress field in southern California is highly heterogeneous. Some of the stress orientation complexity is related to differences between the major geologic provinces. The distinct stress states of some regions are easily understood in terms of their tectonics. In the western Transverse Ranges, for example, the thrust faulting stress regime is the result of convergence across the large-scale constraining bend in the San Andreas Fault. In other regions, the reason for a distinct stress state is unclear.

In the ECSZ, for instance, σ_H is oriented N20-45E, significantly rotated from the average southern California orientation of N7E. Additional stress field heterogeneity is related to fault complexity, such as step-overs and junctions.

The heterogeneity of the observed stress field implies that the complex crustal deformation in southern California is not simply the response of a heterogeneous crust to a homogeneous stress field. The complexity of faulting may be the result of the heterogeneous stress field, or, since faulting appear to affect stress orientation, it may be a cause. Complex faulting may promote heterogeneous stress, and vice versa.

Major earthquakes appear to have significant impact on stress orientation. Stress perturbations are seen at the locations of the 1933 Long Beach, 1952 Kern County, 1971 San Fernando, 1992 Landers and 1994 Northridge earthquakes. The last two events occurred within the time period of this study, and stress field rotations can be seen by comparing inversions performed on data from time intervals before and after the mainshocks. The fact that earthquake-induced stress changes can rotate the stress field implies that the background deviatoric stress magnitude must be low, on the order of earthquake stress drop. This idea is pursued further in Chapter 2.

On the ~20 year time scale of the data used in this study, major earthquakes appear to be the dominant cause of temporal evolution of the stress field. Over the long term, tectonic loading should approximately cancel out stress changes due to earthquakes. However, since tectonic loading is a much slower process, the stress changes associated with it cannot be observed with only ~20 years of data. Modeling on a ~200 year time scale suggests that many features of the present stress field are not related to the seismic cycle of tectonic loading and earthquake stress release, but instead may be longer-lived.

1.5 Conclusions

A high-resolution model of stress orientation in the southern California plate boundary region was found from the inversion of earthquake focal mechanisms. The observed stress field is highly heterogeneous, with variations related to differences be-

tween geologic provinces, fault complexity, and major earthquakes. Temporal changes in stress orientation were also detected, primarily related to earthquake-induced stress changes.

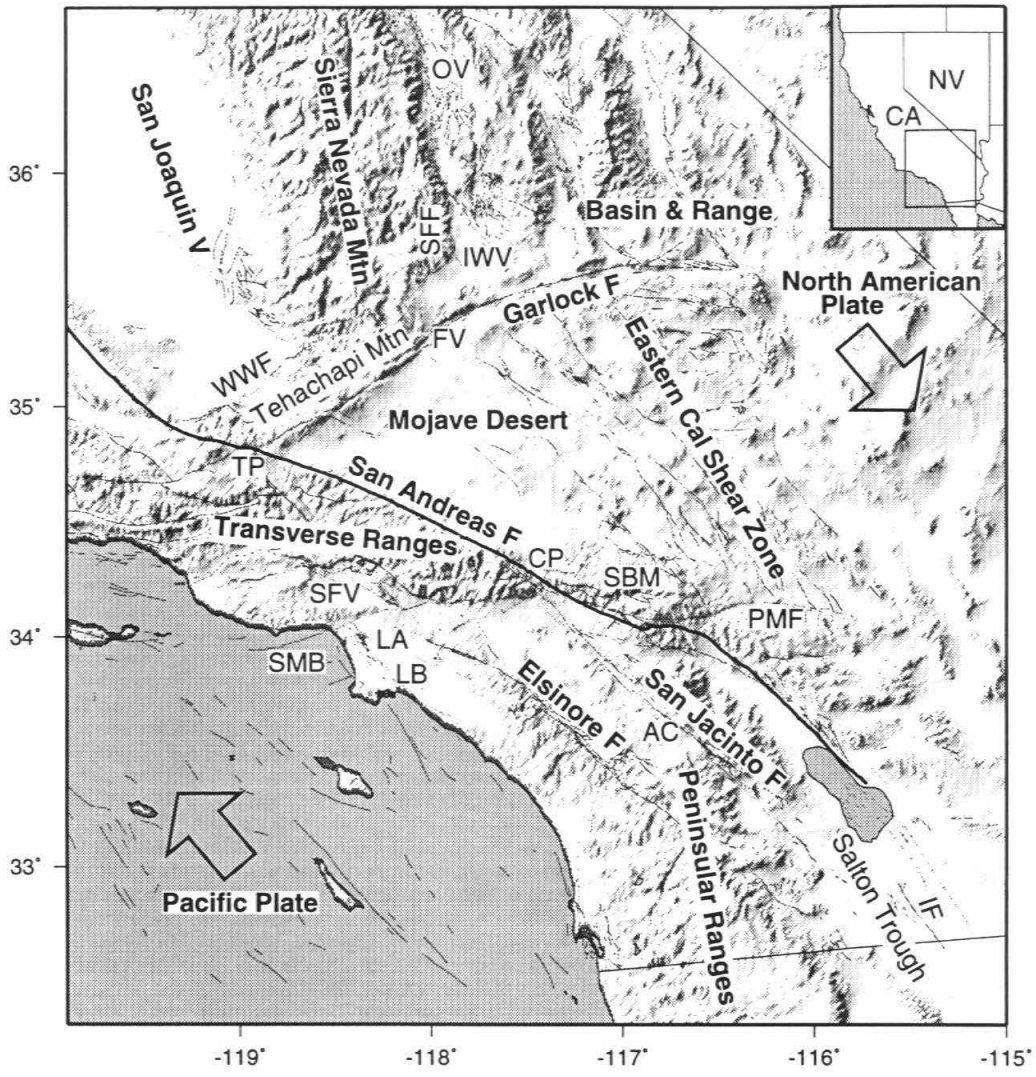

Figure 1.1: Shaded relief map of southern California. Mapped surface traces of faults, from *Jennings* [1975], are shown as thin black lines, the San Andreas Fault as a thick black line. The arrows indicate the approximate direction of relative motion of the Pacific and North American plates. AC, Anza-Cahuilla region; CP, Cajon Pass; FV, Fremont Valley; IF, Imperial Fault; IWV, Indian Wells Valley; LA, Los Angeles; LB, Long Beach; OV, Owens Valley; PMF, Pinto Mountain Fault; SBM, San Bernardino Mountains; SFF, Sierra Frontal Fault; SFV, San Fernando Valley; SMB, Santa Monica Bay; TP, Tejon Pass; WWF, White Wolf Fault.

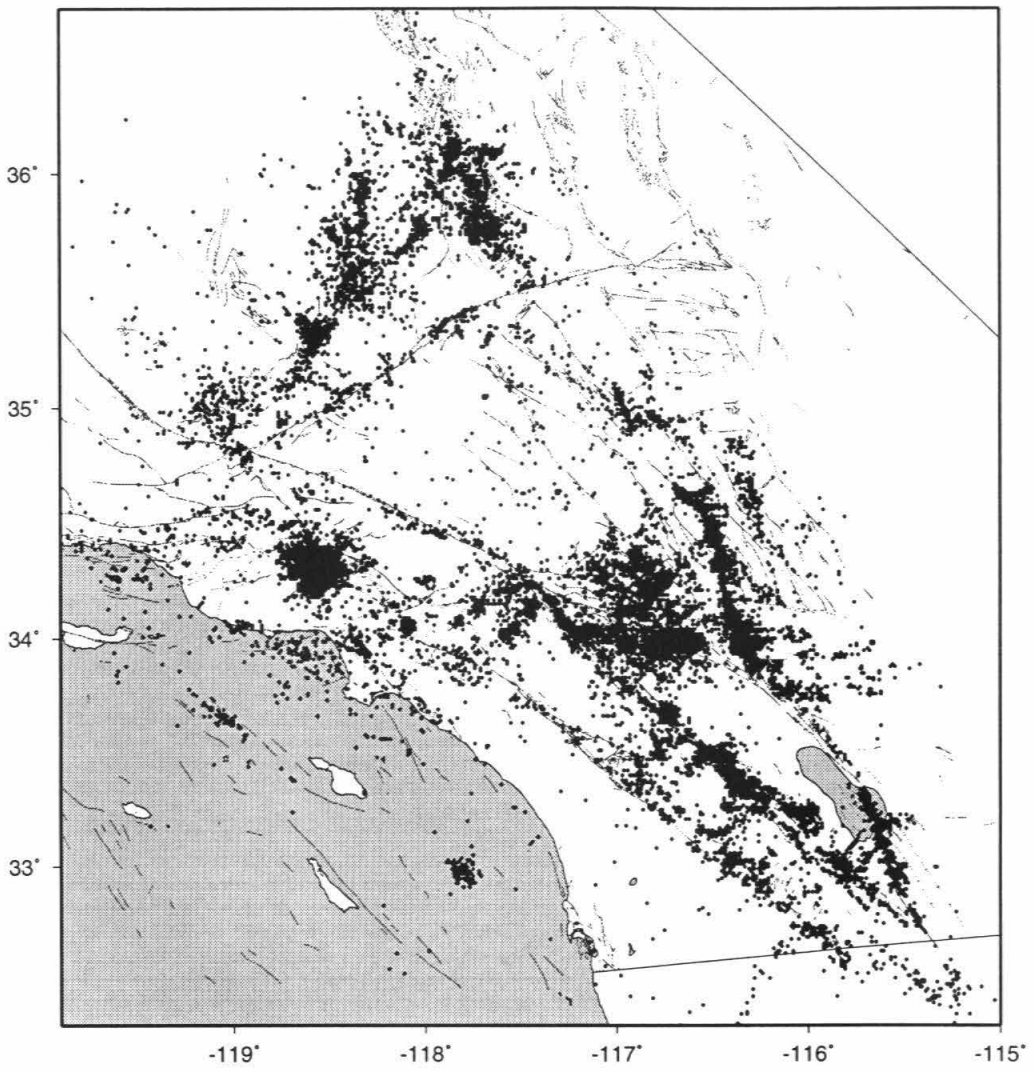

Figure 1.2: Southern California earthquakes used to infer stress orientation. The data set includes ~50,000 events recorded by the Southern California Seismic Network (SCSN) from 1981 to 1999, and during the 1975 Galway Lake and 1979 Homestead Valley sequences. The events were relocated using a three-dimensional seismic velocity model [*Hauksson*, 2000]. Focal mechanisms were determined from the SCSN first-motion data and the recomputed takeoff angles, using the FPFIT software package [*Reasenberg and Oppenheimer*, 1985].

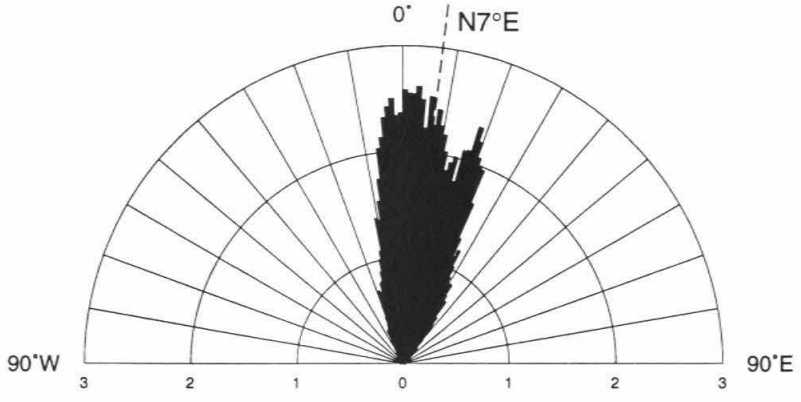

Figure 1.3: Rose diagram of the trend of the σ_H axis for each grid point at which a stress inversion was performed. The length of each sector indicates the percent of points for which the inversion result falls into a 1^o-wide bin. The dashed line indicates the mean orientation.

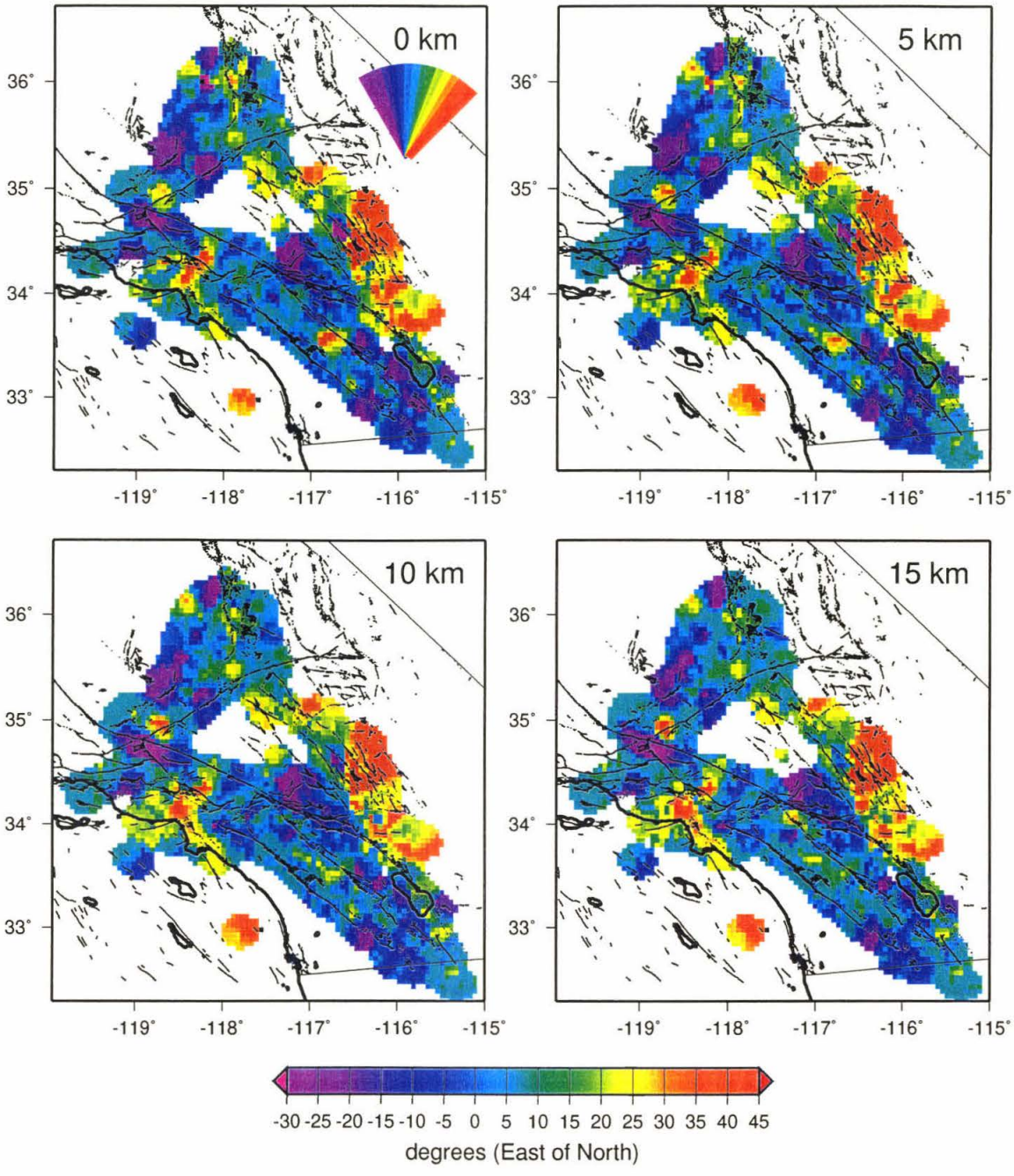

Figure 1.4: Orientation of the maximum horizontal compressive stress, σ_H, at 0, 5, 10 and 15 km depth, measured in degrees clockwise from North. A data set of ~50,000 earthquake focal mechanisms were used to determine stress orientation. An inversion is performed at each point on a 5 km spaced grid using all earthquakes within 5 km of the point or the 50 events closest to the point, whichever data set is largest. Only results with spatial uncertainty $\leq$20 km (1σ) and stress orientation uncertainty $\leq 20^o$ (1σ) are shown. If the orientation of σ_H is indistinguishable from N7E at the 95% confidence level of the inversion, it is shown as N7E.

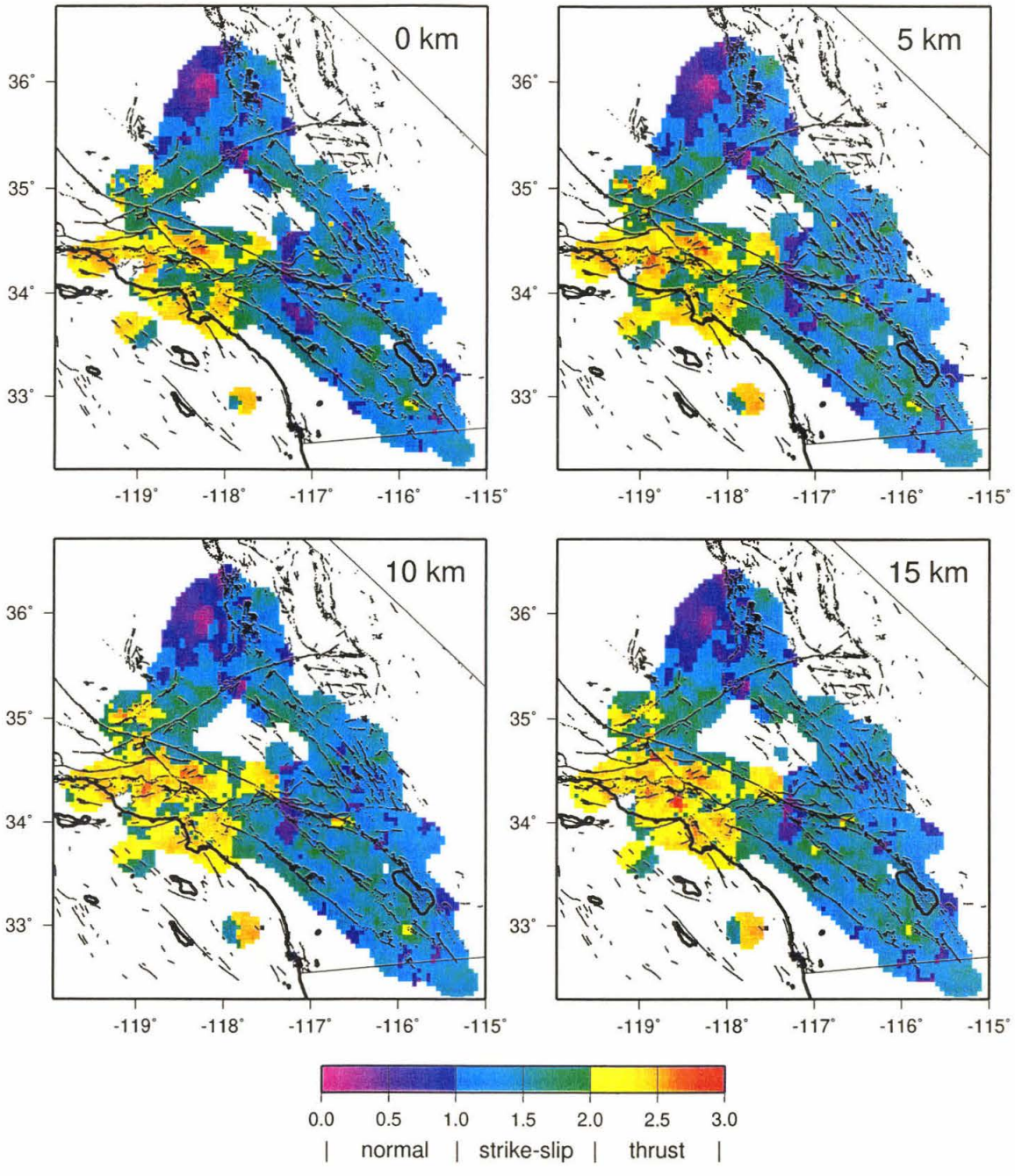

Figure 1.5: Relative magnitude of the three principal stress axes, for the same inversions as shown in Figure 1.4. The parameter A_ϕ is as defined by *Simpson* [1997]. If the maximum principal stress, σ_1, is vertical, corresponding to a normal faulting regime, A_ϕ ranges from 0 to 1. $A_\phi \approx 0$ indicates pure dilatation, $\sigma_2 \approx \sigma_3$; and $A_\phi \approx 1$ indicates a mix of normal and strike-slip faulting, $\sigma_2 \approx \sigma_1$. Similarly, if the minimum principal stress, σ_3, is vertical, corresponding to a thrust faulting regime, A_ϕ ranges from 2 to 3. $A_\phi \approx 3$ indicates pure compression, $\sigma_2 \approx \sigma_1$; and $A_\phi \approx 2$ indicates a mix of thrust and strike-slip faulting, $\sigma_2 \approx \sigma_3$. If σ_2 is vertical, a strike-slip regime, A_ϕ ranges from 1 to 2, depending on whether it is closer to a normal or a thrust faulting regime.

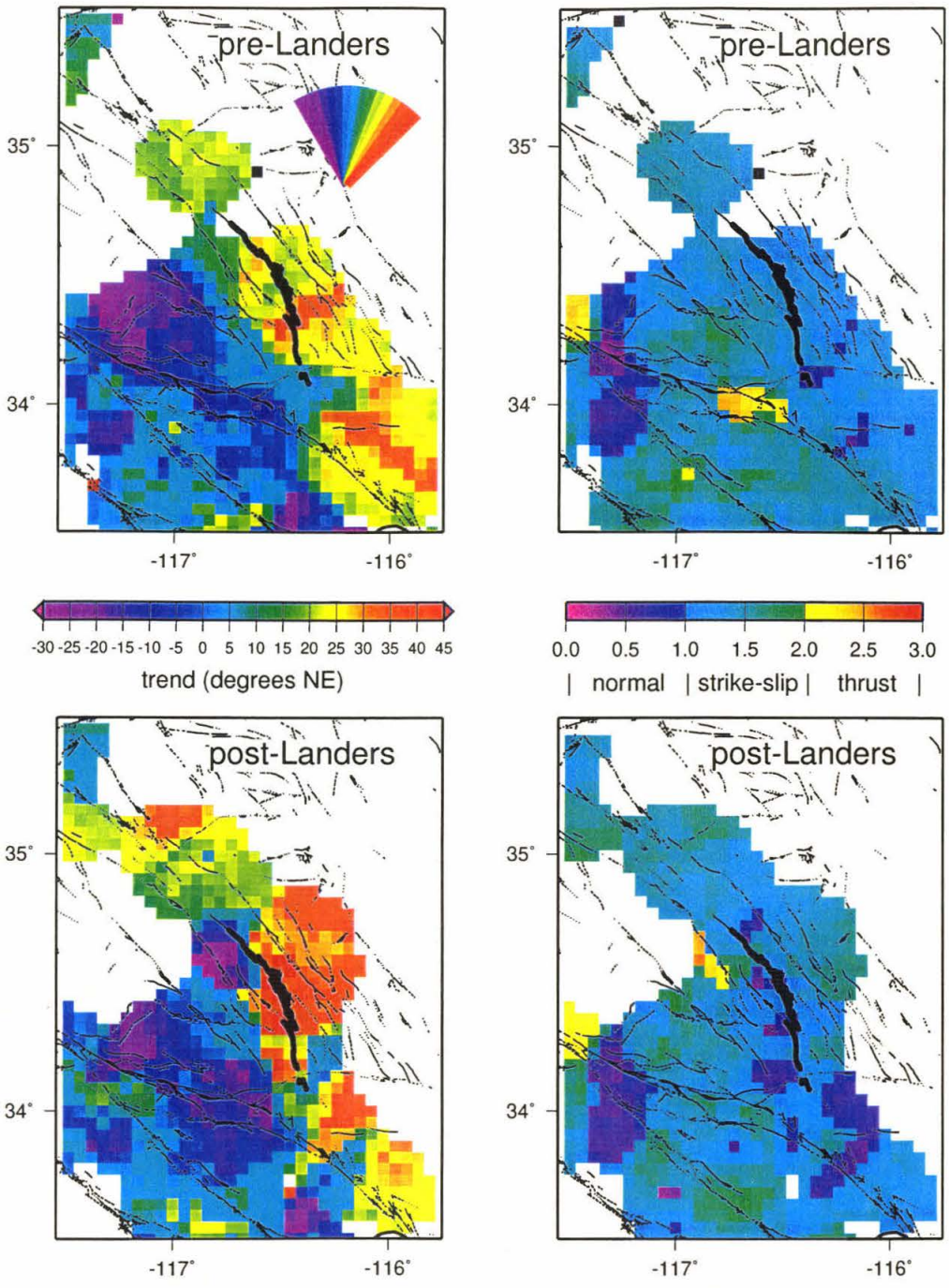

Figure 1.6: The orientation of the maximum horizontal compressive stress, σ_H, and the parameter A_ϕ in the vicinity of the 1992 M7.3 Landers earthquake, before and after the event. The Landers mainshock surface rupture is shown by the dark lines [*Sieh et al.*, 1993]. Stress orientations are computed using the same methodology as for Figure 1.4. Only grid points at 10 km depth are shown, but similar results are obtained at all depths. For the pre-Landers inversion, only events prior to the 4/24/92 M6.2 Joshua Tree foreshock are used. For the post-Landers inversion, only events occurring after the 6/28/92 mainshock are used.

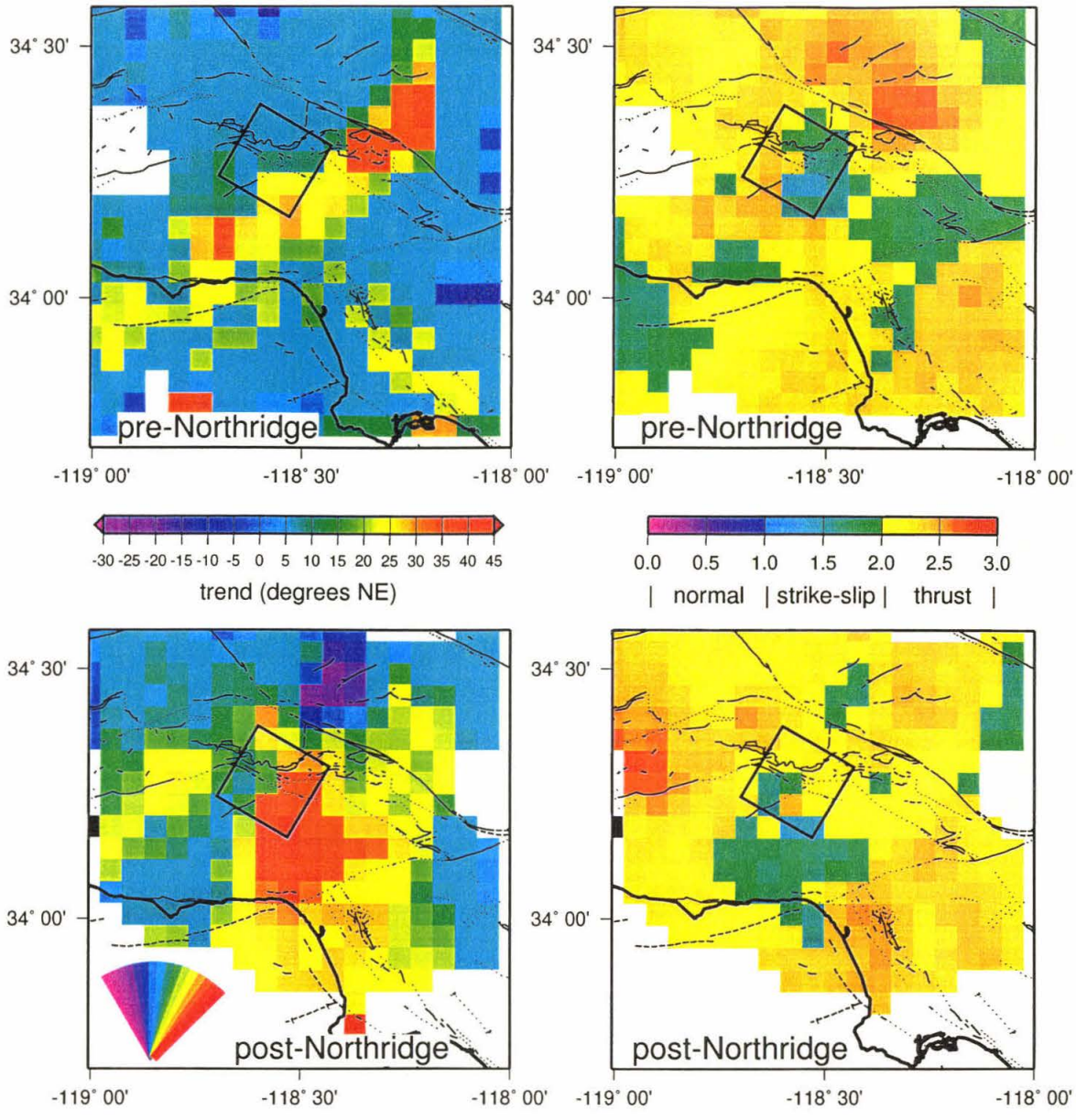

Figure 1.7: The orientation of the maximum horizontal compressive stress, σ_H, and the parameter A_ϕ in the vicinity of the 1994 M6.7 Northridge earthquake, before and after the event. The rectangle is the surface projection of the slip plane of the rupture model of *Wald et al.* [1996]. Stress orientations are computed using the same methodology as for Figure 1.4. Grid points at 10 km depth are shown. Only events occurring prior to the mainshock are used in the pre-Northridge inversion, and only events occurring after the mainshock are used in the post-Northridge inversion.

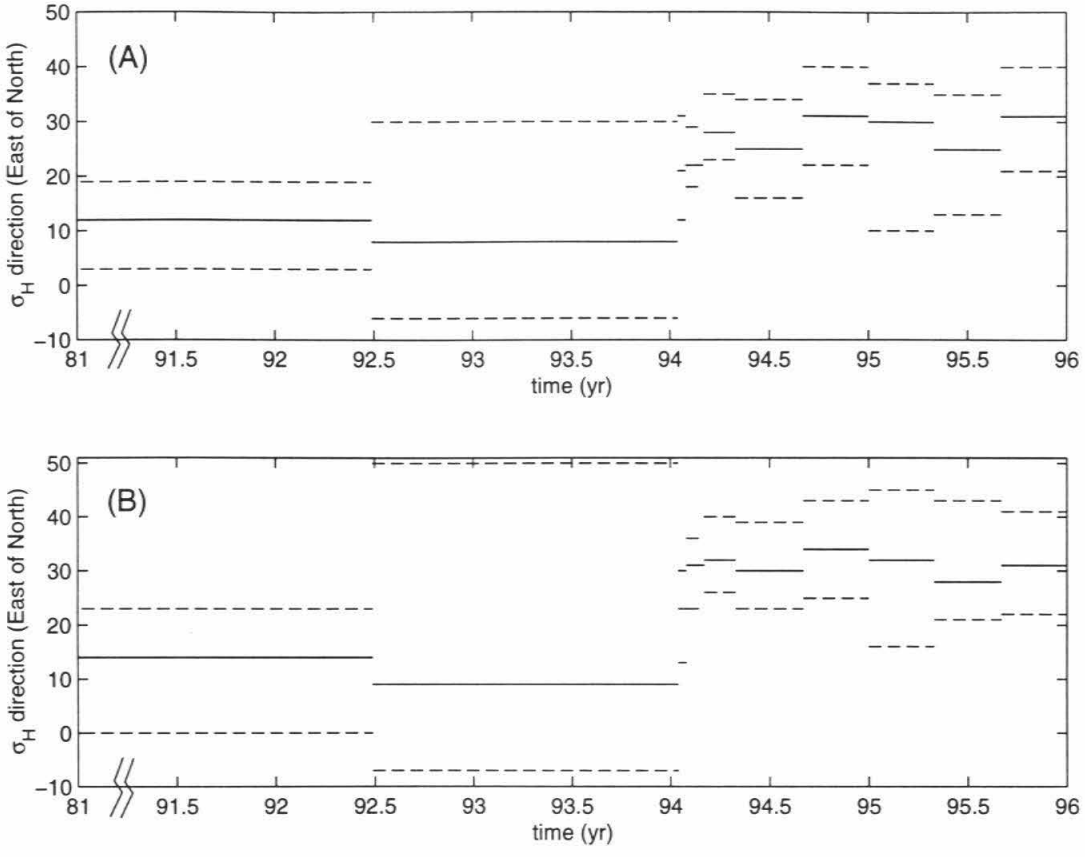

Figure 1.8: The orientation of the maximum horizontal compressive stress, σ_H, through time in the region of the 1994 Northridge earthquake. The earthquakes used in the stress inversion are the same as those used by *Zhao et al.* [1997], and the temporal binning is also the same. Solid lines: orientation of σ_H for the best-fitting stress tensor. Dashed lines: 95% confidence range. (A) First motion focal mechanisms determined using the three-dimensional velocity model of *Hauksson* [2000]. (B) First motion focal mechanisms determined using the three-dimensional velocity model of *Zhao and Kanamori* [1995].

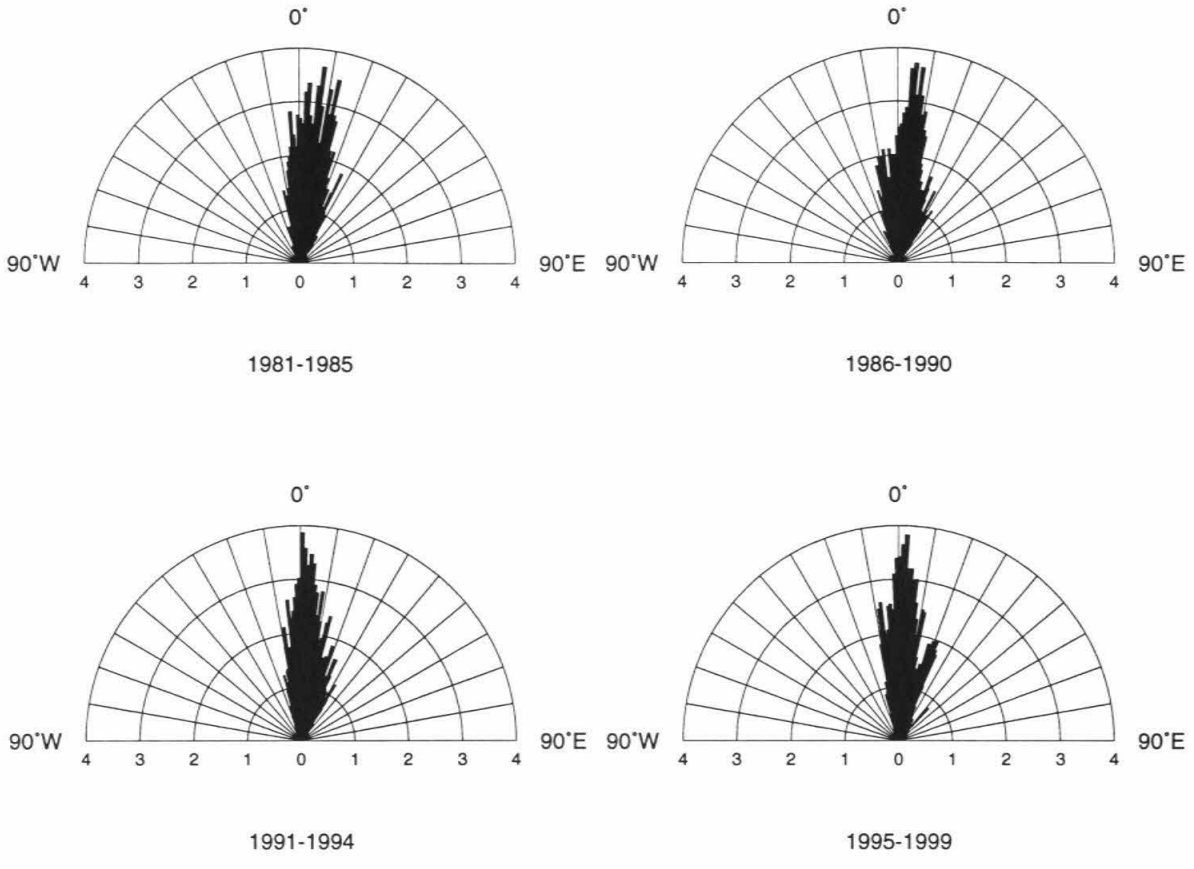

Figure 1.9: Rose diagram of σ_H axis orientation during four time intervals. The length of each sector indicates the percent of points at which the inversion result falls within a 1^o-wide bin.

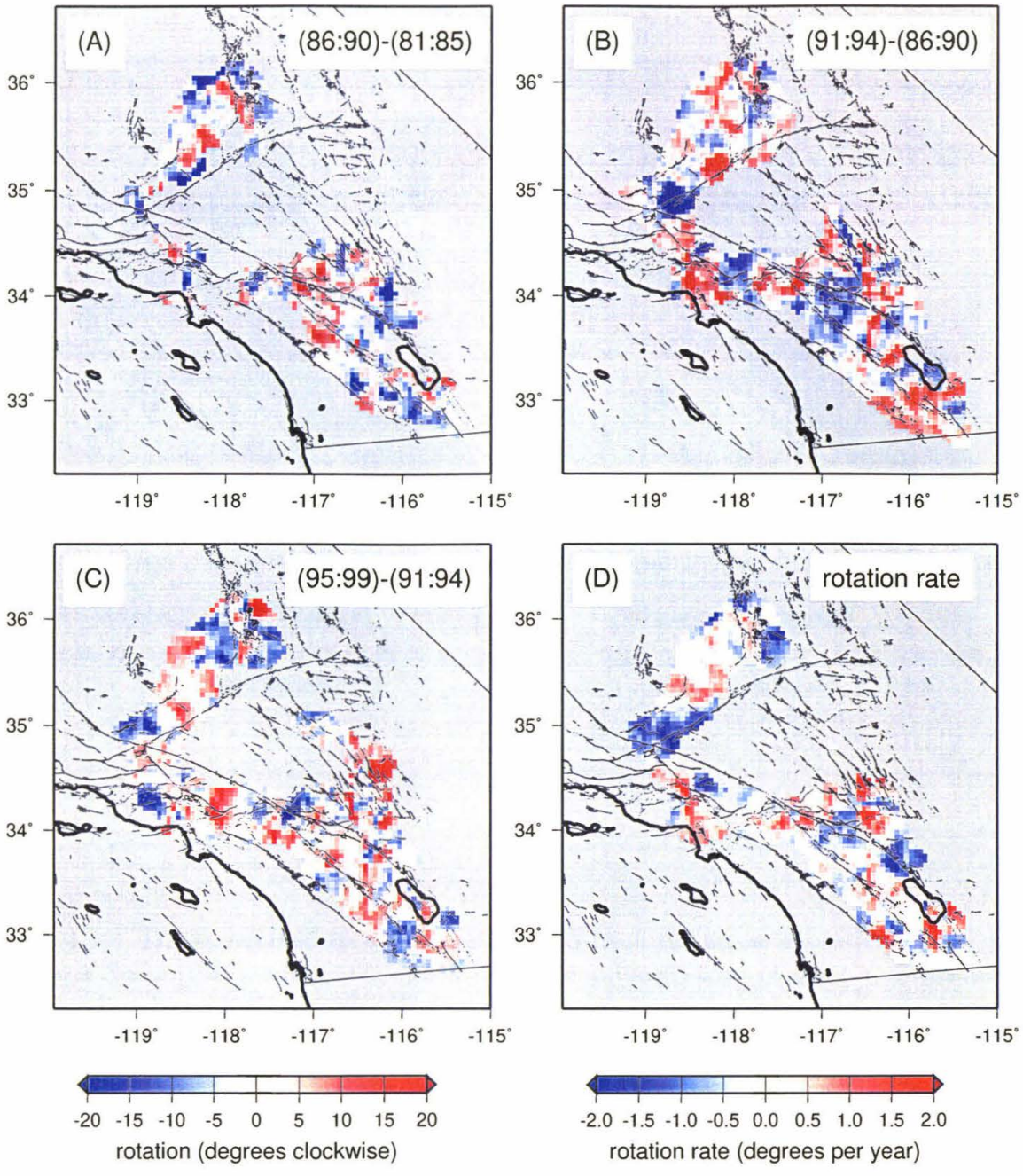

Figure 1.10: The change in stress orientation through time. **(A)** The difference between the σ_H orientation found using events which occurred during 1986-1990 and the orientation found using events which occurred during 1981-1985. **(B)** The difference between 1991-1994 and 1986-1990. **(C)** The difference between 1995-1999 and 1991-1994. **(D)** The rotation per year over the duration of the study. The rotation rate was found by fitting a least-squares linear trend to the results of the 4 time periods.

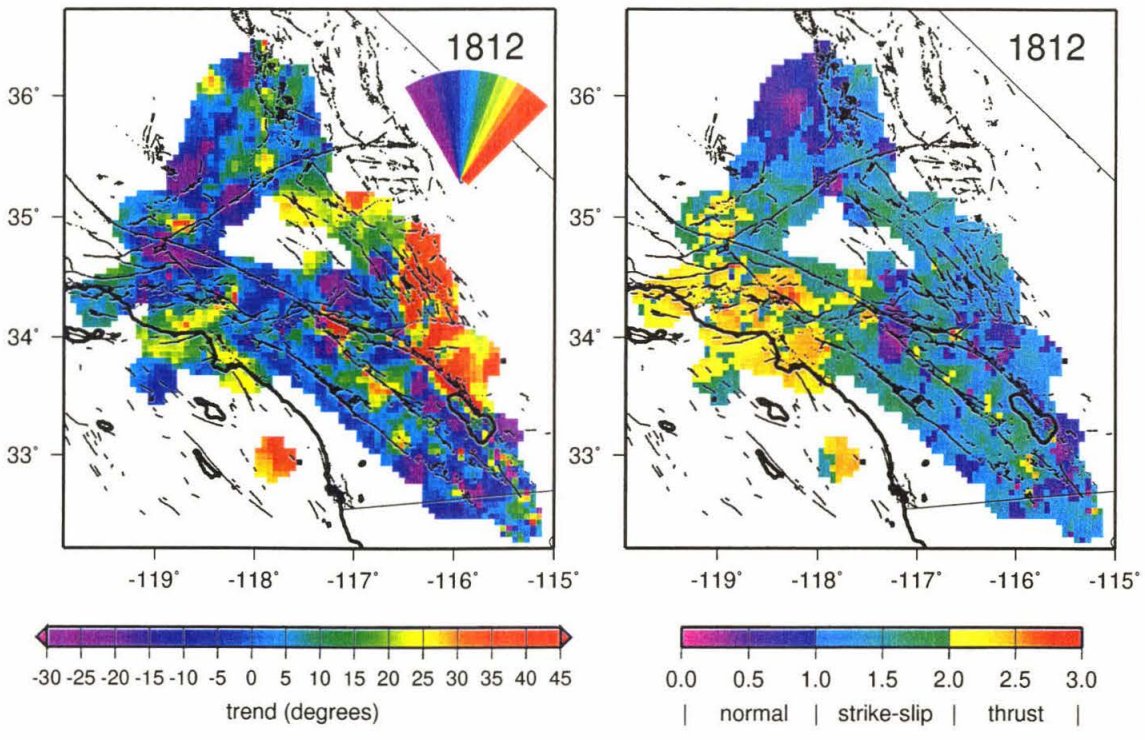

Figure 1.11: The stress field in 1812, as predicted from the stress evolution model of *Deng and Sykes* [1997], which includes earthquake induced stress changes and tectonic stress loading from 1812 to 1992. The prediction was found by subtracting the stress change modeled by *Deng and Sykes* [1997] from the observed stress state in 1992 after the Landers earthquake (*i.e.*, a stress inversion was performed using only ECSZ events occurring after the Landers earthquake and L.A. area events occurring before the 1994 Northridge earthquake), assuming a deviatoric stress of 50 bar. The low stress magnitude was chosen in order to make the stress changes due to the model more apparent. The model is for 8 km depth. The trend of σ_H and the parameter A_ϕ are displayed as in Figure 1.4 and Figure 1.5.

Chapter 2 Stress Magnitude at Seismogenic Depths

2.1 Introduction

The magnitude of the stress in the Earth's crust is more difficult to constrain than its orientation. It is currently unresolved whether deviatoric stress magnitude is high, comparable to the frictional strength of rock predicted by laboratory experiments; or low, perhaps on the order of earthquake stress drop. If the crust has the strength predicted from laboratory experiments [*Byerlee*, 1978], the deviatoric stress at ~10 km depth should be ~1 kbar. Earthquake static stress drops, on the other hand, are ~10-100 bar [*Kanamori and Anderson*, 1975]. Stress magnitude can be measured in boreholes, but they typically sample only the shallow crust. The deepest borehole stress measurements in southern California, near Cajon Pass, extend down to ~3.5 km depth [*Zoback and Healy*, 1992]. Stress magnitude at greater depths in southern California must therefore be inferred seismologically.

The magnitude of the deviatoric part of the crustal stress tensor can be estimated from the stress orientation rotations caused by major earthquakes. The amount of rotation a stress change can cause is controlled by the ratio of the magnitude of the stress change, $\Delta\tau$, to the magnitude of the background deviatoric stress, τ, as well as by the relative orientation of the two stress tensors. *Yin and Rogers* [1995] found a relationship between $\Delta\tau/\tau$ and the rotation of the principal stress axes for the two-dimensional case in which the stress tensor rotates about the σ_2 axis. This solution can be applied only to stress rotations very near the center of the mainshock rupture because the earthquake stress drop is used as $\Delta\tau$. *Yin and Rogers* [1995] use the stress rotations found for the Joshua Tree and Landers earthquakes [*Hauksson*, 1994] to estimate $\Delta\tau/\tau$. They find $\Delta\tau/\tau \approx 0.4$ and 0.8 for Joshua Tree and Landers,

respectively, indicating that the background deviatoric stress is low, on the order of earthquake stress drop.

In this Chapter, I also use the stress rotations caused by major earthquakes in southern California to constrain the deviatoric stress magnitude. First, I present a solution for the two dimensional problem which does not depend on two questionable assumptions made by *Yin and Rogers* [1995]. Second, I use an inversion technique to solve for stress magnitude in the three-dimensional case, in which the stress tensor may rotate about any axis. The two-dimensional solution can be used to make a point estimate of deviatoric stress magnitude at the location of an earthquake from only the near-field stress orientations before and after the event and the earthquake stress drop. The three-dimensional inversion method requires more stress information and an earthquake slip model, but is more powerful because it allows deviatoric stress magnitude to be measured away from the earthquake rupture.

2.2 Two-Dimensional Solution

2.2.1 Method

A general two-dimensional solution can be found for the relationship between the near-field rotation of the stress tensor and the ratio of the earthquake stress drop, $\Delta\tau$, to the background deviatoric stress magnitude, τ. I follow a procedure similar to that used by *Sonder* [1990] for the stress rotations associated with linear density anomalies. This is preferable to the solution obtained by *Yin and Rogers* [1995] because they make two assumptions which may not generally hold. The first assumption is that the mainshock fails in accordance with the Coulomb failure criterion, which may not be the case, for instance for a weak fault. The second assumption is that the magnitude of the deviatoric stress does not change, which is clearly not true since the mainshock relieves a portion of the shear stress. The second assumption is approximately correct if the ratio $\Delta\tau/\tau$ is small, but if the stress drop is on the order of the deviatoric stress, as it appears to be in the Landers example, the assumption breaks down.

The post-mainshock stress tensor equals the pre-mainshock stress tensor plus the stress change tensor due to the mainshock (Figure 2.1). The pre-mainshock deviatoric stress tensor is:

$$\sigma_{pre} = \begin{pmatrix} \tau & 0 \\ 0 & -\tau \end{pmatrix} \tag{2.1}$$

where $\tau = (\sigma_3 - \sigma_1)/2$ is the deviatoric stress magnitude (tension is positive). The earthquake occurs on a fault plane oriented at an angle of θ to the σ_1 axis orientation (sign convention shown in Figure 2.1). The stress change tensor due to the earthquake is:

$$\Delta\sigma = \begin{pmatrix} -2\Delta\tau\cos\theta\sin\theta & \Delta\tau(\cos^2\theta - \sin^2\theta) \\ \Delta\tau(\cos^2\theta - \sin^2\theta) & 2\Delta\tau\cos\theta\sin\theta \end{pmatrix} \tag{2.2}$$

where $\Delta\tau$ is the earthquake stress drop. The post-mainshock stress tensor is therefore:

$$\sigma_{post} = \sigma_{pre} + \Delta\sigma = \begin{pmatrix} \tau - 2\Delta\tau\cos\theta\sin\theta & \Delta\tau(\cos^2\theta - \sin^2\theta) \\ \Delta\tau(\cos^2\theta - \sin^2\theta) & -\tau + 2\Delta\tau\cos\theta\sin\theta \end{pmatrix}. \tag{2.3}$$

Solving for the eigenvalues and eigenvectors, one finds that the post-earthquake stress tensor is rotated from the pre-earthquake stress tensor by an angle of $\theta^\star$, where

$$\theta^\star = atan\left(\frac{1 - \frac{\Delta\tau}{\tau}\sin 2\theta - \left[\left(\frac{\Delta\tau}{\tau}\right)^2 + 1 - 2\frac{\Delta\tau}{\tau}\sin 2\theta\right]^{\frac{1}{2}}}{\frac{\Delta\tau}{\tau}\cos 2\theta} \right). \tag{2.4}$$

Note that the rotation depends on only two parameters: θ, the orientation of the fault relative to the pre-earthquake stress field; and $\Delta\tau/\tau$, the ratio of the earthquake stress drop to the background deviatoric stress level. $\theta^\star$ versus θ is shown for various values of $\Delta\tau/\tau$ in Figure 2.2. This figure is very similar to that for a linear density anomaly [*Sonder*, 1990], the major difference being a 45^o shift of the x-axis because of the difference between a shear source and a tensional or compressional source.

A potential problem with using Equation 2.4 to estimate $\Delta\tau/\tau$ is apparent in Figure 2.2. As the orientation of the fault relative to σ_1 goes to $\pm 45^o$, the rotation angle goes to 0, for any $|\Delta\tau/\tau| < 1$. This is because at $\theta = 45^o$, the two stress tensors

are collinear, so adding them will change the magnitude of the two axes, but will not cause a rotation. Where the results for all $|\Delta\tau/\tau|$ <1 start to converge, it becomes more difficult to infer $\Delta\tau/\tau$ from the stress rotations. An angle of $\sim 45^o$ to σ_1 is also a favorable orientation for fault failure, so many earthquakes may fall into regions where very high-precision stress rotation measurements are necessary to determine $\Delta\tau/\tau$ even to within an order of magnitude.

2.2.2 Results

To estimate $\Delta\tau/\tau$ using the solution given above, θ and $\theta^\star$ must be observed. I find stress orientations before and after the Landers mainshock on four segments of the rupture (Figure 2.3, Table 2.1), similar to the segments used by *Hauksson* [1994]. The pre- and post-Landers stress tensors along each fault segment are different at the 95% confidence level of the inversion, strongly suggesting that the Landers mainshock caused a rotation of the stress field. The significance of the difference between the pre- and post-Landers stress fields can be seen using a technique for identifying stress changes [*Wyss and Lu*, 1995]. Changes in the misfits of individual focal mechanisms with respect to a given stress tensor, here the bestfit pre-Landers stress, signal changes in the stress field. For earthquakes near Landers, the slope of the cumulative misfit curve, which represents the average misfit, changes from $\sim 25^o$/event to $\sim 44^o$/event at the time of the Landers mainshock (Figure 2.4). The high misfit of the aftershocks indicates that they are poorly fit by the pre-event stress tensor, implying a post-mainshock stress state which is different form the pre-mainshock state.

The stress rotations observed in Figure 2.3 are shown along with the analytic solution in Figure 2.2 and are used to constrain $\Delta\tau/\tau$. The Johnson Valley, Homestead Valley and Emerson segments provide both lower and upper bounds. For the Johnson Valley segment, $0.25 \leq \Delta\tau/\tau < 1$; for the Homestead Valley segment, $0.4 \leq \Delta\tau/\tau < 1$; and for the Emerson segment, $0.35 \leq \Delta\tau/\tau \leq 0.85$. The Camp Rock segment experienced a $\sim 21 \pm 14^o$ rotation, qualitatively suggesting high $|\Delta\tau/\tau|$, but the rotation appears to be in the wrong direction, *i.e.*, the direction which would be expected for

left-lateral slip. There is not very much slip on this segment [*Wald and Heaton*, 1994], so the stress rotation here may be dominated by the stress changes due to the other segments. Additionally, there is little pre-Landers seismicity along this segment, so the pre-event stress orientation may not be well constrained.

The deviatoric stress magnitude, τ, can be inferred from $\Delta\tau/\tau$ if the earthquake stress drop, $\Delta\tau$, is known. The average stress drop for the Johnson Valley, Homestead Valley and Emerson segments, estimated from the mapped surface slip (Table 2.1), is ~80 bar. Assuming a value of $\Delta\tau/\tau \approx 0.65$, which fits the rotations of the three segments very well, $\tau \approx 120$ bar. This is nearly an order of magnitude less than would be consistent with the crustal strength predicted by laboratory experiments. Conservative error estimates (Table 2.1) constrain τ to be less than ~250-320 bar.

The estimated magnitude of τ could be incorrect if there was afterslip on the fault, *i.e.*, if $\Delta\tau$ is an underestimate of the true total stress drop. However, if τ is to be on the order of 1 kbar, the afterslip would have to be very large, as large as the coseismic slip. It seems highly unlikely that such large afterslip could have gone undetected for a well-studied event such as Landers.

2.3 Three-Dimensional Inversion

2.3.1 Method

The deviatoric stress magnitude can also be estimated using the three-dimensional stress tensor. In order to do so, the normalized deviatoric stress tensor at a given location prior to the mainshock, σ_{pre}, and after the mainshock, σ_{post}, must be found, and the static stress change tensor due to the mainshock, $\Delta\sigma$, must be computed from the mainshock slip distribution. The predicted post-earthquake stress tensor, $\sigma_{post}^{predict}$, for a given background deviatoric stress magnitude, τ, is the pre-mainshock stress tensor, scaled by the deviatoric stress, plus the stress change tensor, or

$$\sigma_{post}^{predict} = \tau\sigma_{pre} + \Delta\sigma. \tag{2.5}$$

One can search for the value of τ that minimizes the misfit between the deviatoric part of $\sigma_{post}^{predict}$ and σ_{post}. Since τ is a scalar, the minimization procedure is a straightforward search over possible values. The misfit between the deviatoric part of $\sigma_{post}^{predict}$ and σ_{post} is defined using the normalized tensor dot product.

I use this methodology to find τ from the stress rotations due to the Landers sequence, using the focal mechanism data set and stress inversion method described in Chapter 1. I divided the Landers region into 10 km x 10 km boxes in four different depth ranges (Figure 2.5). The post-mainshock stress for each box, σ_{post}, was found by inverting only the aftershocks inside that box. Since the pre-Landers seismicity is not as dense as the aftershocks, the pre-event stress tensor, σ_{pre}, was found using events from an area 4 times as large as the box. The stress change for each box, $\Delta\sigma$, was computed at the average location of aftershocks in that box, assuming an elastic half-space, following *Okada* [1992]. The Landers mainshock was modeled using the slip distribution of *Wald and Heaton* [1994], and the Joshua Tree preshock and Big Bear aftershock were modeled as dislocations with 0.35 m slip on a 12-15 km long fault plane.

2.3.2 Results

Figure 2.6 shows the average misfit for boxes in each depth range versus the deviatoric stress level, τ. The average misfit for 0-5 km depth is lowest for $\tau \approx$50 bar; 5-10 km depth, $\tau \approx$100 bar; 10-15 km depth, $\tau \approx$250 bar; and 15-20 km depth, $\tau \approx$10 bar. The minimum average misfits are 20-45% less than the average misfits for τ =1 kbar, indicating that while low stress is clearly preferred, high stress cannot be completely ruled out. The deviatoric stress magnitude appears to increase slowly with depth down to $\sim$15 km. For 15-20 km depth, the results may be unreliable due to the small number of data points. For synthetic tests assuming $\tau \approx$100 bar, a minimum misfit at $\tau \approx$10 bar is obtained in numerous trials.

The three-dimensional inversion technique introduced here appears to be a viable method for obtaining stress magnitude estimates. However, some problems, including

low misfit reduction, indicate that improved data quality will be necessary in order to constrain stress magnitude with a high level of certainty. Also problematic are the scattered boxes for which the stress tensor appears to rotate in the opposite direction from what is predicted.

2.4 Discussion

Results from both the two-dimensional analytic solution and the three-dimensional inversion indicate that the deviatoric stress in the crust in the vicinity of the Landers earthquake is low, on the order of 100 bar. The low deviatoric stress level clearly applies to the ECSZ. In the three-dimensional inversion, low values of τ are also found in the San Bernardino Mountains and along parts of the San Andreas Fault, implying that these areas are at low stress as well. This suggests that the entire southern California plate boundary region may be at low stress.

If deviatoric stress in the southern California plate boundary region is low, active faults in southern California must be weak in order to operate at low levels of shear stress. At the very least, the active faults of the ECSZ must be weak. Three classes of fault-weakening models have been proposed: high-pressure fluids [*Hubbert and Rubey*, 1959; *Rice*, 1992]; inherently weak fault zone materials, although most candidate minerals have been eliminated by laboratory testing [*Moore et al.*, 1996; *Morrow et al.*, 1992]; and dynamic weakening [*Heaton*, 1990; *Melosh*, 1996; *Andrews and Ben-Zion*, 1997].

The stress magnitudes and fault strengths discussed in this chapter are clearly average values over length scales on the order of 10s of km. Smaller-scale variations in fault strength and deviatoric stress are acceptable and likely. Locally high deviatoric stress magnitudes presumably exist at crack tips and fault irregularities. Dynamic fault weakening mechanisms require small-scale heterogeneity, as locally high shear stress or locally low static strength is necessary to initiate rupture.

The observed stress magnitudes are best explained by a model in which major active faults are weak, while the intact crust is strong. In an intraplate setting, the

crust as a whole is strong because it contains no major active faults, so the deviatoric stress is high, as is observed in deep boreholes [*Brudy et al.*, 1997]. In a simple plate boundary region, containing only one major active fault, the deviatoric stress magnitude may also be high, but the stress tensor must be oriented such that little shear stress is resolved onto the fault. In a complex plate boundary region, like southern California, however, there are weak faults in many orientations. The crust as a whole cannot support high shear stresses because of the numerous planes of weakness, and the deviatoric stress is low.

The deviatoric stress magnitudes implied by earthquake stress rotations are on the same order of magnitude as shallow borehole stress measurements in southern California. The maximum observed deviatoric stress in the Cajon pass borehole, near the western edge of the Landers study area, is $\sim$300$\pm$100 bar [*Zoback and Healy*, 1992]. The two observations are inconsistent only if it is assumed that the borehole stress measurements can be extrapolated to greater depths, which would imply $\sim$1 kbar deviatoric stress at 10 km depth. The observations presented here suggest that deviatoric stress does not increase with depth as rapidly as would be predicted for a strong crust.

A common argument against a low strength crust is that it could not support steep topography such as the Transverse Ranges. However, a shear strength on the order of 100 bar is consistent with the Transverse Range topography, if it is isostatically supported. The potential energy difference between two columns in isostatic equilibrium will result in a local horizontal force on the boundary between them [*Turcotte and Schubert*, 1982]. The force per unit length parallel the boundary, F, can be written:

$$F = \int_0^\infty \rho_1(z) g z dz - \int_0^\infty \rho_2(z) g z dz \tag{2.6}$$

where $\rho_1(z)$ and $\rho_2(z)$ are the density structures of the two columns, g is the gravitational acceleration, and z is height above the depth of compensation. The resulting

horizontal stress, averaged over a 60 km thick lithosphere, is:

$$\sigma_{xx} = \frac{F}{60\text{km}} \tag{2.7}$$

and the corresponding deviatoric stress is $\sigma_{xx}/2$. Topography of $\sim$2 km produces a force of $\sim 2 \cdot 10^{12}$ N/m, or a deviatoric stress of $\sim$150 bar, assuming ρ=2700 kg/m^3 in the crust and 3300 kg/m^3 in the mantle, and that the crust is 30 km thick. Therefore, the average deviatoric stress in the lithosphere due to isostatically supported mountains is of similar magnitude to the inferred strength of faults.

2.5 Conclusions

Stress magnitude at seismogenic depths in southern California has been constrained from the rotations of the stress field due to major earthquakes. The results of both a two-dimensional analytic solution and a three-dimensional inversion imply a low level of deviatoric stress magnitude, on the order of 100 bars. This is an order of magnitude less than would be expected if the crust had the strength predicted by laboratory experiments. The observations can be explained by a model in which faults are weak while the intact crust is strong.

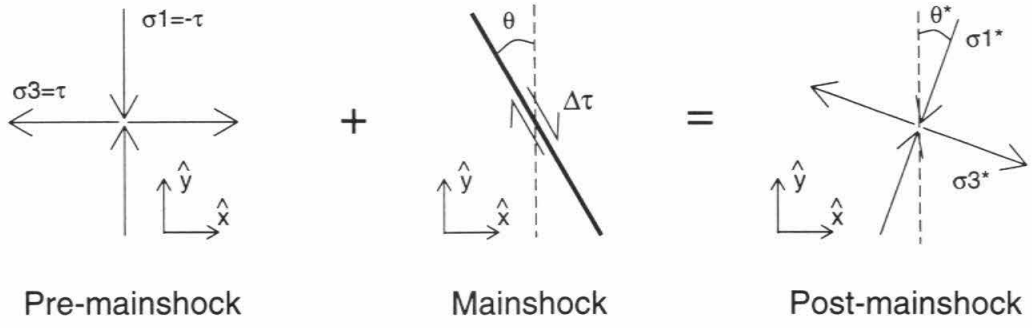

Figure 2.1: The assumed geometry of a stress rotation due to slip on a fault. The post-mainshock stress state is equal to the pre-mainshock stress state plus the stress change due to the earthquake. The problem is assumed to be two-dimensional, so it can be represented entirely in the σ_1-σ_3 plane. θ is the angle from the fault trend to the σ_1 axis, clockwise positive. $\theta^\star$ is the rotation of the stress field, clockwise positive. The mainshock stress drop, $\Delta\tau$, is taken to be positive for the sense of slip shown, and negative for the opposite sense of slip. Note that the σ_1-σ_3 plane may represent a map view, cross section, or oblique view, depending on the orientation of the stress axes.

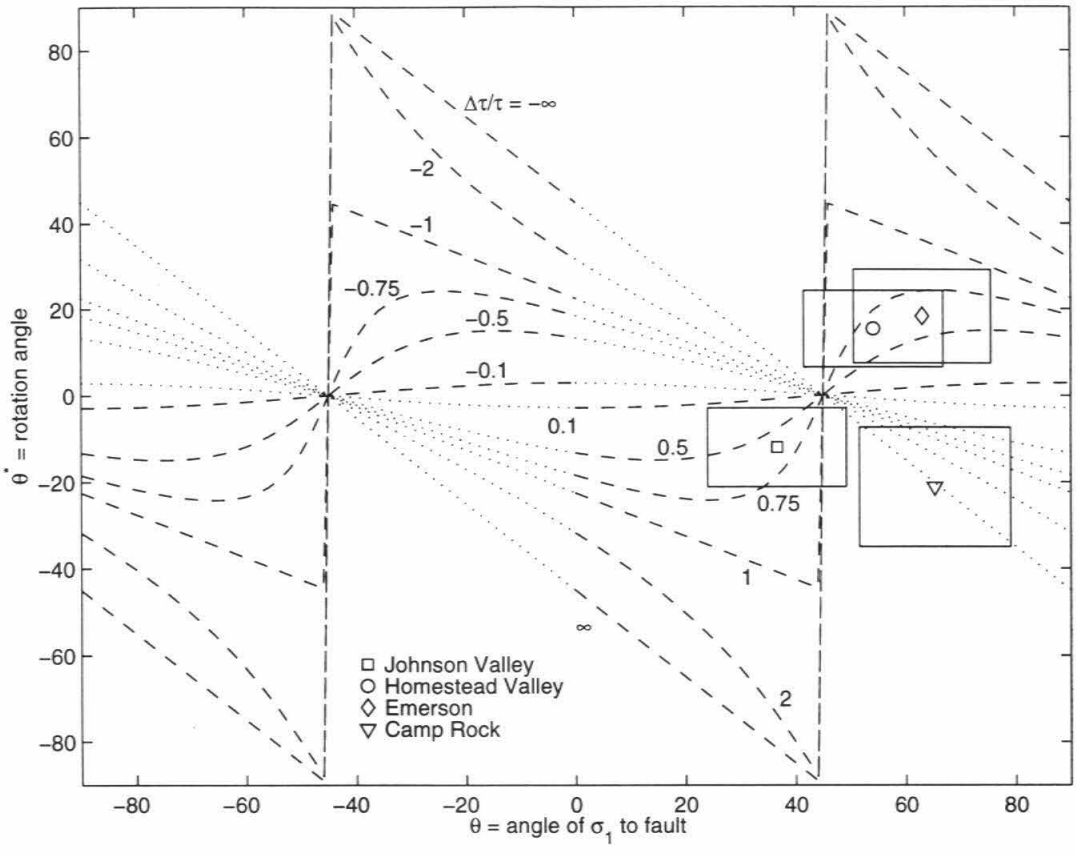

Figure 2.2: The rotation of the stress field due to an earthquake, two-dimensional solution (Equation 2.4). The stress rotation, $\theta^\star$, is shown versus the angle of the fault to the pre-earthquake σ_1 axis, θ, for various values of $\Delta\tau/\tau$, the ratio of the stress drop to the deviatoric stress magnitude. The geometry is shown in Figure 2.1. Dashed lines indicate that the sign of $\Delta\tau/\tau$ is consistent with mainshock slip in the direction of resolved pre-earthquake shear stress; dotted lines, opposite to this direction. The observed θ and $\theta^\star$ for four segments of the 1992 Landers earthquake (Figure 2.3, Table 2.1) are shown as symbols. Large squares are the 2σ confidence ranges of the stress orientations and fault strike.

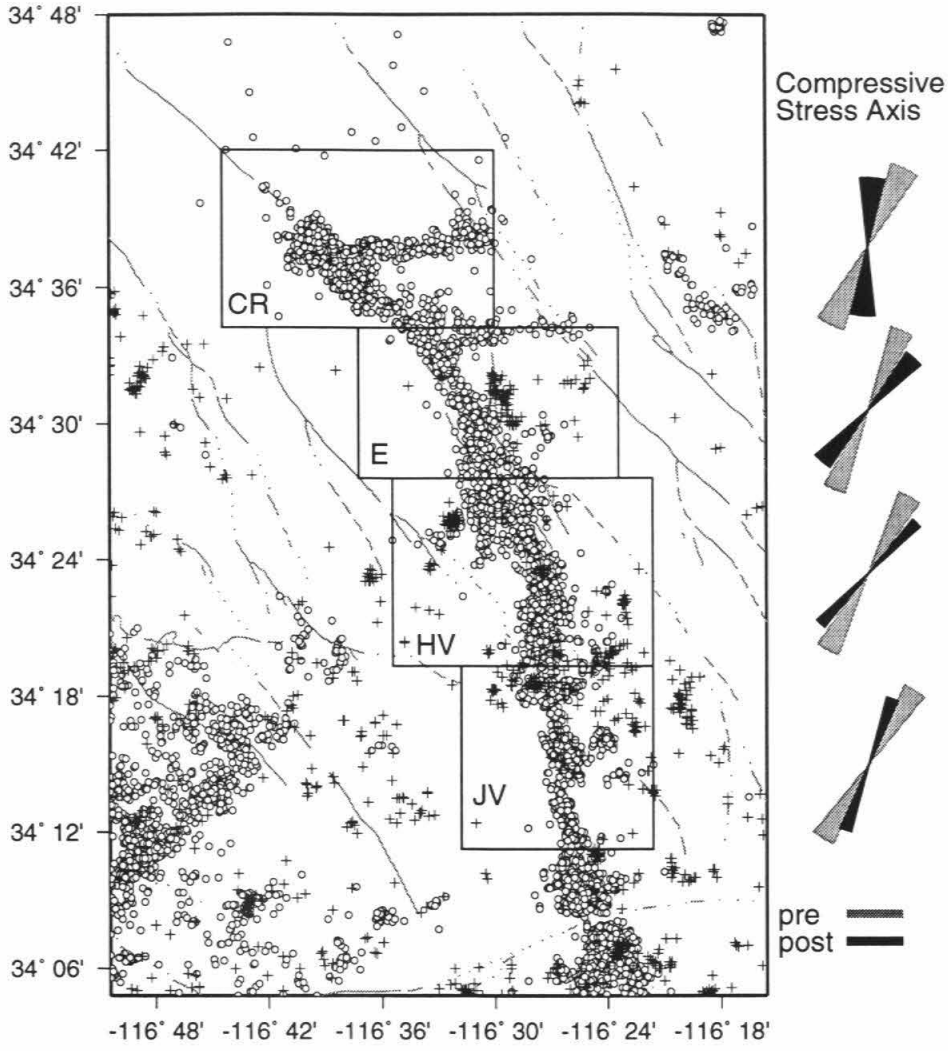

Figure 2.3: Earthquakes and fault segments used in the two-dimensional inversion for stress magnitude near Landers. The events shown as crosses occurred prior to the Landers mainshock, while those shown as circles occurred after. The four fault segments, Johnson Valley (JV), Homestead Valley (HV), Emerson (E), and Camp Rock (CR), are shown along with the spatial extent of the events used in the stress inversion. The pre-mainshock inversion for the Camp Rock segments also includes events up to 0.1^o away from the edge of the box. To the right, the orientation of σ_H before and after the mainshock. The width of the wedge indicates the 95% confidence region.

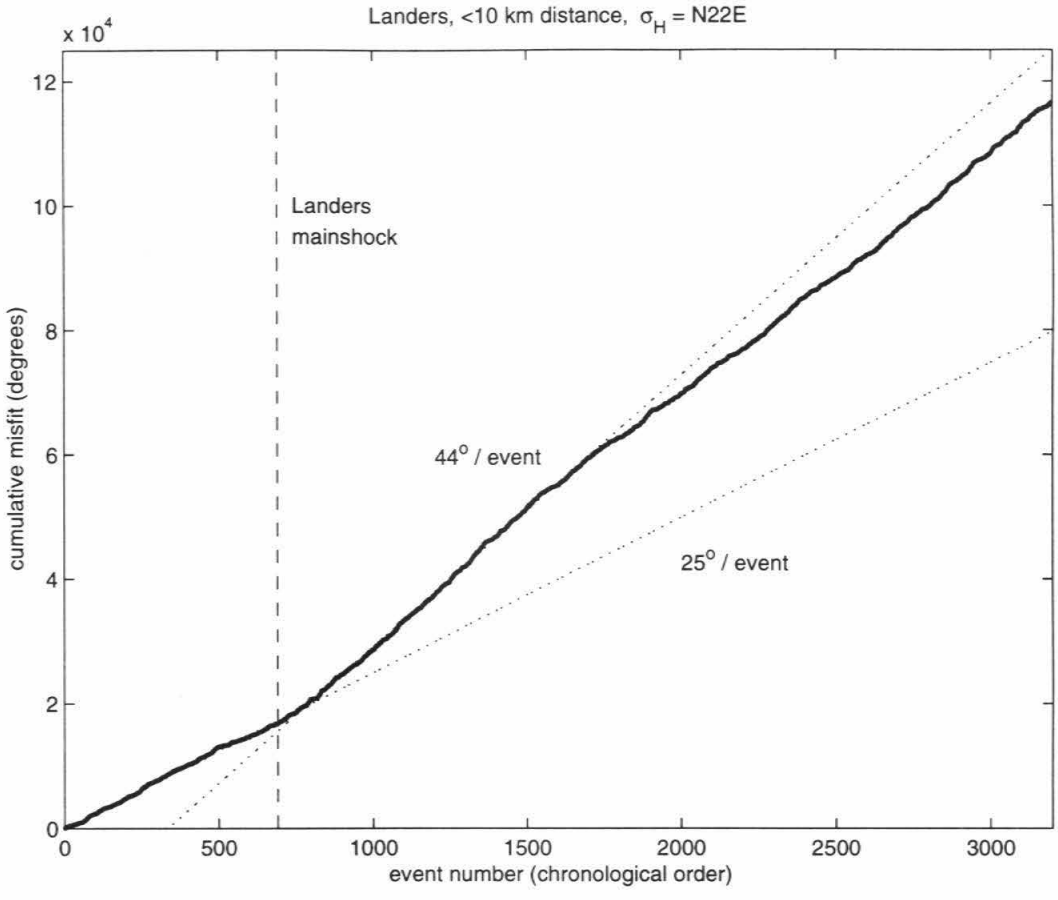

Figure 2.4: Cumulative misfit, relative to a given stress state, for the focal mechanisms of earthquakes occurring within 10 km of the Landers mainshock rupture, ordered chronologically. Aftershocks within 1 km of the rupture were excluded. The stress field is strike-slip with σ_H trending N22E, the preferred pre-Landers orientation of *Hauksson* [1994]. The slope of the curve represents the average misfit per event.

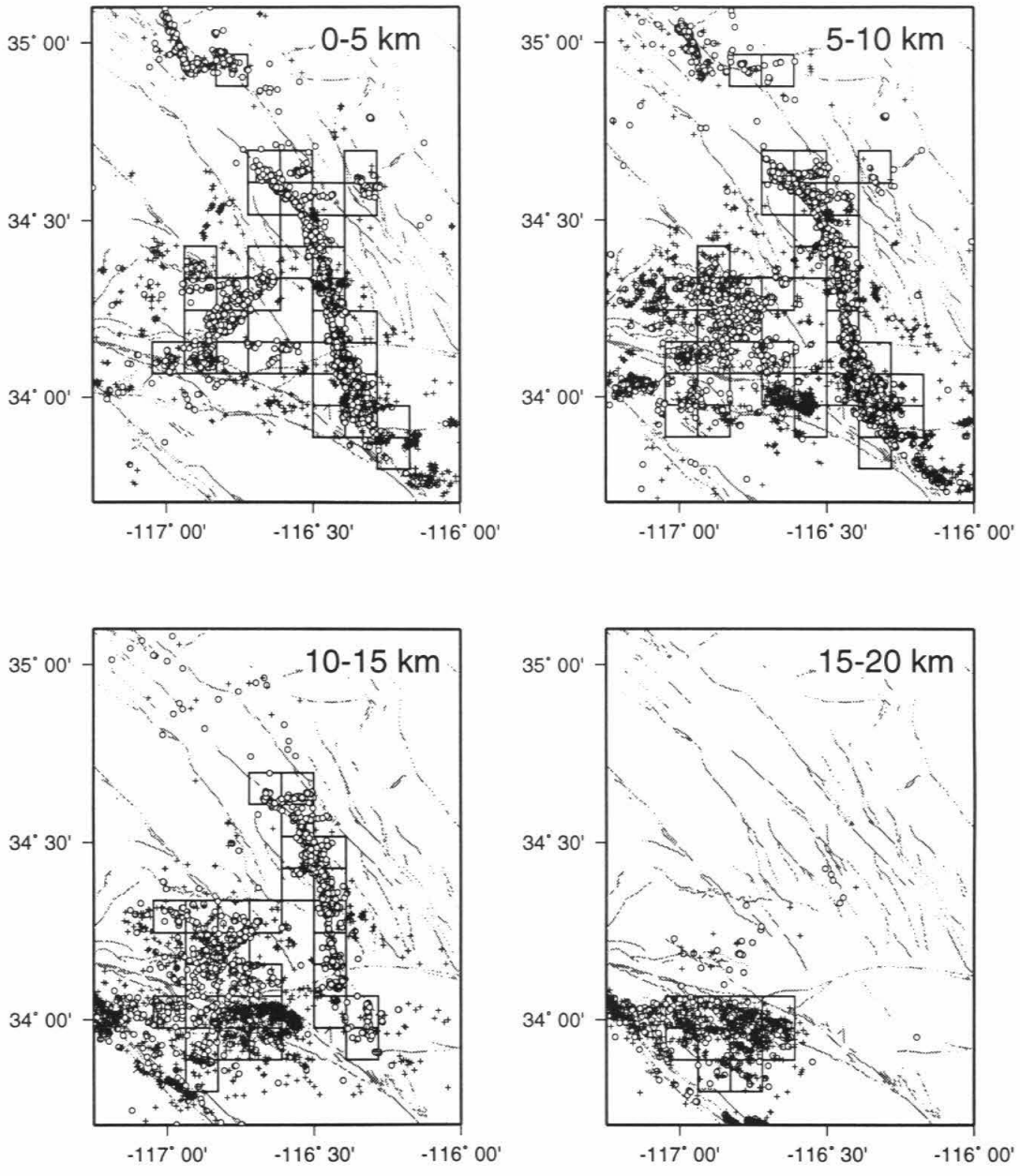

Figure 2.5: Earthquakes and bins used in the three-dimensional inversion for stress magnitude near Landers. The boxes indicate the spatial extent of the bins in each depth range. The events shown as crosses are prior to the Joshua Tree preshock, and the events shown as circles are after the Big Bear aftershock. All bins have a total modeled stress change due to Landers, Big Bear and Joshua Tree of at least 0.1 MPa.

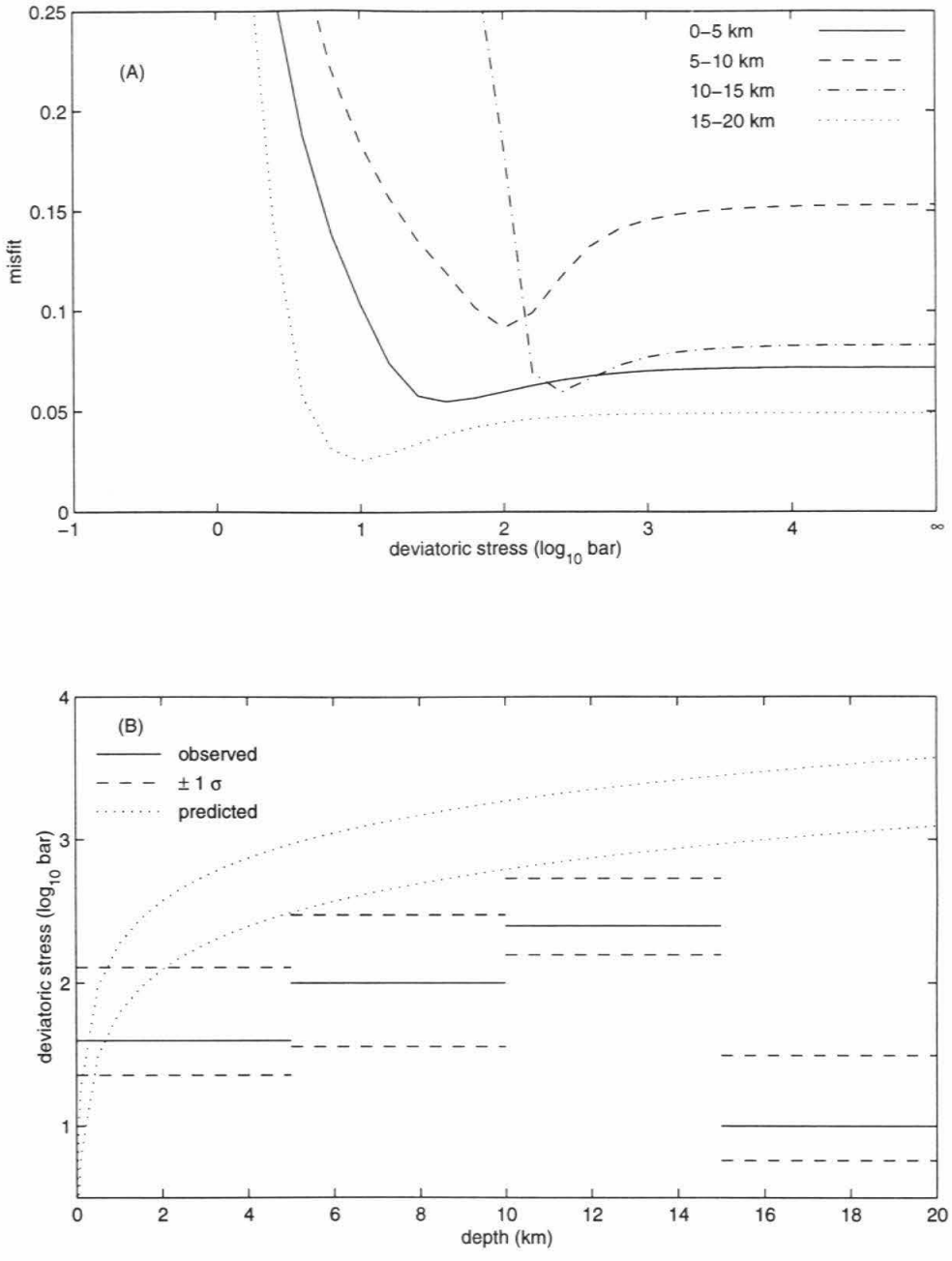

Figure 2.6: Results of a three-dimensional inversion for stress magnitude in the Landers region (Figure 2.5.) **(A)** Misfit versus deviatoric stress level, τ, for the four depth ranges. The misfit is defined as (1-σ_{post}:$\sigma_{post}^{predict}$), where σ_{post}:$\sigma_{post}^{predict}$ is the normalized tensor dot product between the observed and predicted post-mainshock stress tensors. I include only boxes for which the misfit is within the 95% confidence region of the inversion for at least one value of τ, in order to control data quality. **(B)** Stress magnitude versus depth. The solid lines indicate the best-fit deviatoric stress magnitude in each depth range, the dashed lines are an estimate of the 1σ confidence range based on the misfit curves in (A). The dotted lines indicate the range of predicted values for a strike-slip regime based on laboratory experiments.

segment	strike	σ_H rotation	D (m)	$\Delta\tau$ (bar)	$\Delta\tau/\tau$	τ (bar)
Johnson V.	N5W	-12±9^o	2±0.5	50±12	0.63 (0.25-1)	79 (38-250)
Homestead V.	N26W	15±9^o	3.5±0.5	88±12	0.67 (0.4-1)	130 (76-250)
Emerson	N40W	18±11^o	4±0.5	100±12	0.62 (0.35-0.85)	160 (100-320)
Camp Rock	N40W	-21±14^o	1±0.5	25±12	?	?

Table 2.1: The four segments of the Landers earthquake used to invert for deviatoric stress magnitude, τ. The average surface slip, D, is estimated from *Sieh et al.* [1993]. The stress drop, $\Delta\tau$, is computed from the definition $\Delta\tau = \mu\frac{D}{L}$, assuming a fault length scale, L, of 12 km (*i.e.*, the rupture broke the entire seismogenic crust) and μ=3x10^{10}N/m^2. Rotation is positive clockwise. Numbers in parentheses are the range of acceptable values. All segments are assumed to be vertical and rupture is assumed to be pure strike-slip.

Chapter 3 Stress State and the Strength of the San Andreas Fault

3.1 Introduction

To understand the mechanics of the southern California plate boundary region, it is important to constrain the strength of San Andreas Fault. The strength is defined as the maximum possible frictional resistance to slip. The strength and the shear stress acting on the fault may be variable on small length scales, as discussed in Chapter 2. Here I consider the average strength over length scales on the order of kms.

The San Andreas Fault is generally considered to be a weak fault. Laboratory experiments indicate that faults should have a coefficient of friction of 0.6-0.85 [*Byerlee*, 1978], which corresponds to a strength on the order of 1 kbar at seismogenic depths, assuming hydrostatic pore pressure. The lack of a heat flow anomaly along the San Andreas [*Brune et al.*, 1969; *Lachenbruch and Sass*, 1992] indicates that sliding friction is less than 100-200 bar, and that the fault is therefore weak in an absolute sense.

The San Andreas is also thought to be weak relative to other faults in the region, based on the apparent misorientation of the fault relative to the surrounding stress field. The regional maximum horizontal stress axis, σ_H, has been observed to be roughly perpendicular to the fault surface, indicating that relatively little shear stress is resolved onto the San Andreas compared to faults of other orientations [*Zoback et al.*, 1987; *Mount and Suppe*, 1992]. Since the San Andreas appears to operate at a lower level of shear stress than other faults, it is considered weak in a relative sense.

In this chapter, I re-examine the hypothesis that the San Andreas is weak in a relative sense. I use high-spatial-resolution stress orientations, obtained from the inversion of earthquake focal mechanisms, to test whether σ_H is at high angle to the

fault within a few km of the San Andreas in southern California.

3.2 Method

Stress orientation versus distance from the fault is determined for eight profiles across relatively straight segments of the San Andreas Fault (SAF), San Jacinto Fault (SJF), and Elsinore Fault (EF). Figure 3.1 shows the locations of the fault segments and the spatial extent of the events used in each profile. The earthquakes are from the relocated data set described in Chapter 1, and all occurred between 1981 and 1998.

All earthquakes within 1 km of each fault segment are inverted together to find the stress orientation very near the fault. The rest of the earthquakes along each profile are binned in groups of 100 based on perpendicular distance from the fault, and each group is inverted for principal stress direction. The focal mechanisms are inverted for stress using the method of *Michael* [1984, 1987b], which has been shown to produce accurate results with appropriate uncertainty estimates (Appendix A.)

3.3 Results

The direction of the maximum horizontal stress, σ_H, for each profile is shown in Figures 3.2 and 3.3. In general, σ_H makes an angle of $\sim 40^o$-50^o to the fault inside a zone along the fault, the width of this zone varying from $\sim$2 km to $\sim$30 km. Further away, it makes an angle of $\sim 60^o$-90^o to the fault. The high angles in the far-field are consistent with the observations of previous studies. However, the rotation of σ_H to low angle near the San Andreas is a new observation which contradicts the model of a relatively weak fault.

For fault segments subparallel to the relative plate motion (profiles A, F, G and H in Figures 3.2 and 3.3), far-field σ_H is typically $\sim 60^o$ to the fault strike. However, within 2-5 km of the Parkfield and Indio segments of the SAF (profiles A and G), the northern and southern SJF (profiles F and H), and the central and southern EF (profiles G and H), σ_H is at $\sim 40^o$ to the fault strike.

In the region of the compressional bend in the SAF (profiles B, C, D and E), far-field σ_H is typically $\sim 90^o$ to the fault strike. Near the Fort Tejon and San Bernardino segments of the SAF (profiles B and D), however, σ_H is at $\sim 40^o$ to the fault strike. The zone of stress rotation across the Fort Tejon segment is ~20-30 km wide, while that across the San Bernardino segment is ~5 km wide, but superimposed on a wider zone (~30 km) to the northeast where σ_H is $\sim 50^o$ to the fault. Previous studies of stress orientation along the SAF have also found a principal stress axis oblique to the Fort Tejon and San Bernardino segments [*Jones*, 1988; *Wyss and Lu*, 1995].

There are two segments without a clear stress rotation. The Mojave segment of the SAF (profile C) has a broad area (~50-90 km) in which σ_H is at approximately 60^o to the fault. Banning (profile E) is the only segment for which the observed σ_H is everywhere at high angle ($>60^o$) to the fault. The Banning segment has numerous strands, some non-vertical, unlike the rest of the southern California San Andreas system, and it is uncertain whether there is a single thoroughgoing fault [*Magistrale and Sanders*, 1996; *Seeber and Armbruster*, 1995]. A difference in stress state is not surprising, then, as this segment appears to be different from the rest of the fault system.

The resolution of the width of the observed stress rotation is dependent on the width of the data bins. Near the fault, the bin width is 2 km. Therefore, the widths of the narrowest (~2-5 km) zones are at the limit of the resolution, but the widths of the wider zones (>5 km) are well resolved.

The stress orientations along the fault appear to be robust and not artifacts of poor data quality or inadequate focal mechanism diversity. Results of inversions using only the best-constrained $\sim 1/3$ of the data set are very similar to the results for the whole data set (Figure 3.4A). Additionally, the mechanisms along the fault show considerable diversity, which is necessary for a reliable inversion (Figure 3.4B).

The observed stress rotations appear robust in that using different binning schemes (Figure 3.5) or a different inversion program (Figure 3.6) produces results which are in agreement with Figure 3.2 to within the 95% confidence regions. *Townend and Zoback* [2000] inverted the same focal mechanism data set using a different binning

technique, and used their observations to argue that there is not a stress rotation. However, when their observed stress orientations are displayed differently, as profiles across the San Andreas, it is apparent that these orientations agree very well with those found here (Figure 3.7). The similarity between the results of the the two studies demonstrates that the observed stress rotations are a robust feature of the focal mechanism data.

Similar stress orientation patterns are also observed if only events from limited depth intervals are used (Figure 3.8). However, the similarity may break down near the surface, as stress orientations inferred from shallow events ($\leq$2.5 km depth) do not indicate a stress rotation along the fault. Shallow borehole stress orientation measurements are highly scattered. A series of boreholes across the Mojave segment of the San Andreas imply a rotation to low angle near the fault [*Hickman et al.*, 1988; *Stock and Healy*, 1988], qualitatively similar to the rotations observed here. Other borehole stress orientations appear inconsistent with my observations. For example, the low-angle, right-lateral stress orientations observed along the San Bernardino segment of the SAF contrast with left-lateral stress orientations measured to 3.5 km depth in the Cajon Pass borehole approximately 5 km northeast of the San Andreas [*Zoback and Healy*, 1992; *Shamir and Zoback*, 1992]. However, shear-wave anisotropy observed at Cajon Pass implies that σ_H at seismogenic depths is at $\sim 45^o$ to the fault in a right-lateral sense [*Liu et al.*, 1997], consistent with the observations in Figure 3.2.

3.4 Discussion

Observations of stress orientation very near to the San Andreas contradict the model of a relatively weak fault. The observed $\sim 40^o$-50^o angle between σ_H and the fault strike means that the shear stress on the fault is approximately equal to the deviatoric stress magnitude. The San Andreas must therefore be of comparable strength to its immediate surroundings. There are two possibilities: that the San Andreas is strong, or that the surroundings are weak. The stress orientation information alone cannot

distinguish between these two models.

Scholz [2000] interpreted this stress rotation, originally published by *Hardebeck and Hauksson* [1999], to mean that the San Andreas is actually a strong fault. A strong fault driven from below by a shear zone would produce upper crustal stress orientations similar to those observed here. However, a strong San Andreas is at odds with heat flow observations [*Brune et al.*, 1969; *Lachenbruch and Sass*, 1992].

Hardebeck and Hauksson [1999] interpreted the stress rotation as a ~2-30 km wide zone of weakness due to elevated fluid pressure, based on the fault fluid model of *Rice* [1992], which predicts such a rotation. *Scholz* [2000] noted that there is a force balance problem for a wide zone of high fluid pressure, since the model predicts an elevated vertical stress which must be balanced by vertical shear stress on fault-parallel planes. If the deviatoric stress outside the high-pressure fluid zone is high, this shear stress is unacceptably large.

Another possibility is that the San Andreas is a weak fault in a weak crust, as suggested by the low deviatoric stress magnitude found in Chapter 2. The San Andreas may have a resolved shear stress comparable to the estimated deviatoric stress, ~100 bar, and be consistent with the upper bound on frictional stress required by heat flow measurements. Figure 3.9 illustrates on Mohr circle diagrams several models for the San Andreas: a strong fault model, two models for a weak fault in a strong crust, and two models for a weak fault in a weak crust. The latter two models are preferred because they are the only cases consistent with both a low angle of σ_H to the San Andreas and a low resolved shear stress on the fault plane.

If the San Andreas is weak in an absolute sense but not a relative sense, this implies that all the active faults in the southern California plate boundary region operate at low stress. Three classes of fault-weakening models have been proposed: high-pressure fluids [*Hubbert and Rubey*, 1959; *Rice*, 1992]; inherently weak fault zone materials, although most candidate minerals have been eliminated by laboratory testing [*Moore et al.*, 1996; *Morrow et al.*, 1992]; and dynamic weakening [*Heaton*, 1990; *Melosh*, 1996; *Andrews and Ben-Zion*, 1997]. These models were formulated to explain the weakness of mature faults with well-developed gouge zones, like the San Andreas, and

may need to be modified to apply to lesser-developed faults.

The rotation of σ_H across the San Andreas may simply reflect interseismic stress accumulation. If the deviatoric stress is on the order of earthquake stress drop, σ_H should rotate during the seismic cycle, from a high angle immediately following the stress release of a large earthquake to a lower angle later in the interseismic period as the fault is reloaded. The last major earthquake on the San Andreas in southern California was in 1857, so all the fault segments are currently late in the cycle and σ_H is at low angle to the fault.

This model predicts the width of the zone of rotation to roughly correspond to the width of the interseismic strain accumulation, which it does. In the western and central Transverse Ranges (*i.e.*, the Fort Tejon and Mojave segments of the San Andreas) where the zone of stress rotation is widest (~20-90 km), a wide zone of strain accumulation (>40 km) is observed geodetically [*Lisowski et al.*, 1991]. In the southeastern San Andreas system (*i.e.*, the San Bernardino and Indio segments and the San Jacinto and Elsinore faults) where the zone of stress rotation is narrow (<20 km), the strain accumulation is also more localized (<20 km) [*Lisowski et al.*, 1991].

The observed stress rotations imply that the San Andreas is driven from below. If it were driven from the side, *i.e.*, if the shear stress were transmitted through the upper crust, there would be significant shear stress on San Andreas-parallel planes in the far field, inconsistent with the high angle of σ_H to the fault observed at ~100 km distance. This means only that the driving stresses are not transmitted through the upper crust, they may be transmitted though the lower crust or upper mantle. Localized deformation beneath the San Andreas would then drive the fault from below.

3.5 Conclusions

Stress orientations obtained from the inversion of earthquake focal mechanisms were used to test the hypothesis that the maximum horizontal stress, σ_H, is at high angle to the San Andreas Fault in southern California. Stress orientations along eight

profiles across the fault indicate that while σ_H is at high angle ($\sim 60^o$-90^o) to the fault in the far field, within a few km of the fault it rotates to lower angle ($\sim 40^o$-50^o). This observation is robust with respect to data selection, binning method and stress inversion technique.

The low angle of σ_H to the fault in the near field contradicts the model that the San Andreas is weak relative to its surroundings. This observation, combined with the low deviatoric stress levels found in Chapter 2, suggests that the San Andreas is weak in an absolute sense, but not in a relative sense. If the deviatoric stress level is low, the rotation of the stress tensor near the San Andreas may simply reflect interseismic stress accumulation.

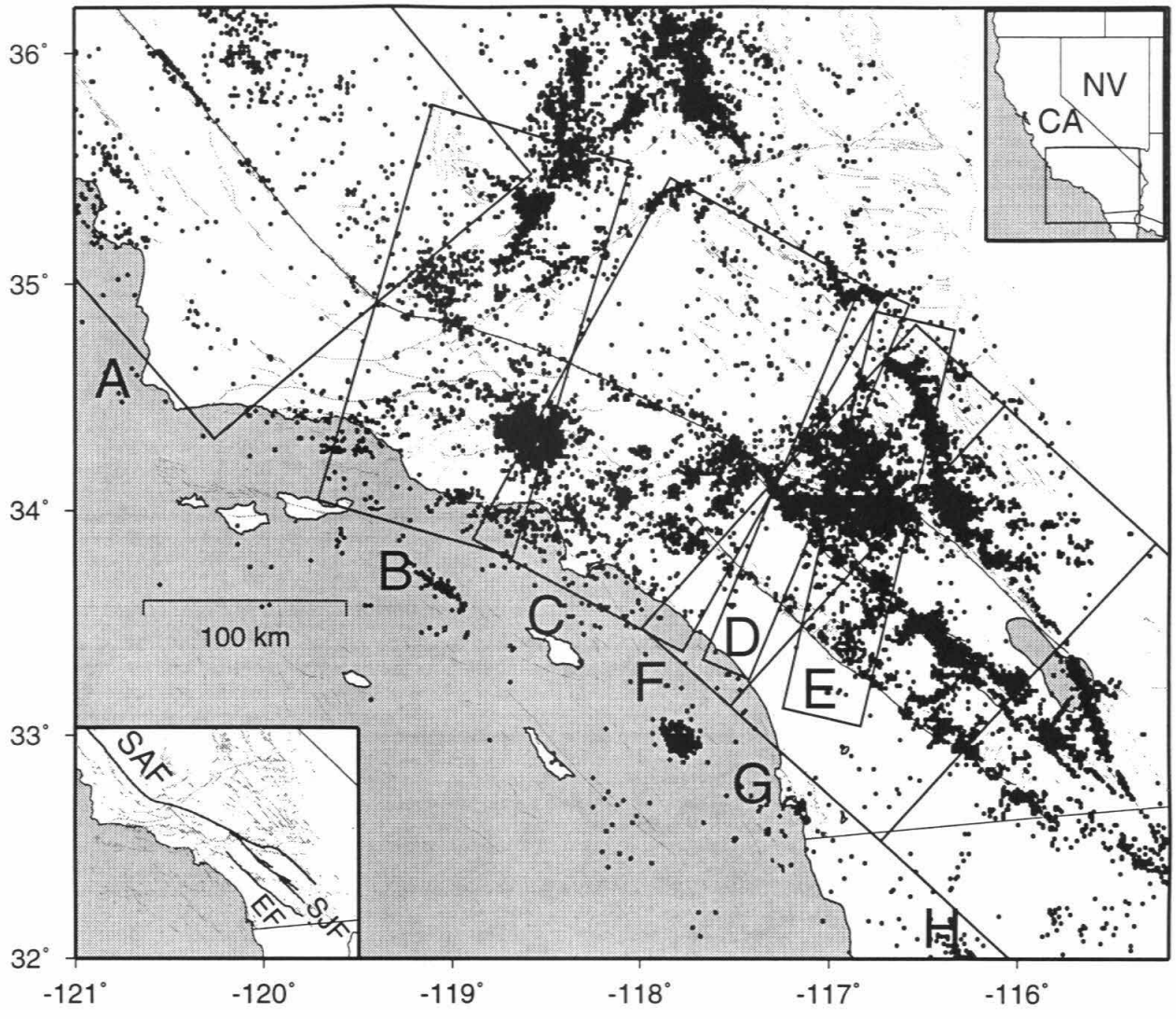

Figure 3.1: Map view of ~50,000 southern California earthquakes occurring between 1981 and 1998. The events were relocated and first-motion focal mechanisms found using the three-dimensional velocity model of *Hauksson* [2000]. The inset indicates the location of the three major faults of the right-lateral San Andreas fault system in southern California, the San Andreas (SAF), the San Jacinto (SJF), and the Elsinore (EF). The boxes indicate the locations of the stress orientation versus distance profiles shown in Figure 3.2.

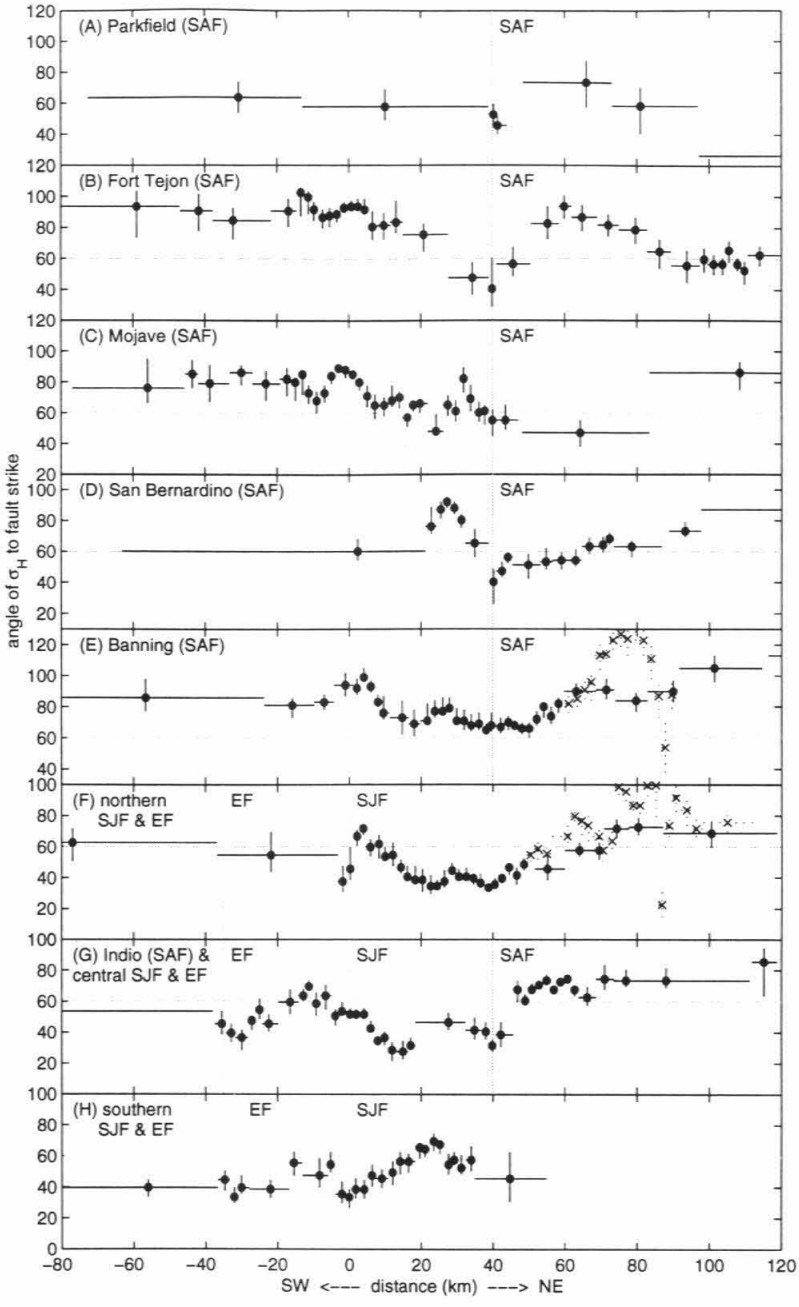

Figure 3.2: Orientation of σ_H, the maximum horizontal stress, relative to the strike of the fault segment versus perpendicular distance from the fault (NE positive.) The locations of the profiles are shown in Figure 3.1. The earthquakes used for each profile are binned in groups of 100 based on their perpendicular distance from the fault, and inverted for principal stress orientation [*Michael*, 1984, 1987b]. Angles $>90^o$ indicate left-lateral stress orientations. The horizontal error bars indicate the extent of the bins, and the vertical error bars the 95% confidence interval of the inversion results. The vertical gray lines indicate the approximate location of the traces of the major faults. Horizontal dashed line at 60^o for reference. (The crosses with dotted error bars are post-Landers stress orientations, when different from pre-Landers orientations.)

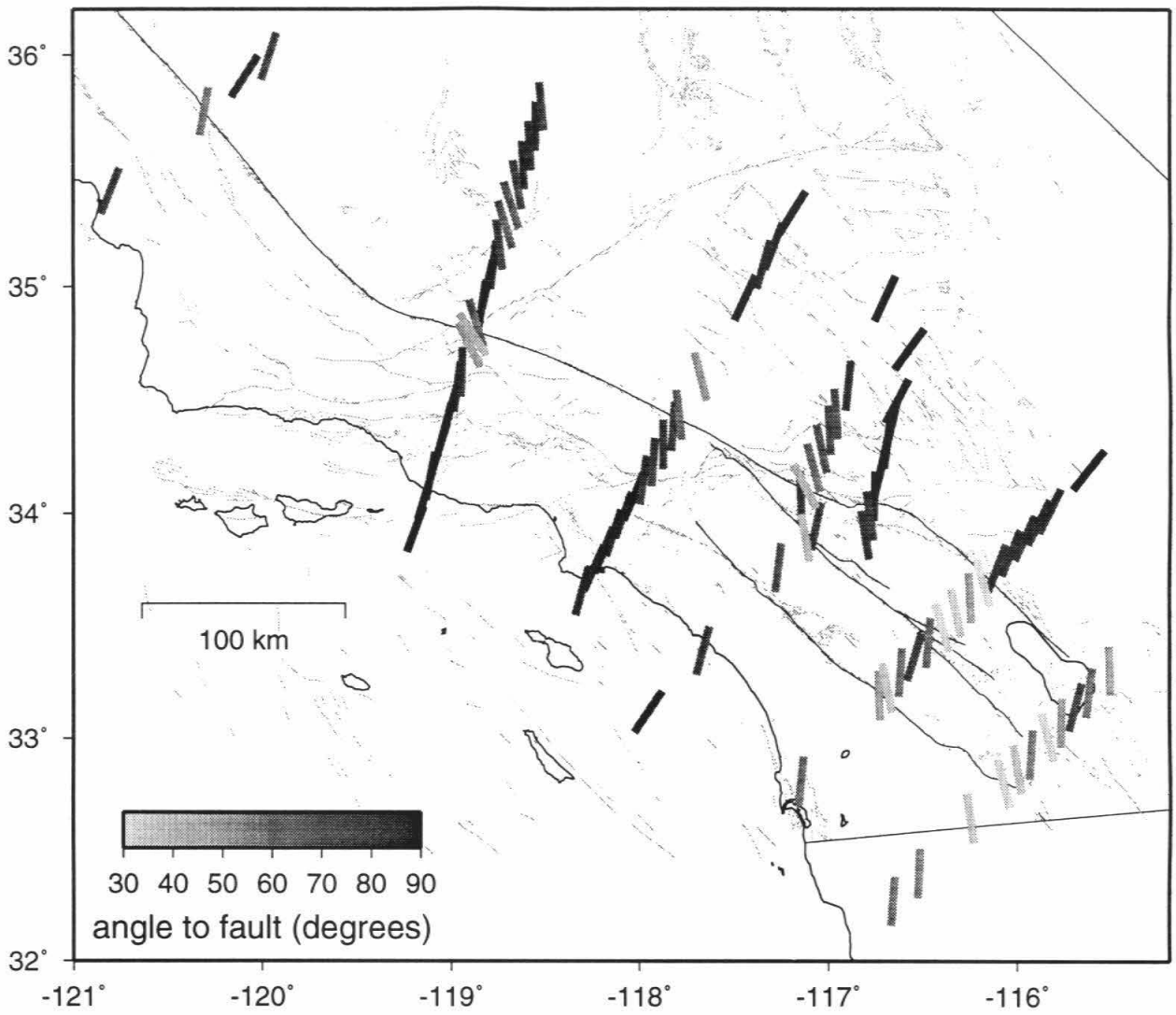

Figure 3.3: The orientation of the maximum horizontal stress, σ_H, along profiles across the San Andreas fault system. The bar orientation indicates the σ_H direction and the shade denotes the angle σ_H makes with the strike of the nearest major fault segment. For clarity, only representative orientations from the full profiles (Figure 3.2) are shown.

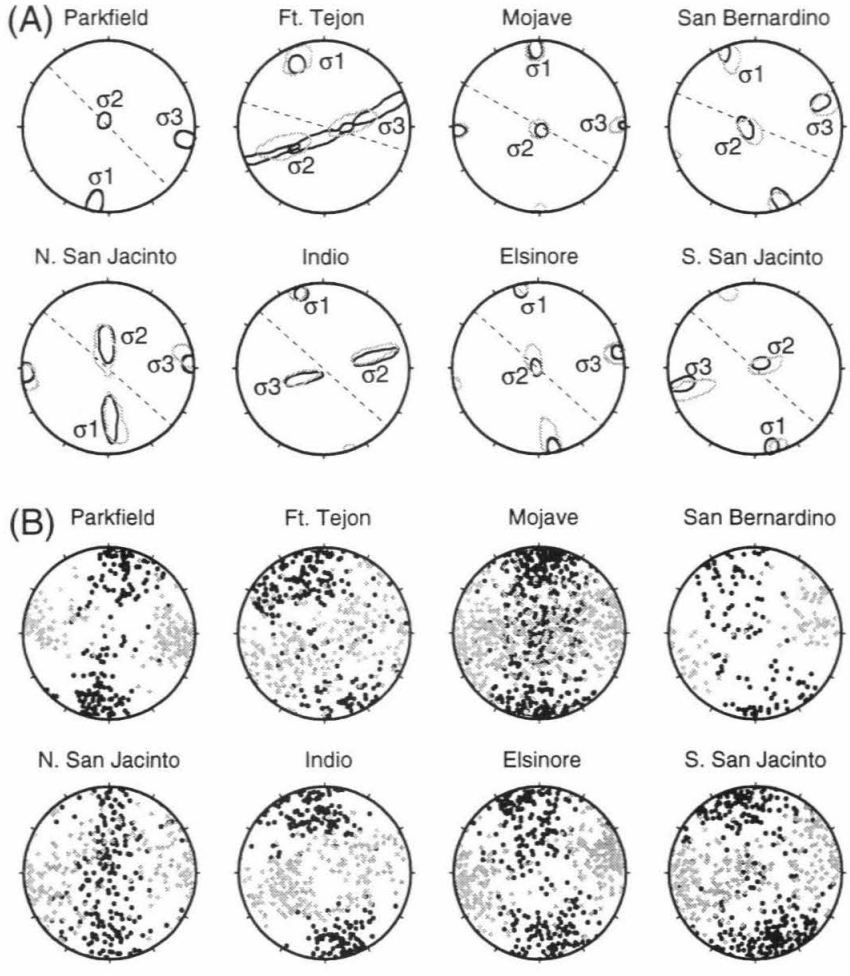

Figure 3.4: Three-dimensional stress orientations along the fault, where σ_H is observed to be at low angle ($\leq 60^o$) to the fault (Figure 3.2). For the Parkfield segments, events in an 8 km wide zone are used; Ft. Tejon, 23 km; Mojave, 10 km; San Bernardino, 4 km; N. San Jacinto, 4 km; Indio, 2 km; Elsinore, 3 km; and S. San Jacinto, 5 km. (A) The 95% confidence regions for the maximum (σ_1), intermediate (σ_2), and minimum (σ_3) principal stress directions on a lower-hemisphere equal-angle projection. Black: inversion results for all of the earthquakes inside the zone. Grey: inversion results for the best-constrained mechanisms (M$\geq$2 events with at least 20 first-motion picks, which constitute approximately one third of the data set. There are an inadequate number of well-constrained events for inversion at Parkfield.) The dashed line indicates the orientation of the fault. (B) The distribution of the compressional (black) and tensional (grey) axes of the focal mechanisms used in the inversion. The diverse set of mechanisms indicates that the observed stress orientations along the fault are not an artifact of inverting a data set comprised only of similar fault-parallel, strike-slip mechanisms.

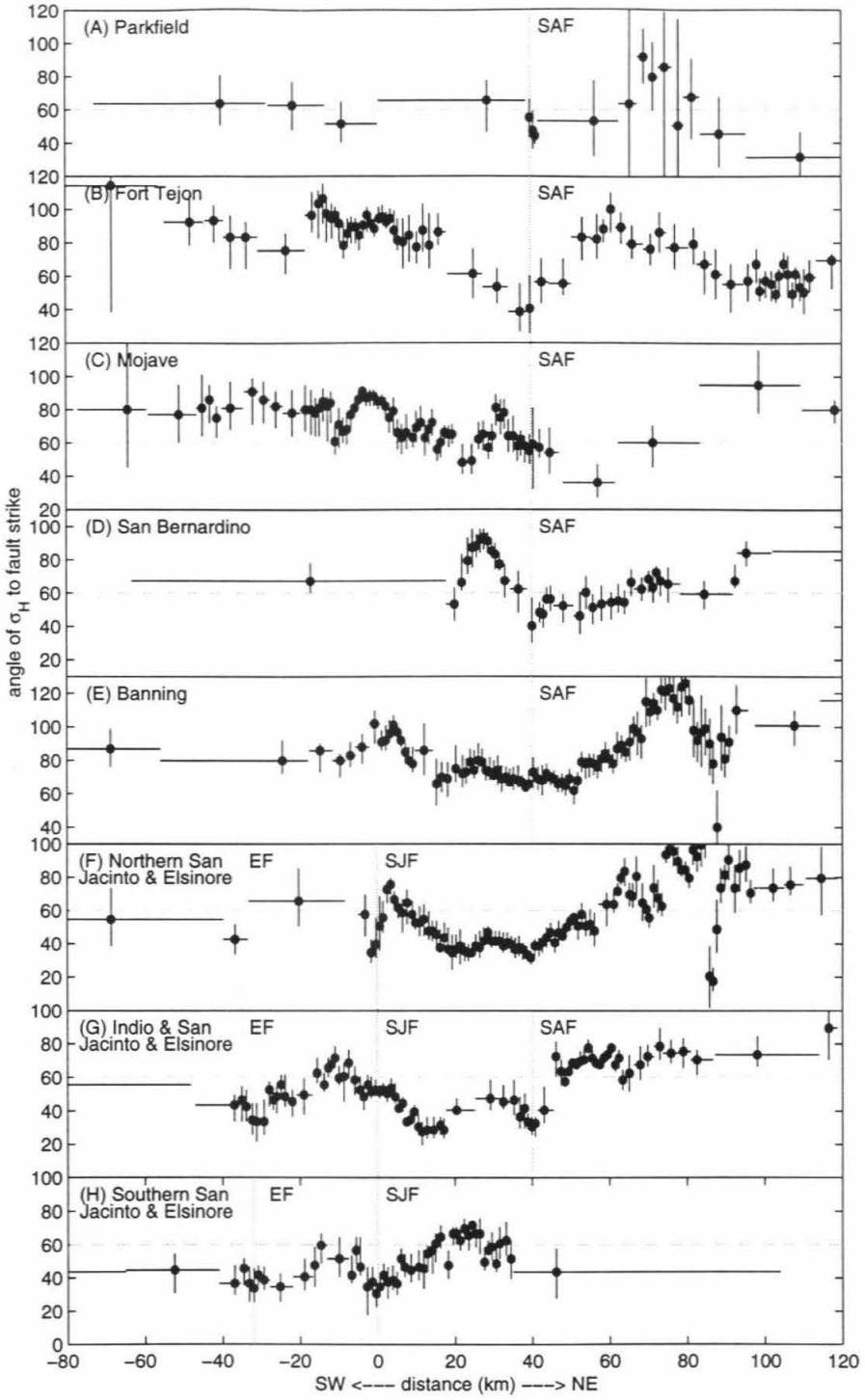

Figure 3.5: Orientation of σ_H, the maximum horizontal stress, relative to the strike of the fault segment versus perpendicular distance from the fault (NE positive.) As in Figure 3.2, except that the events are binned in groups of 50, and separate pre- and post-Landers inversions were not performed.

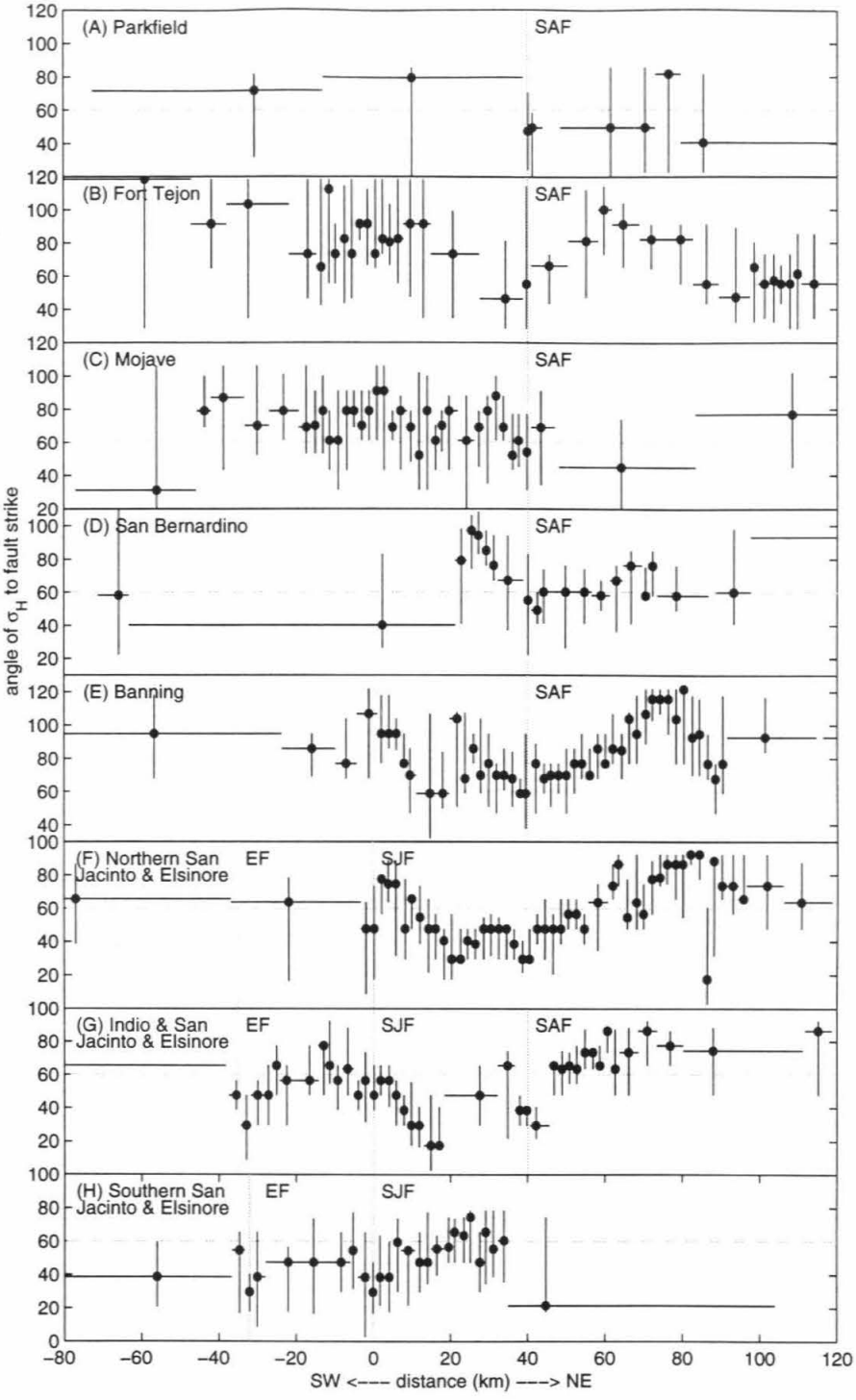

Figure 3.6: Orientation of σ_H, the maximum horizontal stress, relative to the strike of the fault segment versus perpendicular distance from the fault (NE positive.) As in Figure 3.2, except that the events were inverted for stress using the method of *Gephart and Forsyth* [1984], and separate pre- and post-Landers inversions were not performed.

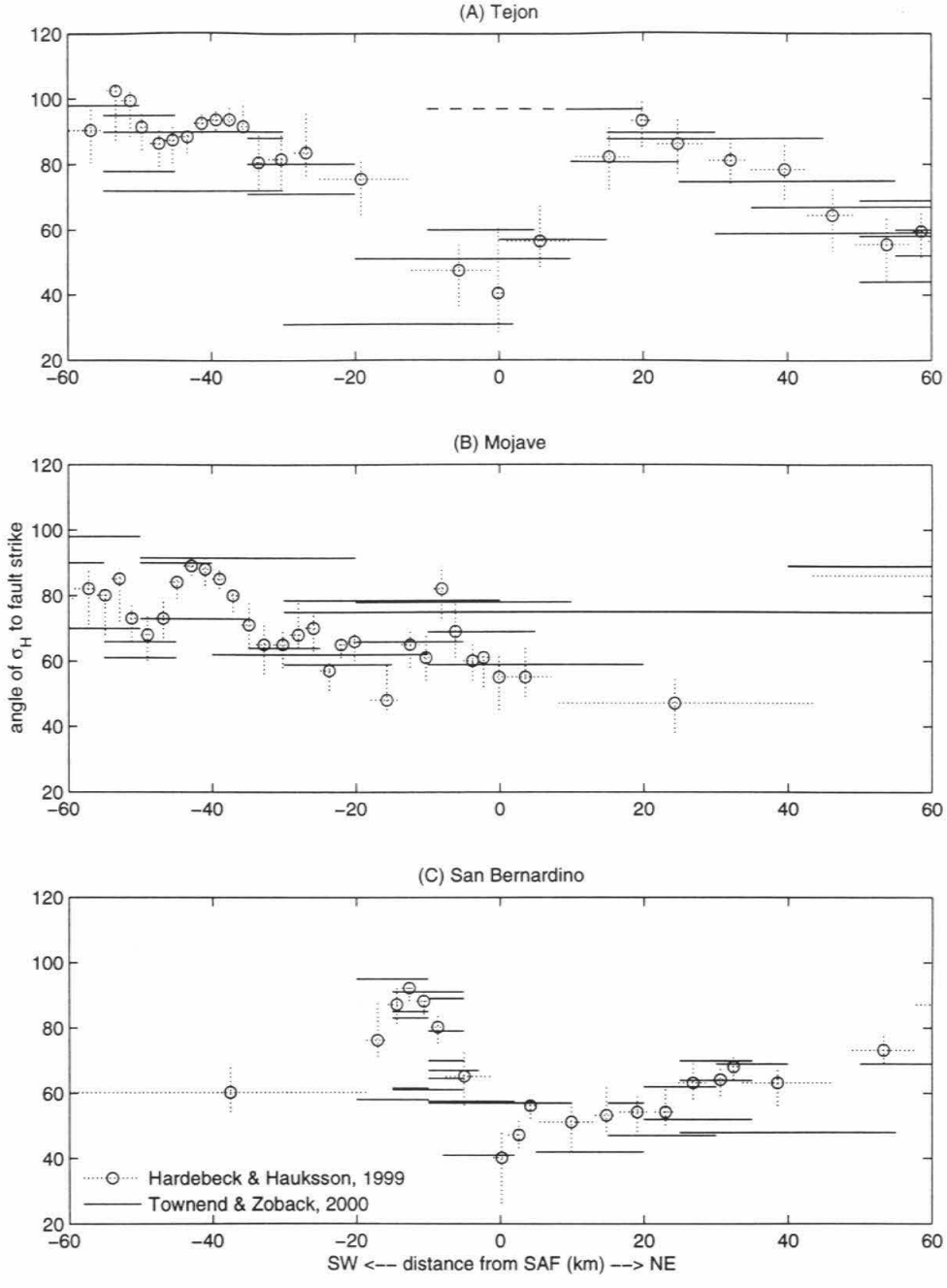

Figure 3.7: Profiles of σ_H orientation relative to the strike of the San Andreas versus distance from the fault, using two different binning techniques. The solid lines are orientations measured from Figure 4 of *Townend and Zoback* [2000], who invert events in variable-sized square bins. The horizontal length of the lines represent the spatial extent of the bins in the fault-normal direction. One bin which crosses the Tejon segment of the fault contains only events in the opposite corner of the box, the empty portion of the box is indicated with a dashed line. The circles with the dotted error bars are from Figure 3.2.

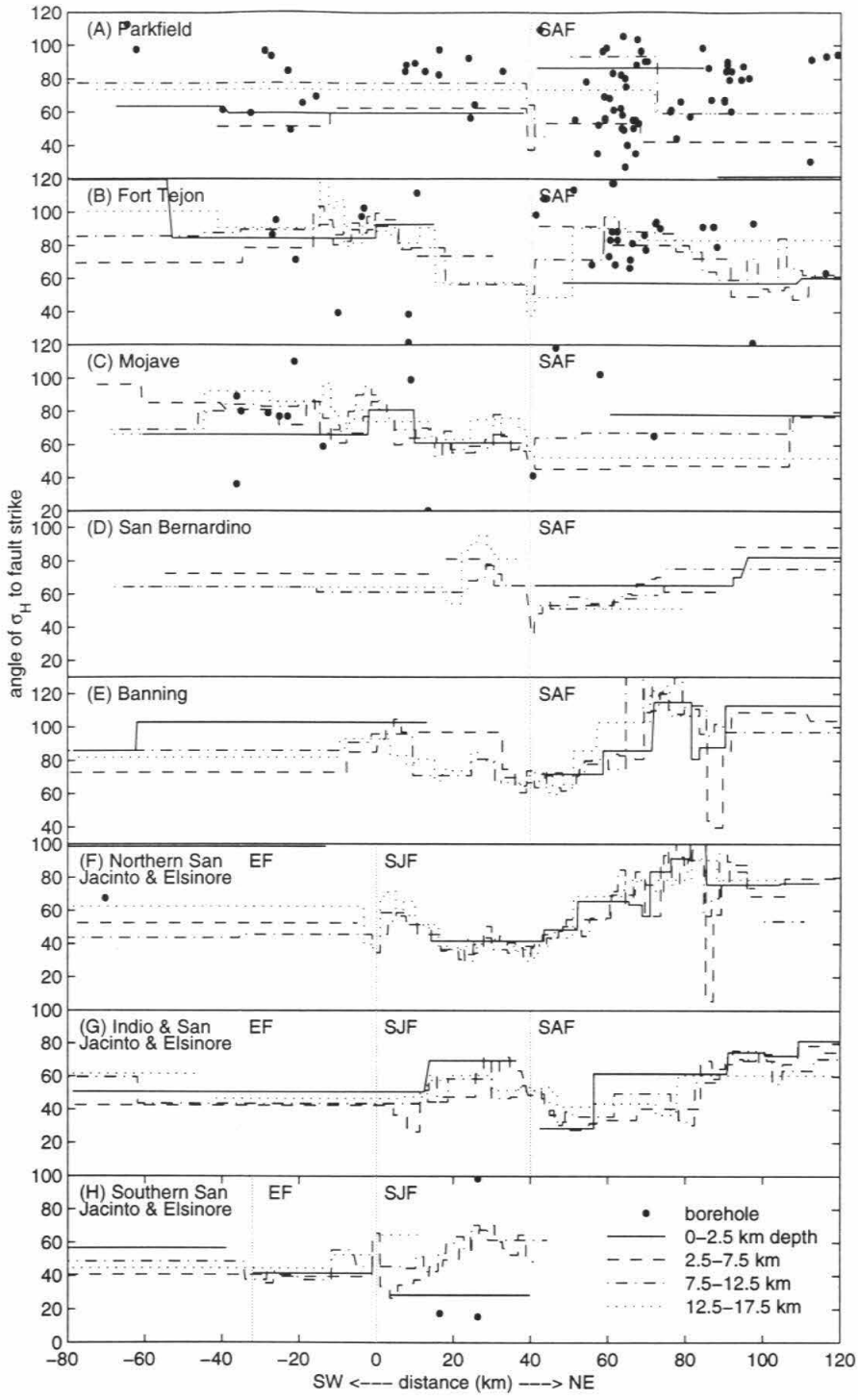

Figure 3.8: Orientation of σ_H, the maximum horizontal stress, relative to the strike of the fault segment versus perpendicular distance from the fault (NE positive.) Four profiles are shown for each fault segment, each using only events from the corresponding depth range. Solid dots indicate borehole measurements from the World Stress Map project [*Zoback*, 1992] (only the borehole data from the database is used).

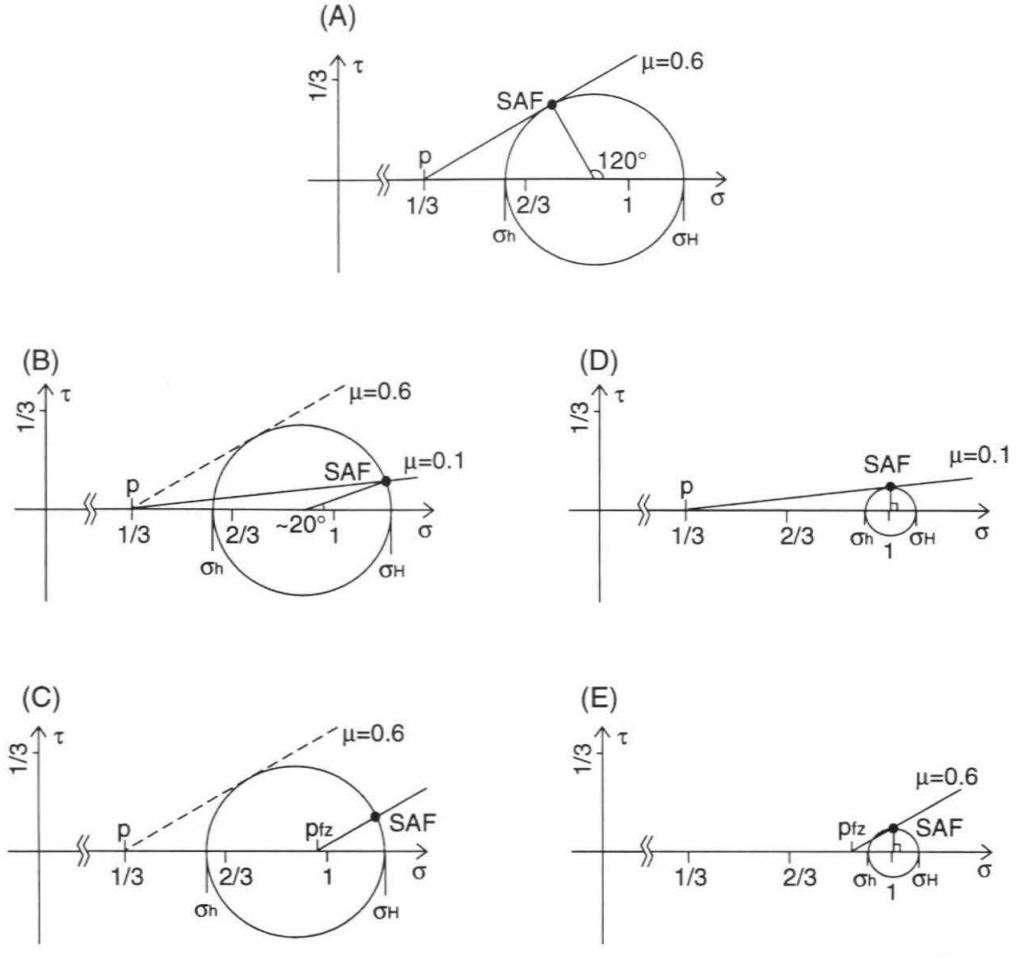

Figure 3.9: Mohr circle diagrams representing five models for the San Andreas Fault. σ_H and σ_h are the maximum and minimum horizontal stresses, respectively. The units on the axes are the fraction of the lithostatic load. SAF indicates the orientation of the San Andreas; p, hydrostatic pore pressure; p_{fz}, elevated fault zone pore pressure; and μ, the coefficient of friction corresponding to the shown failure envelope. (A) A strong fault, consistent with the predictions of laboratory friction experiments. (B) A weak fault, due to low μ, in a high-stress crust. (C) A weak fault, due to high-pressure fluids, in a high-stress crust. A more complex model is required if tensile failure is not allowed to occur, see *Rice* [1992]. (D) A weak fault, due to low μ, in a low-stress crust. (E) A weak fault, due to high-pressure fluids, in a low-stress crust.

Chapter 4 Earthquake Stress Drop and Background Stress

4.1 Introduction

Faults rupture in response to crustal stress. The slip which occurs during an earthquake, and therefore the stress drop of the event, should be related to the stress and the frictional parameters of the fault. Since earthquake stress drops can be measured, they can be used to study the stress state and the frictional properties of faults.

A simple representation of friction for a crack model consists of a static coefficient of friction, μ_s, which controls the initial failure stress, and a dynamic coefficient of friction, μ_d, which controls the stress level at which slip ceases. An earthquake static stress drop is defined as:

$$\Delta\sigma = \tau_{pre} - \tau_{post} \tag{4.1}$$

the difference between the shear stress on the fault before (τ_{pre}) and after (τ_{post}) the earthquake. Relating the stress drop to the effective normal stress, σ_{eff}, and frictional coefficients:

$$\Delta\sigma = \mu_s\sigma_{\text{eff}} - \mu_d\sigma_{\text{eff}} = (\mu_s - \mu_d)\sigma_{\text{eff}} \tag{4.2}$$

This simple model therefore predicts that stress drop should scale with the effective normal stress on the fault.

One way to test this prediction is to investigate whether static stress drop increases with depth. Assuming hydrostatic pore pressure, the effective normal stress on faults of a given orientation should increase approximately linearly with depth. Some studies have found an increase in stress drop with depth. For the Big Bear, California, aftershock sequence, *Jones and Helmberger* [1996] find that events shallower than 12 km had stress drops in the range of 10 to 100 bars, averaging about 55 bars, while

events deeper than 12 km had stress drops exceeding 100 bars and averaging 200 bars. *Song and Helmberger* [1997], studying M_L 4.0 to 5.6 aftershocks of the Northridge, California, earthquake, find that the highest stress drops occur below 8 km depth.

Other studies, however, have not found an increase in stress drop with depth. *Jones and Helmberger* [1998] find that stress drop does not increase with depth for M_W >4 earthquakes in the Eastern California Shear Zone. *Smith and Priestley* [1993] also find no correlation between stress drop and depth for M_L 2.8 to 4.2 earthquakes in Round Valley, California.

In this chapter, I investigate whether stress drop increases with depth for small (M_L=2.5-4.0) aftershocks of the Northridge earthquake. The Northridge sequence is ideal for studying stress drop variations with depth because the aftershocks extend below 20 km depth.

4.2 Data and Methods

Time-domain pulse widths measured from seismograms are used to estimate the static stress drops of 279 M_L 2.5 to 4.0 aftershocks of the 1994 Northridge, California, earthquake (Figure 4.1). The events were relocated using the three-dimensional seismic velocity model of *Hauksson and Haase* [1997], and arrival times from Southern California Seismic Network (SCSN) stations. Only events in the M_L 2.5 to 4.0 range are used because static stress drop is estimated from seismograms and the waveforms of smaller events may not have clear arrivals and those of larger events are likely to be complicated by source complexity and directivity effects. The aftershocks were selected for clarity of recordings of the initial P-wave pulse.

4.2.1 Computing Stress Drop

Static stress drop, $\Delta\sigma$, is calculated from a relation for a circular fault [*Brune*, 1970]:

$$\Delta\sigma = \frac{7M_o}{16r^3} \tag{4.3}$$

where r is the radius of the fault and M_o the seismic moment. It is easily verified, from the definition of seismic moment $M_o = \mu r^2 D$ (where μ is the shear modulus and D is the average slip) and the stress-strain relation $\Delta\sigma \sim \mu\frac{D}{r}$, that $\Delta\sigma \sim \frac{M_o}{r^3}$. The constant of proportionality reflects the assumed shape of the rupture, and is unimportant in the study of relative stress drops.

Moment can be estimated from local magnitude, M_L, from an empirical relationship for Southern California earthquakes [*Thatcher and Hanks*, 1973]:

$$logM_o = 1.5M_L + 16.0 \tag{4.4}$$

with M_o in dyne-cm. The slope constant in Equation 4.4 appears to be slightly greater than 1.5 for the Northridge aftershocks sequence when the long-period moments of M_L 4.0 to 5.6 events are determined from waveforms [*Song and Helmberger*, 1997].

The radius of a circular fault rupturing uniformly outward from the center, r, is related to the duration of the time function of the rupture, τ, by [*Frankel and Kanamori*, 1983; *Boatwright*, 1980]:

$$r = \frac{\tau v}{1 - (v/\alpha)sin\theta} \tag{4.5}$$

where v is the rupture velocity, α is the P-wave velocity and θ is the takeoff angle relative to the fault. The relationship $r \approx \tau v$ clearly equates the rupture length with the velocity of rupture times its duration, while the denominator of Equation 4.5 is a correction for the geometry of the observer.

I use a rupture velocity of $v = 0.75\beta$, and assume that the S-wave velocity, β, is proportional to the P-wave velocity, α, by the relation: $\beta = 0.6\alpha$. I use a one-dimensional P-wave velocity model (Table 4.1) adapted from *Hauksson and Haase* [1997] and *Hauksson et al.* [1995a]. The takeoff angle relative to the fault, θ, is arbitrarily set to $\pi/4$. Because I am examining relative stress drops, uncertainties in the constants used should not significantly affect the results.

Broadband velocity seismograms from the Calabasas TERRAscope station (CALB)

and three Southern California Earthquake Center (SCEC) temporary stations (Figure 4.1) are used to estimate the rupture duration of an event based on the width of the initial P-wave pulse. The azimuthal coverage isn't complete due to the sparsity of stations in the mountains to the north and northeast. The seismograms are bandpass filtered between 0.4 and 40 Hz. The width of the initial P-wave pulse is measured on the vertical component of clean non-nodal records, measuring from the emergence of the signal from the background noise to the first zero crossing. Since none of the source-receiver pairs are more than about 40 km apart, this first arrival should always be the direct arrival.

There appears to be a general broadening of the average pulse with hypocentral distance, presumably due to attenuation of high frequency seismic waves. The increase in pulse width appears to be approximately $1.6\text{x}10^{-4}$ seconds per km hypocentral distance. I correct for this effect by subtracting $1.6\text{x}10^{-4}$ s per km distance from each pulse width measurement. The measurements at each station are uniformly shifted so that the mean rupture duration for the entire data set is the same for each station, in order to eliminate bias from differences in station coverage.

The corrected rupture durations are in the range of 0.024 to 0.34 s, and the corresponding fault radii are in the range of 0.1 to 1.1 km. From the estimated source size and moment, I determine the static stress drop for each event as observed from each station, and determine a combined estimate by averaging these values in log domain. The combined estimates of stress drop range from 0.04 bar to 70 bars, with a log average of 1.3 bars (Figure 4.2 and Table 4.2).

4.2.2 Uncertainty Estimates

The stress drop calculation is clearly most sensitive to the estimation of rupture duration, since, in Equation 4.3, $\Delta\sigma$ goes as $1/r^3$, and hence as $1/\tau^3$. It is therefore important to determine if the wide range of $\Delta\sigma$ values obtained is an artifact of uncertainties in the measurement of τ. The measurements of τ are generally consistent across the 4 stations, usually to within 0.05 s, and the stress drop as observed from

each station is usually within a factor of 3 of the combined stress drop estimate for that event (Figure 4.3). An order of magnitude difference in stress drop corresponds to a visible difference in pulse width. Both events shown in Figure 4.4 have M_L =2.9 and are approximately 24 km from the station LA00 where they are recorded. The event in the top record has a longer P-wave pulse at this station, about 0.15 s, while the event in the lower record has a shorter pulse, about 0.05 s. The lower record clearly has greater high-frequency content than the upper record. When stress drops are combined for all stations, the stress drop of the first event is about 0.9 bar, and that of the second is about 10 bar. This evidence suggests that not all of the scatter in $\Delta\sigma$ estimates come from uncertainty in τ, as further supported by a quantification of measurement uncertainty.

Measurement error bounds are computed for the stress drops as observed at each station. The measurement error of event magnitude is taken to be 0.5 magnitude units. The digital seismogram sample spacing, 0.0125 s for CALB and 0.005 s for the SCEC temporary stations, is used as the pulse width measurement error. The values are used to determine a maximum and minimum stress drop estimate for each event as recorded at each station, which define the measurement error bounds.

There are two kinds of uncertainties which go into the error bounds for the combined static stress drop estimate: measurement uncertainty for each event observed at each station, as described above, and uncertainty due to differences between the observations for the same event at different stations. The latter uncertainty can be characterized as the 95% confidence interval for the mean:

$$\pm 1.96 \frac{\sigma}{\sqrt{N}} \tag{4.6}$$

where σ is the standard deviation of the observations for a given event at the stations, and N is the number of stations recording the event. The measurement uncertainty can be written analogously, if we think of the measurement error bar as a 95% confi-

dence interval which should narrow with an increasing number of measurements:

$$\pm\frac{m}{\sqrt{N}} \tag{4.7}$$

where m is the mean measurement error of the stress drop estimates for a given event. These two 95% confidence intervals are calculated in the log domain, and are combined to determine the 95% confidence interval for the average static stress drop:

$$\pm\sqrt{\frac{(1.96\sigma)^2 + m^2}{N}} \tag{4.8}$$

Most of these error bars are less than a factor of 5, indicating that measurement uncertainty is not responsible for the 3 orders of magnitude scatter in stress drop estimates. It appears, then, that there is a significant amount of actual scatter in the static stress drops of the aftershocks.

4.3 Observations

4.3.1 Stress Drop Variations with Magnitude

The combined static stress drop estimates for the aftershocks, along with error bars, are shown versus magnitude in Figure 4.5. There are several orders of magnitude scatter in most magnitude ranges, but static stress drop increases with magnitude over the entire magnitude range with a correlation coefficient of 0.7. It is possible that this relationship may be an artifact of the method, since $\Delta\sigma$ as calculated in Equation 4.3 depends on M_o. If M_o were overestimated for large events and underestimated for small ones, that is if the slope constant in Equation 4.4 were too large, an increase in stress drop with magnitude would be observed. This is probably not the case, however, since the work of *Song and Helmberger* [1997] suggests that, if anything, the constant used here is too low.

4.3.2 Stress Drop Variations with Depth

In Figure 4.6, static stress drop, along with error bars, is shown versus depth. There is much scatter in the estimates at all depth ranges. The scatter can be somewhat reduced by removing the trend with magnitude (Figure 4.7), which is roughly $log\Delta\sigma \approx 2M_L$ (Figure 4.5). For the majority of events, those between 5 km and 15 km depth, there is no observed systematic increase in minimum, maximum or average stress drop with depth.

The maximum stress drop, however, appears to scale linearly with depth in the upper 5 km. With the exception of two outliers, the maximum observed stress drops from 0 to 5 km depth are fit well by a linear increase with depth equivalent to ~1% of lithostatic pressure (Figure 4.7). However, below 5 km depth, the maximum observed stress drop does not appear to continue increasing with depth.

For events deeper than 15 km, the observed stress drops appear higher on average than for shallower events. I perform a Student's t test in order to determine if the difference between the mean stress drops (in log domain, and after the trend in stress drop with magnitude is removed) of events at depths between 5 and 15 km and of events at depths greater than 15 km is statistically significant. I use the methodology of *Press et al.* [1986] for distributions with possibly different variances, which essentially determines whether or not the sample means of the two distributions are within a standard error (the uncertainty of the population mean) of each other. The null hypothesis, that the static stress drops of events at depth between 5 and 15 km and at depths greater than 15 km come from populations with the same mean, can be rejected at the 95% confidence level.

The observed change in average stress drop at 15 km depth is primarily due to an increase in the lowest observed stress drop. This phenomenon is most pronounced for the observations at CALB (Figure 4.6a) and LA00 (Figure 4.6d), although it is seen at all stations. Below about 15 km depth, low stress-drop events ($\Delta\sigma$ <1 bar) appear to be "missing" (Figure 4.7). This is probably not due to a bias in data selection, since deep events in this magnitude range should have clean seismograms regardless

of stress drop. The trend of stress drop with magnitude was removed prior to the statistical test, so the increase in apparent minimum stress drop at 15 km depth cannot be due to a disproportionate number of higher magnitude (and hence higher stress drop) events at depth.

4.3.3 Mainshock-induced Stress Changes

I also test whether the static stress changes due to the mainshock may be controlling the aftershock stress drops. The static stress change tensor for an elastic half-space was computed at the locations of the aftershocks used in this study using the Northridge mainshock slip model of *Wald et al.* [1996] and the program ELFPOINT by Robert W. Simpson (based on the subroutines of *Okada* [1992]). The change in shear stress in the direction of slip (which is the same for both nodal planes, so there is no fault plane ambiguity) was computed for events for which first-motion focal mechanisms could be found. The mechanisms were computed from SCSN first-motion data using the FPFIT software package [*Reasenberg and Oppenheimer*, 1985]. There is no correlation between the observed static stress drops and calculated changes in shear stress in the direction of slip (Figure 4.8). Mainshock induced static stress changes appear not to be an important controlling factor in static stress drop.

4.3.4 Spatial Variations in Stress Drop

Several studies of stress drop in aftershock sequences have found that aftershocks along the mainshock fault plane tend to have lower stress drops than events occurring farther from the main rupture [*Jones and Helmberger*, 1998; *Smith and Priestley*, 1993; *Hough et al.*, 1991]. If stress drop scales with the level of shear stress on the fault plane, lower stress drop events should occur where the mainshock has relieved a significant amount of shear stress. This is equivalent to predicting that stress drop should be low for events with large negative static stress changes, which is not the case for the Northridge data (Figure 4.8). Mainshock induced stress increases and decreases do not appear to affect static stress drop, and therefore no spatial patterns

related to the mainshock are observed.

4.4 Discussion

4.4.1 Static Stress Drop

The estimated static stress drops for M_L 2.5 to 4.0 aftershocks of the Northridge earthquake, ranging from 0.04 bar to 70 bars, are comparable to stress drops found for some other events of similar magnitude. For example, M_L 2.3-4.0 earthquakes in New England were found to have $\Delta\sigma$=2.6-20.1 bar [*Feng and Ebel*, 1996]; M_L 2.0-3.5 aftershocks of the Coalinga earthquake, $\Delta\sigma$=0.5-80 bar [*Lindley and Archuleta*, 1992]; M_L 2.0-4.9 earthquakes in the Seattle area, $\Delta\sigma$=0.4-25 bar [*Frankel et al.*, 1999]; JMA magnitude 3.5-4.9 events in Hokkaido, $\Delta\sigma$=0.03-30 bar [*Fujita et al.*, 1995]; M_D 1.4-3.9 earthquakes near Parkfield, $\Delta\sigma$=2-30 bar [*O'Neill*, 1984]; and M_L events near San Juan Bautista, $\Delta\sigma$=1-10 bar [*Bakun and McLaren*, 1984].

However, these stress drops average at least an order of magnitude lower than those found in some other studies of similar-sized earthquakes. For instance, *Frankel and Kanamori* [1983], who use a method similar to that used here, find an average stress drop for small Southern California earthquakes of 170 bars, greater than any stress drops observed in this study. *Abercrombie and Leary* [1993] and *Abercrombie* [1995] compile stress drops for events over a large range of magnitudes, and those with M_W of about 2.5 to 4.0 have stress drops ranging from about 5 bars to 1000 bars. Aftershocks of the Loma Prieta earthquake with $M_L \approx$ 1.5-4.5 are found to have stress drops of 1-800 bars [*Guo et al.*, 1997] or, similarly, 6-266 bars [*Hough et al.*, 1991]. Events of M_L 2.8-4.2 in Round Valley are found to have $\Delta\sigma$=10-200 [*Smith and Priestley*, 1993]; M_L 1.8-4.5 events in the vicinity of Bordertown, Nevada, $\Delta\sigma \approx$ 60 bars [*Ichinose et al.*, 1997]; and M_L 1.8-4.5 events near Oroville, California, $\Delta\sigma$=14-170 bar [*Fletcher et al.*, 1984].

It is currently unclear whether these variations in stress drop estimates reflect true orders of magnitude spatial and temporal variability in typical earthquake stress

drop, or are artifacts of varying data quality or differences in methodology. Increased use of high-quality data from borehole seismometers [*Abercrombie and Leary*, 1993] and comparison of various time- and frequency-domain techniques are necessary to resolve this question.

4.4.2 Stress Drop Variations with Magnitude

I observe an increase in static stress drop with magnitude for M_L 2.5 to 4.0 Northridge aftershocks. The same trend has also been reported for M >4 Northridge aftershocks [*Mori et al.*, 1996]. Other studies, however, have determined that static stress drop does not vary with magnitude over large ranges of magnitude [*Abercrombie and Leary*, 1993; *Abercrombie*, 1995]. There are several proposed explanations for an observed trend in stress drop with magnitude. *Mori et al.* [1996] suggest that it indicates that more energetic earthquakes tend to grow to be larger magnitude events. It has also been suggested that there is a minimum nucleation size of earthquakes, causing small-magnitude events to have low stress drops since they cannot rupture a smaller area. The observations of *Archuleta et al.* [1982], that stress drop increases with magnitude only for M <3 events, is consistent with this model. This theory does not explain, however, why the trend of increasing stress drop with magnitude would continue for larger events, as it does for M >4 Northridge aftershocks [*Mori et al.*, 1996]. *Abercrombie and Leary* [1993] and *Abercrombie* [1995] suggest that the apparent lower stress drops and minimum source areas for small events are artifacts of attenuation of high frequency seismic waves. It could be that an increase in stress drop with magnitude is not universal, but occurs in some circumstances, such as the Northridge sequence, or it may be that the observations presented here have been affected by the attenuation of high frequencies.

4.4.3 Stress Drop Variations with Depth

The simple model summarized in Equation 4.2 predicts that stress drop should scale with effective normal stress. One would more realistically expect the maximum stress

drop to scale with effective normal stress. While fault heterogeneity could present barriers to slip which stop the rupture early, the total stress on the fault would provide an upper limit to stress drop.

An increase in maximum stress drop with depth is found for shallow events, $\leq$5 km depth, consistent with this model. However, for earthquakes deeper than 5 km, no correlation between maximum stress drop and depth was found. This indicates that one of the assumptions of Section 4.1 must not hold at depth. One possibility is that effective normal stress does not substantially increase with depth below $\sim$5 km due to elevated pore fluid pressure following a lithostatic gradient. This interpretation is consistent with the results of Chapter 2, which indicate that the deviatoric stress magnitude at depth is low. High pore pressure, and the resulting low effective normal stress, would lead to weak faults and low deviatoric stress.

Alternatively, the fault friction model may be incorrect and earthquake stress drop may not scale with the magnitude of the effective normal stress on the fault. A lack of scaling between stress drop and mainshock-induced stress change also suggests that stress drop is not strongly controlled by the magnitude of stress on the fault. This would be possible if the slip and stress drop were primarily controlled by the dynamic stress pulse or by a pulse of extreme fault weakening [*Heaton*, 1990; *Andrews and Ben-Zion*, 1997]. In this case, the slip and the stress drop would be controlled more by the duration and magnitude of the dynamic stress or fault weakening pulse than by the static effective normal stress on the fault. Dynamic faulting weakening is also consistent with the low deviatoric stress magnitudes observed in Chapter 2.

I observe higher average stress drops for deeper aftershocks due to an increase in minimum stress drop at 15 km depth. It appears that smaller stress drop events are inhibited at depth, which is unexpected. The lack of low stress-drop events may be due to a material property change. The Northridge aftershocks below about 15 km depth appear to occur within a high-seismic-velocity ridge [*Hauksson and Haase*, 1997], indicating that material properties may play an important role. One possible scenario is that only more energetic events are capable of growing to M >2.5 in stronger materials.

4.5 Conclusions

I have estimated static stress drop for 279 M_L 2.5 to 4.0 aftershocks of the 1994 Northridge earthquake using time-domain pulse widths. The stress drops are scattered over 3 orders of magnitude. Quantification of uncertainties indicates that the scatter is unlikely to be due solely to measurement errors, implying actual stress drop variations of at least 2 orders of magnitude.

The observed stress drops are larger for larger magnitude events. It has been proposed that such a trend could occur if there were a minimum size for earthquake rupture. However, it seems more likely that it is an artifact of the attenuation of high frequency seismic waves.

A roughly linear increase in maximum stress drop is observed between 0 and 5 km depth, consistent with a simple model of friction in which stress drop scales with effective normal stress. However, between 5 km and 15 km depth, where most events are located, there is no observed increase in stress drop with depth. Below 15 km, there is an observed increase in average stress due to a lack of low stress drop events at depth.

The lack of increasing stress drop with depth below 5 km implies that one of the assumptions of the simple friction model does not hold at depth. The lack of correlation between stress drop and effective normal stress could be explained if dynamic stress and dynamic fault weakening control the amount of slip on the fault. Alternatively, effective normal stress may not scale with depth if the increase in pore pressure with depth is approximately lithostatic.

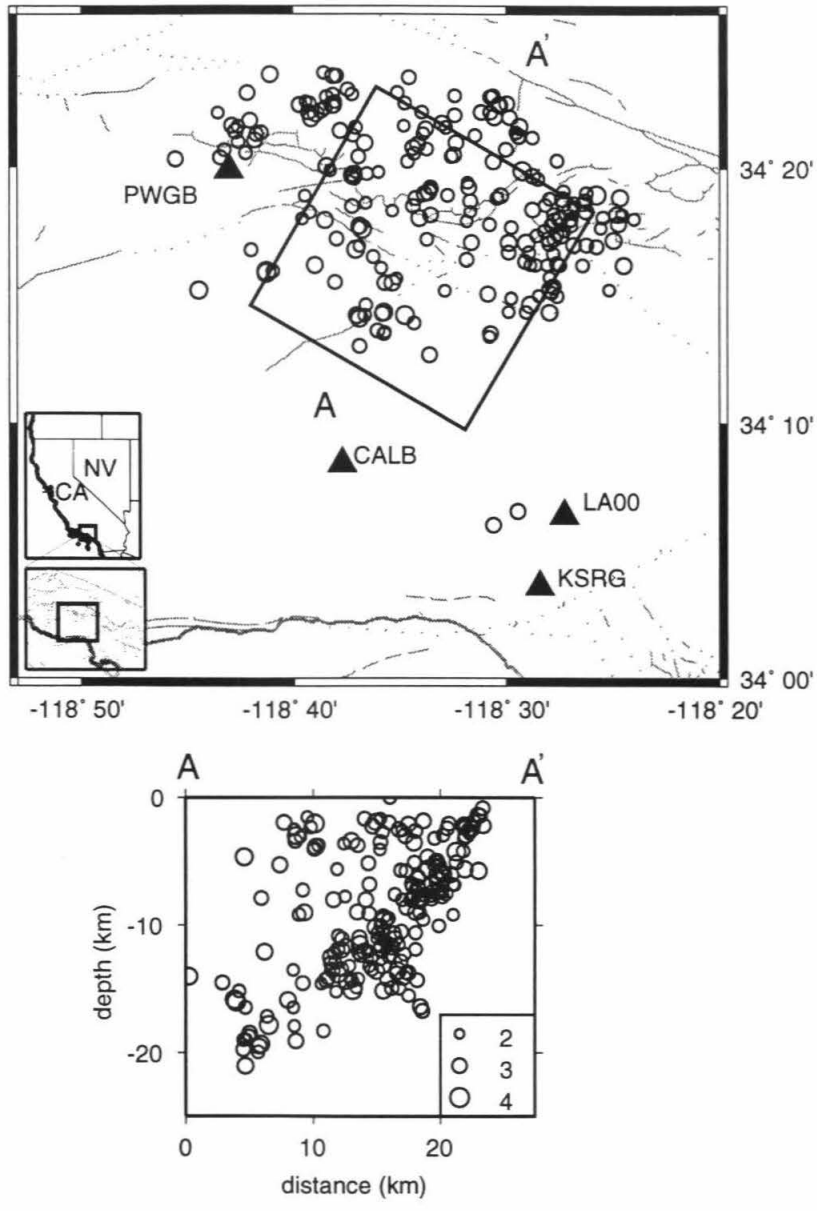

Figure 4.1: Northridge aftershocks, $M_L = 2.5$ to 4.0, used in this study, shown as open circles in map view and in northeast-southwest cross-section through the mainshock fault plane. Mainshock fault plane, shown as a black rectangle, from *Wald et al.* [1996]. The stations used in this study are shown as solid triangles.

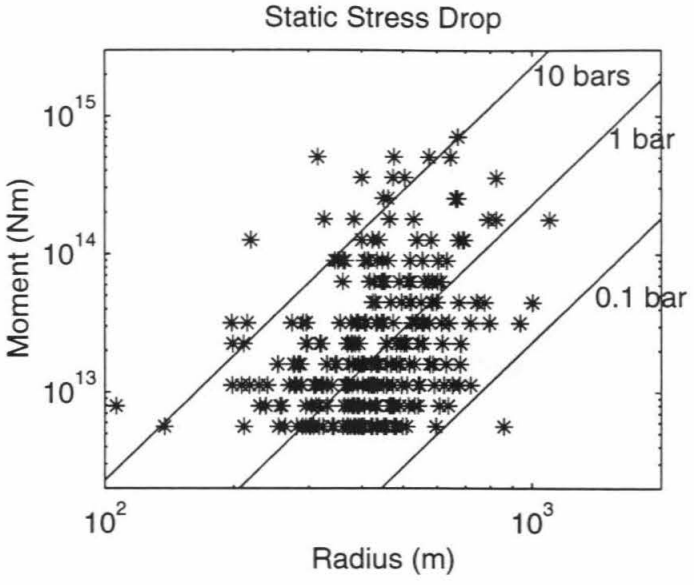

Figure 4.2: The combined (all stations) static stress drop estimates for the Northridge aftershocks, shown on a plot of seismic moment versus rupture radii. The solid diagonal lines are contours of constant static stress drop.

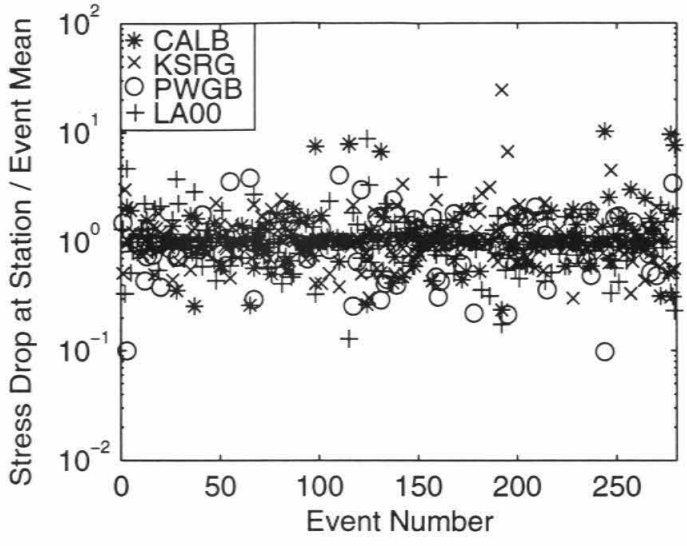

Figure 4.3: The ratio of static stress drop as observed at a station to the combined static stress drop estimate for each event. The observations from different stations are shown with different symbols.

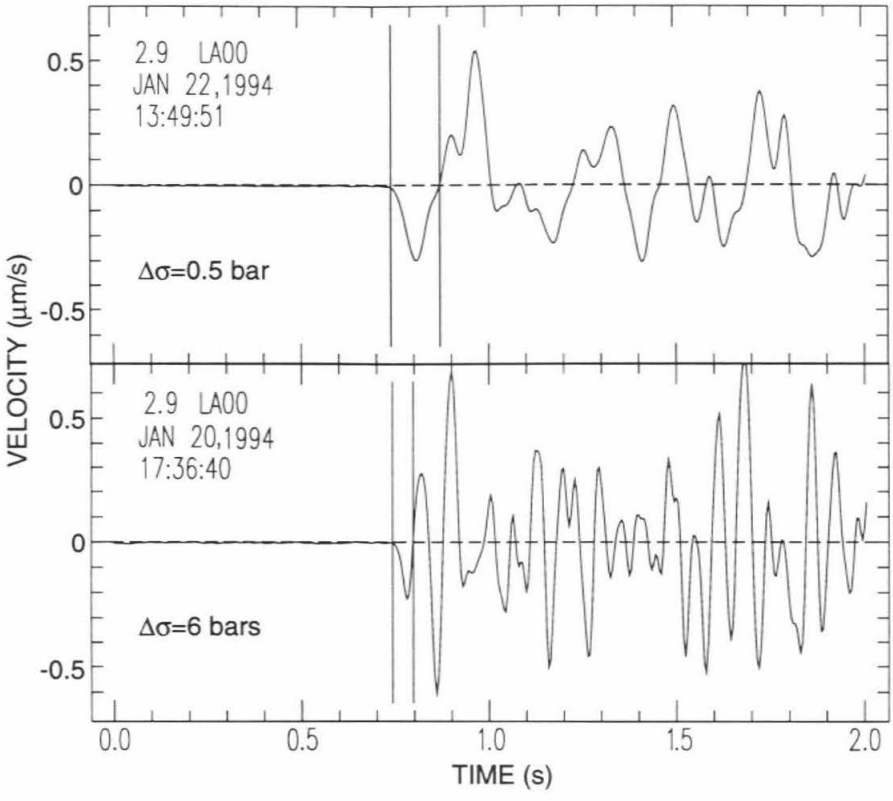

Figure 4.4: Velocity records of the direct P-waves, recorded at the station LA00, of two events with the same magnitude and epicentral distance (M_L =2.9, distance=24 km.) The event in the top record has a longer corrected P-wave pulse, about 0.15 s, and a calculated static stress drop of about 0.9 bar, while the event in the lower record has a shorter pulse, about 0.05 s, and a stress drop of about 10 bars.

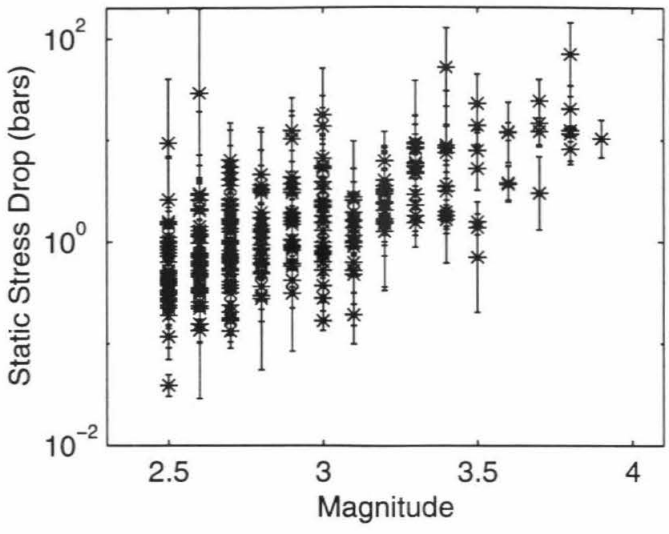

Figure 4.5: Combined estimates of static stress drop versus magnitude, with 95% confidence intervals shown as vertical error bars.

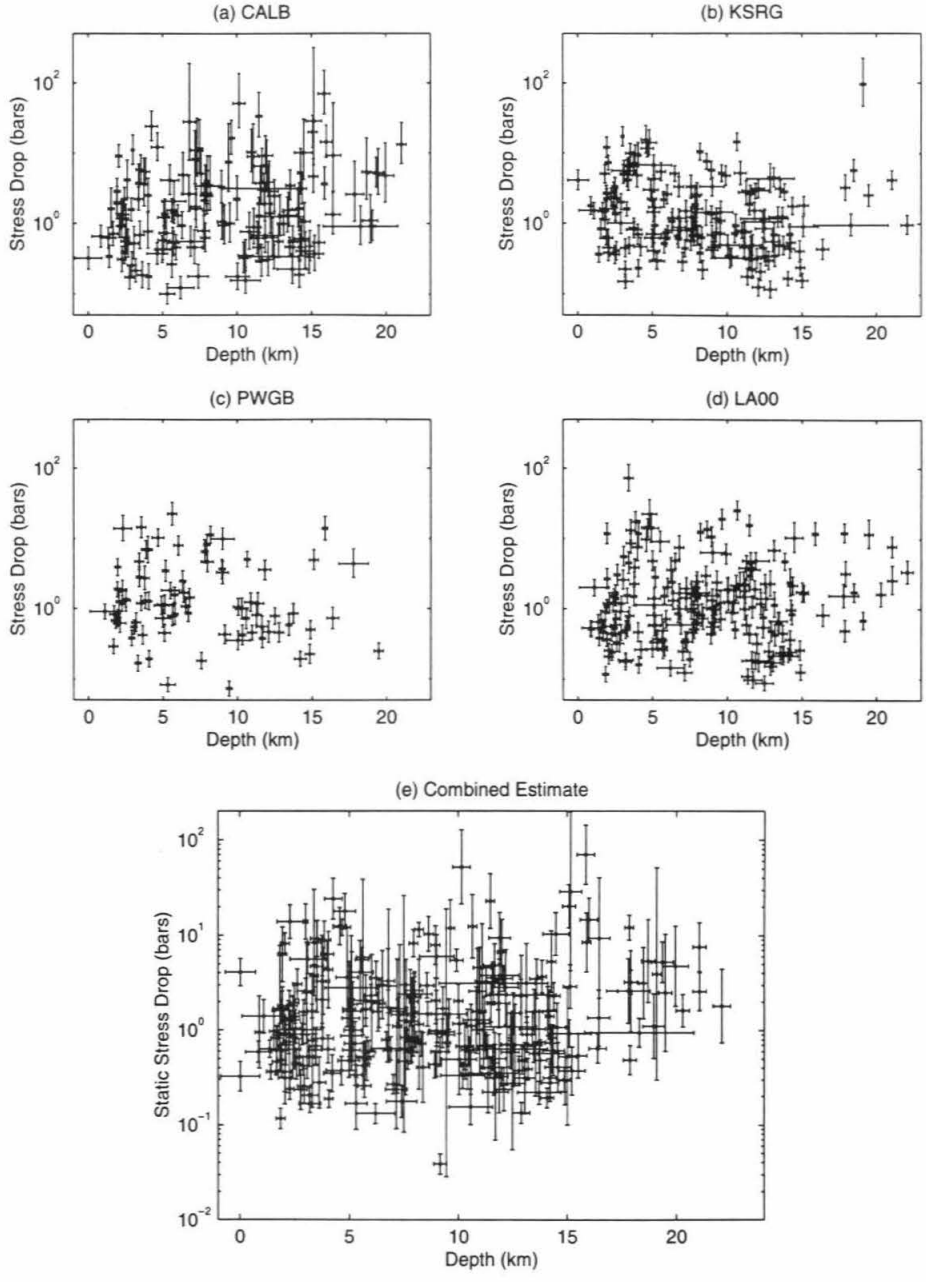

Figure 4.6: Static stress drop versus depth. The vertical error bars indicate the 95% confidence interval of the static stress drop, while the horizontal error bars indicate the 95% confidence level of the hypocentral depth. (a)-(d) Observations at individual stations. (e) Combined estimate (average over all stations).

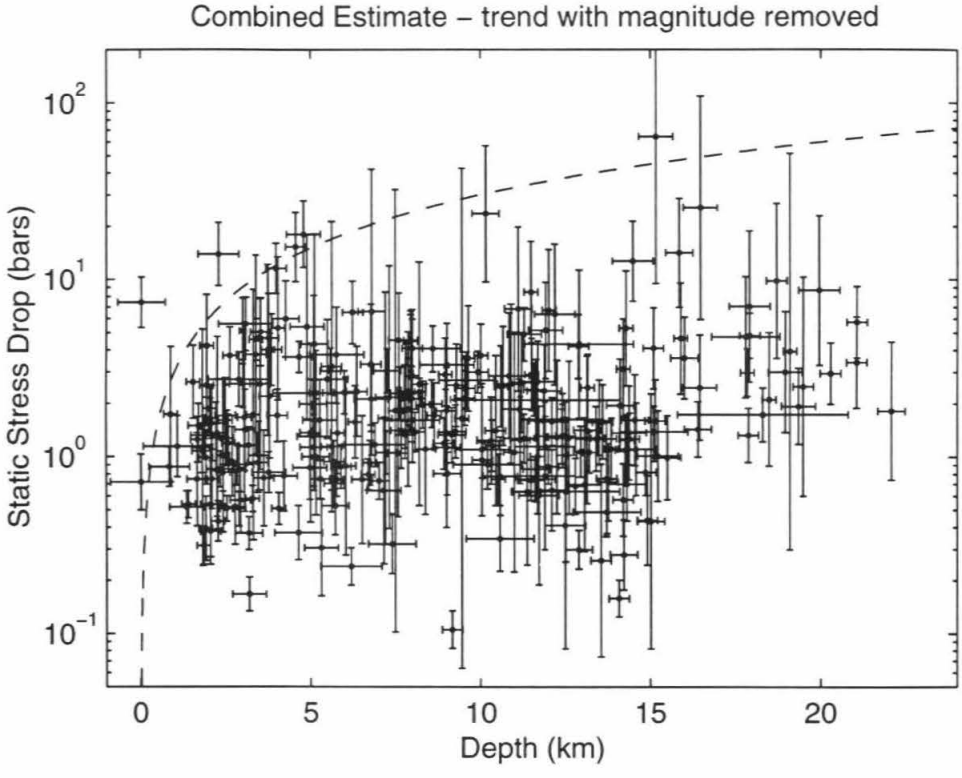

Figure 4.7: Static stress drop versus depth, after the trend in stress drop with magnitude (Figure 4.5) is removed. The vertical error bars indicate the 95% confidence interval of the static stress drop, while the horizontal error bars indicate the 95% confidence level of the hypocentral depth. The dashed line indicates a linear increase with depth equivalent to $\sim$1% of the lithostatic load.

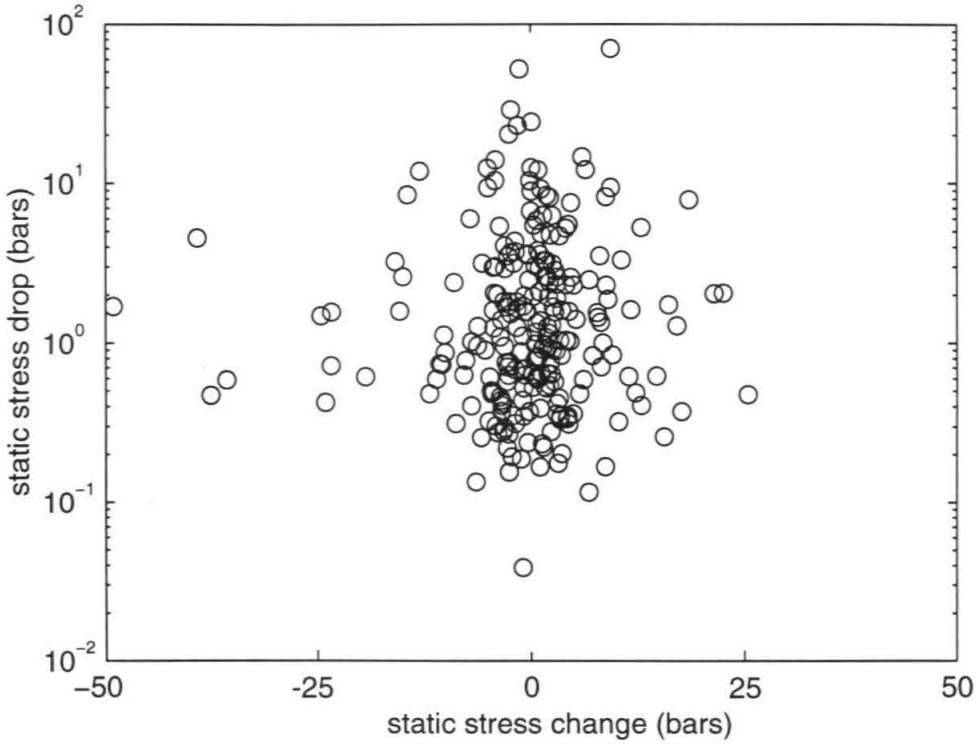

Figure 4.8: The estimated static stress drop plotted against the computed static stress change due to the Northridge mainshock. The static stress change shown is the change in shear stress in the direction of slip. Only events with known focal mechanisms are used.

P Wave Velocity (km/s)	Depth to Top of Layer (km)
3.5	0
4.5	1
5.0	2
5.5	6
6.0	8
6.5	12
6.6	16
6.72	18

Table 4.1: One-dimensional P-wave velocity model used in estimating the rupture velocity of each aftershock.

CUSP	Origin time (GMT)		Epicenter		Depth		$\Delta\sigma$ (bar)		
ID	yymmdd	time	lat	lon	(km)	M_L	$\Delta\sigma$	min	max
3141380	940118	08:45:10.1	34.276	-118.473	9.58	2.7	1.48	1.03	2.14
3141384	940118	09:00:48.3	34.367	-118.640	10.20	2.5	0.33	0.24	0.46
3141387	940118	09:12:57.3	34.288	-118.412	3.78	3.0	0.82	0.63	1.06
3141390	940118	09:17:42.9	34.290	-118.400	2.90	2.5	1.01	0.71	1.43
3141391	940118	09:25:49.1	34.349	-118.624	0.03	2.7	4.08	2.93	5.67
3142358	940119	21:04:14.9	34.374	-118.635	12.40	2.8	1.09	0.78	1.53
3186871	940119	21:04:23.7	34.350	-118.640	15.10	2.8	0.93	0.67	1.30
3142362	940119	21:17:59.2	34.357	-118.712	12.50	3.0	0.64	0.26	1.59
3142363	940119	21:22:02.2	34.350	-118.710	18.30	2.7	0.95	0.67	1.35
3142364	940119	21:26:15.0	34.360	-118.710	12.90	2.7	2.37	0.91	6.18
3142379	940119	21:42:03.5	34.284	-118.498	10.15	3.4	52.17	21.47	126.78
3142418	940119	22:59:06.4	34.364	-118.701	11.62	3.2	3.14	1.86	5.28
3142386	940119	22:06:36.3	34.381	-118.621	10.57	2.6	0.16	0.10	0.24
3142819	940120	05:58:24.6	34.379	-118.698	11.90	3.6	3.80	2.57	5.63
3142827	940120	09:57:32.7	34.355	-118.565	6.20	2.7	0.13	0.10	0.17
3142733	940120	10:07:09.0	34.273	-118.531	11.10	2.8	4.58	1.58	13.26
3142763	940120	11:27:35.9	34.381	-118.636	13.72	2.6	0.22	0.17	0.29
3142831	940120	11:36:16.3	34.379	-118.641	5.70	2.7	0.52	0.39	0.68
3142757	940120	11:06:19.7	34.374	-118.506	1.36	3.1	0.63	0.51	0.78
3142838	940120	12:26:22.6	34.305	-118.437	7.23	3.2	1.58	1.19	2.08
3142824	940120	13:56:45.5	34.361	-118.715	8.00	3.2	2.40	1.38	4.16
3142843	940120	14:22:50.9	34.290	-118.460	5.77	2.7	2.05	1.10	3.83
3142911	940120	17:36:40.5	34.217	-118.615	14.48	2.9	10.38	6.17	17.46
3142936	940120	18:43:15.4	34.337	-118.577	0.02	2.6	0.32	0.22	0.46
3142940	940120	18:48:07.0	34.369	-118.519	2.35	3.2	1.27	1.01	1.61
3142941	940120	18:56:01.2	34.312	-118.438	7.50	2.9	1.49	0.08	26.36
3142981	940120	20:45:29.0	34.286	-118.562	10.83	2.6	1.29	0.57	2.90
3143002	940120	21:24:24.0	34.381	-118.621	11.89	2.6	0.35	0.13	0.92
3143020	940120	22:04:44.4	34.254	-118.465	11.48	3.5	22.97	11.86	44.47
3143099	940121	02:51:47.2	34.270	-118.458	10.44	2.6	0.63	0.24	1.67
3143180	940121	05:49:56.7	34.289	-118.581	5.29	2.6	0.34	0.26	0.43
3143444	940121	07:53:54.2	34.357	-118.521	3.46	2.8	0.62	0.42	0.92
3143089	940121	02:04:43.7	34.380	-118.510	0.85	2.8	0.59	0.46	0.76
3143122	940121	03:35:47.8	34.322	-118.506	2.84	3.0	0.91	0.69	1.19
3143175	940121	05:29:20.4	34.348	-118.569	13.71	3.0	0.76	0.36	1.60
3143181	940121	05:56:04.6	34.270	-118.650	12.10	3.4	3.53	2.58	4.82
3143446	940121	08:40:17.1	34.356	-118.692	13.40	2.9	1.04	0.68	1.58
3143496	940121	10:43:59.7	34.379	-118.624	11.59	2.7	0.50	0.37	0.67
3143498	940121	11:14:48.3	34.280	-118.530	11.20	2.6	1.18	0.62	2.25

Table 4.2: The Northridge aftershocks used in this study, including the date, time, epicenter and depth of occurrence, the CUSP ID number used by the SCSN to catalog earthquakes, and the stress drop estimate with 95% confidence interval.

CUSP	Origin time (GMT)		Epicenter		Depth		$\Delta\sigma$ (bar)		
ID	yymmdd	time	lat	lon	(km)	M_L	$\Delta\sigma$	min	max
3143325	940121	11:31:17.0	34.368	-118.617	12.89	2.6	0.13	0.10	0.17
3143502	940121	12:43:53.8	34.371	-118.487	2.06	2.9	0.31	0.22	0.43
3143509	940121	12:47:06.7	34.370	-118.660	12.60	2.7	0.70	0.26	1.90
3143362	940121	13:22:15.0	34.276	-118.593	17.92	2.8	3.24	2.42	4.34
3143420	940121	16:31:24.9	34.394	-118.671	11.71	2.5	0.22	0.07	0.71
3143439	940121	17:32:26.0	34.303	-118.445	8.92	2.5	0.44	0.31	0.61
3145631	940121	18:42:24.4	34.310	-118.470	5.10	3.1	2.79	0.79	9.88
3183923	940121	18:42:24.4	34.320	-118.460	3.10	3.0	5.60	3.95	7.95
3143556	940121	18:57:19.2	34.291	-118.471	8.96	3.5	7.90	4.95	12.61
3143486	940121	19:11:36.6	34.290	-118.451	7.95	2.5	0.78	0.53	1.13
3143487	940121	19:14:20.8	34.334	-118.641	14.38	3.3	2.30	1.65	3.22
3143493	940121	19:27:37.9	34.296	-118.465	8.00	2.7	1.57	0.67	3.70
3143495	940121	19:37:42.1	34.292	-118.470	8.00	2.7	2.23	1.53	3.26
3143526	940121	19:46:37.9	34.303	-118.463	9.00	2.7	1.00	0.68	1.47
3143528	940121	19:54:40.0	34.309	-118.469	9.53	2.6	0.96	0.68	1.38
3143531	940121	19:56:56.1	34.287	-118.467	11.50	2.8	1.95	1.22	3.11
3143539	940121	20:12:16.6	34.299	-118.450	7.62	2.7	1.25	0.89	1.76
3143559	940121	20:57:51.4	34.296	-118.449	7.95	2.6	2.01	1.36	2.97
3143561	940121	21:02:54.6	34.330	-118.630	4.80	3.0	17.98	11.65	27.73
3143567	940121	21:26:27.5	34.286	-118.416	5.59	3.3	5.53	4.11	7.45
3143593	940121	22:22:51.6	34.395	-118.643	6.90	2.7	0.64	0.48	0.85
3143636	940122	00:16:35.9	34.353	-118.479	2.78	2.6	0.23	0.14	0.38
3143658	940122	01:49:37.7	34.304	-118.654	7.26	2.7	1.68	1.26	2.22
3143669	940122	02:18:59.0	34.225	-118.512	19.10	3.0	3.94	0.30	51.74
3143729	940122	03:27:34.0	34.338	-118.460	4.22	2.6	0.35	0.22	0.55
3143686	940122	03:34:10.3	34.350	-118.489	1.89	3.1	1.61	1.23	2.10
3143699	940122	03:55:37.4	34.317	-118.437	6.80	2.6	2.94	0.46	18.94
3143740	940122	05:41:54.7	34.251	-118.514	14.28	3.0	5.31	2.53	11.15
3143816	940122	09:03:49.6	34.362	-118.550	5.00	3.1	1.67	0.52	5.32
3143823	940122	09:45:46.2	34.271	-118.460	9.29	2.8	1.70	1.00	2.89
3143876	940122	12:46:29.8	34.292	-118.454	7.02	2.5	0.27	0.21	0.34
3143893	940122	13:49:51.8	34.313	-118.513	1.82	2.9	0.88	0.66	1.17
3143912	940122	14:43:09.8	34.382	-118.585	10.04	2.6	0.49	0.21	1.17
3143932	940122	15:17:01.9	34.330	-118.600	12.10	2.5	0.24	0.14	0.40
3143946	940122	15:41:11.6	34.380	-118.540	3.19	2.7	0.20	0.16	0.25
3144125	940122	23:14:54.6	34.314	-118.411	5.63	3.3	5.87	0.89	38.65
3144137	940122	23:36:23.8	34.256	-118.463	12.01	3.0	6.70	3.04	14.75
3144154	940123	00:30:45.7	34.315	-118.658	4.03	2.5	0.63	0.45	0.89
3144206	940123	02:48:46.6	34.337	-118.510	6.78	3.0	3.31	1.52	7.24
3144221	940123	04:00:55.3	34.300	-118.463	6.70	3.0	0.79	0.65	0.97
3144232	940123	04:58:10.6	34.289	-118.529	8.38	2.5	0.41	0.17	0.95
3144273	940123	06:57:41.2	34.382	-118.703	7.98	3.1	2.62	1.74	3.94

Table 4.2 cont.

CUSP	Origin time (GMT)		Epicenter		Depth		$\Delta\sigma$ (bar)		
ID	yymmdd	time	lat	lon	(km)	M_L	$\Delta\sigma$	min	max
3144530	940123	08:39:45.1	34.367	-118.540	2.06	2.8	0.36	0.17	0.79
3144291	940123	08:04:26.4	34.301	-118.458	8.20	2.6	1.16	0.24	5.60
3144539	940123	08:41:41.8	34.287	-118.465	8.20	3.8	11.54	9.69	13.74
3144306	940123	09:14:50.7	34.275	-118.604	9.15	2.6	0.59	0.41	0.85
3144556	940123	09:30:41.2	34.352	-118.522	5.11	2.8	0.87	0.65	1.16
2142200	940123	14:30:07.5	34.341	-118.628	10.30	2.7	0.68	0.38	1.20
3144428	940123	14:05:31.6	34.320	-118.529	2.50	3.1	1.96	1.24	3.12
3144459	940123	14:52:37.4	34.284	-118.527	8.97	3.2	2.05	1.17	3.59
3144558	940123	14:52:57.3	34.394	-118.685	11.68	3.3	4.85	2.88	8.18
3144561	940123	15:59:03.8	34.258	-118.595	1.95	3.2	6.30	3.25	12.23
3145080	940123	22:05:02.2	34.140	-116.870	8.60	2.5	1.49	1.11	2.01
3145082	940123	22:05:26.1	34.290	-118.490	8.30	2.5	0.72	0.53	0.98
3145050	940123	23:37:23.0	34.296	-118.433	9.27	2.8	0.93	0.66	1.32
3145129	940124	02:41:02.5	34.244	-118.481	13.85	3.6	3.69	2.48	5.50
3145173	940124	03:42:46.3	34.308	-118.573	3.75	2.9	3.28	1.08	9.97
3187574	940124	05:11:27.3	34.270	-118.540	17.80	2.7	2.61	1.19	5.71
3145158	940124	05:22:29.4	34.303	-118.409	9.17	2.5	0.04	0.03	0.05
3145172	940124	05:59:22.5	34.354	-118.620	11.13	2.7	1.02	0.69	1.51
3145176	940124	06:13:10.1	34.359	-118.618	11.48	2.7	0.41	0.31	0.53
3145184	940124	06:27:38.9	34.278	-118.482	10.59	2.6	1.12	0.67	1.89
3145185	940124	06:33:44.9	34.326	-118.475	5.32	2.7	0.17	0.09	0.32
3145187	940124	07:04:37.2	34.294	-118.496	9.45	2.6	0.74	0.03	19.13
3145284	940124	10:48:27.7	34.346	-118.573	14.08	2.6	0.19	0.15	0.25
3174345	940124	10:48:48.7	34.346	-118.573	15.02	3.1	0.53	0.10	2.79
3145302	940124	13:47:12.4	34.380	-116.460	2.30	3.0	13.91	9.22	21.01
3145393	940124	17:52:51.2	34.369	-118.655	12.53	3.2	1.52	0.93	2.50
3145401	940124	18:16:29.4	34.358	-118.563	1.83	3.2	1.69	0.36	7.83
3145396	940124	18:05:59.8	34.368	-118.649	13.13	3.4	3.16	1.21	8.24
3145456	940124	21:31:44.5	34.282	-118.429	2.63	2.9	3.05	2.11	4.42
3145547	940125	02:06:35.9	34.300	-118.449	7.60	2.8	3.04	1.65	5.59
3145652	940125	03:09:31.3	34.345	-118.500	2.43	2.9	0.83	0.31	2.26
3145735	940125	08:40:22.7	34.359	-118.547	3.19	2.6	0.52	0.41	0.66
3145736	940125	08:41:13.8	34.310	-118.447	7.20	2.8	1.10	0.22	5.64
3145747	940125	10:21:57.9	34.302	-118.559	10.98	3.2	1.58	0.33	7.53
3145743	940125	12:09:00.2	34.315	-118.504	1.09	3.1	1.40	0.94	2.09
3179723	940125	12:08:59.8	34.315	-118.504	2.10	3.1	0.92	0.62	1.35
3145830	940125	16:21:25.1	34.254	-118.419	9.54	2.5	0.90	0.59	1.36
3146011	940125	17:17:29.6	34.313	-118.511	2.54	3.5	1.39	1.17	1.64
3145846	940125	18:08:42.5	34.313	-118.511	0.89	2.7	0.95	0.40	2.29
3145851	940125	18:42:43.8	34.314	-118.447	9.92	3.3	5.47	4.18	7.17
3145922	940125	22:23:23.6	34.370	-118.720	9.00	2.9	0.92	0.33	2.62
3145977	940126	02:17:29.5	34.284	-118.645	22.07	3.0	1.81	0.74	4.44

Table 4.2 cont.

CUSP	Origin time (GMT)		Epicenter		Depth		$\Delta\sigma$ (bar)		
ID	yymmdd	time	lat	lon	(km)	M_L	$\Delta\sigma$	min	max
3146002	940126	03:43:09.4	34.187	-118.540	12.88	2.7	2.30	1.52	3.48
3146006	940126	03:53:59.2	34.374	-118.663	11.28	2.8	3.29	2.32	4.66
3146008	940126	04:04:04.0	34.248	-118.472	14.32	2.8	0.84	0.60	1.16
3146038	940126	05:38:28.3	34.276	-118.508	11.67	2.6	0.45	0.21	0.95
3146073	940126	07:58:51.5	34.276	-118.496	10.33	2.5	0.43	0.31	0.59
3146164	940126	08:46:15.5	34.180	-118.617	5.12	2.5	1.58	0.37	6.66
3146189	940126	11:50:40.5	34.330	-118.440	5.80	2.5	0.50	0.29	0.85
3146149	940126	12:28:47.0	34.295	-118.478	10.66	3.8	12.43	5.75	26.87
3146168	940126	13:53:23.3	34.185	-118.616	4.57	2.9	12.49	7.94	19.65
3146267	940126	16:07:03.3	34.370	-118.634	12.49	2.8	0.28	0.06	1.38
3146268	940126	16:20:31.0	34.240	-118.600	2.10	2.6	0.70	0.42	1.14
3146233	940126	17:09:22.8	34.370	-118.526	3.30	3.5	1.58	1.33	1.87
3146270	940126	17:38:47.4	34.348	-118.610	13.06	2.6	0.31	0.13	0.75
3146242	940126	17:59:41.2	34.213	-118.612	3.20	3.0	0.17	0.13	0.21
3146419	940127	04:04:22.7	34.277	-118.463	12.41	2.6	0.59	0.39	0.89
3146427	940127	04:43:52.4	34.360	-118.489	2.43	3.4	1.81	1.42	2.31
3146437	940127	05:50:08.6	34.343	-118.704	3.77	2.6	2.09	1.17	3.74
3146452	940127	06:26:22.1	34.252	-118.464	14.20	2.6	1.41	0.74	2.69
3146522	940127	12:10:53.7	34.313	-118.466	7.67	2.6	0.63	0.39	1.03
3146550	940127	13:49:05.1	34.353	-118.490	2.26	2.7	0.75	0.21	2.61
3146657	940127	14:31:10.5	34.258	-118.589	15.89	3.3	8.49	4.15	17.37
3146638	940127	17:56:33.8	34.184	-118.614	6.24	2.7	3.56	2.37	5.36
3146681	940127	20:41:11.9	34.356	-118.557	5.16	3.0	1.00	0.47	2.13
3146789	940128	04:58:33.8	34.300	-118.458	7.95	3.3	8.24	5.93	11.46
3146791	940128	05:47:51.6	34.357	-118.630	11.84	3.2	2.39	1.64	3.48
3146815	940128	07:44:46.2	34.237	-118.617	21.05	3.4	7.56	4.19	13.66
3146864	940128	12:34:36.2	34.370	-118.498	1.71	2.7	0.82	0.62	1.10
3146868	940128	12:48:41.8	34.366	-118.497	1.92	3.1	0.48	0.32	0.73
3147037	940128	23:04:54.5	34.356	-118.492	2.28	2.7	0.24	0.18	0.31
3147057	940129	00:47:17.6	34.287	-118.462	10.52	2.9	0.61	0.44	0.85
3147167	940129	07:52:21.3	34.238	-118.623	21.06	2.6	2.58	1.62	4.09
3147235	940129	10:42:27.2	34.307	-118.474	11.16	2.7	0.68	0.39	1.21
3147539	940129	11:13:18.0	34.303	-118.413	6.04	3.4	1.97	0.62	6.28
3147243	940129	11:30:00.4	34.315	-118.546	2.70	2.7	0.52	0.33	0.82
2176175	940129	11:37:30.1	34.300	-118.660	2.50	2.5	0.63	0.38	1.03
3147246	940129	11:37:31.6	34.299	-118.642	9.01	3.3	6.01	3.53	10.23
3147263	940129	12:21:11.0	34.292	-118.607	3.06	3.2	2.49	0.73	8.45
3147457	940129	12:35:33.5	34.313	-118.571	1.67	2.9	0.61	0.33	1.12
3147272	940129	12:47:36.0	34.349	-118.611	15.14	3.3	2.92	1.71	4.97
3147277	940129	12:59:43.3	34.316	-118.564	2.25	3.1	1.03	0.56	1.87
3147283	940129	13:15:48.9	34.287	-118.633	3.40	2.9	3.75	2.86	4.92
3147344	940129	14:03:06.7	34.300	-118.568	3.40	3.4	8.39	2.30	30.60

Table 4.2 cont.

CUSP	Origin time (GMT)		Epicenter		Depth		$\Delta\sigma$ (bar)		
ID	yymmdd	time	lat	lon	(km)	M_L	$\Delta\sigma$	min	max
3147332	940129	15:10:52.4	34.305	-118.589	3.63	2.5	0.28	0.15	0.52
3147357	940129	16:19:09.7	34.188	-118.616	4.90	2.8	3.62	1.09	12.02
3147370	940129	17:22:52.6	34.302	-118.566	3.32	2.6	0.78	0.15	3.94
3147390	940129	18:20:43.5	34.303	-118.637	3.99	2.7	6.32	4.55	8.78
3147394	940129	18:54:46.8	34.393	-118.635	16.40	2.6	0.65	0.45	0.93
3147399	940129	19:25:44.4	34.375	-118.654	11.37	2.7	0.35	0.13	0.90
3147418	940129	20:48:48.1	34.376	-118.657	11.65	2.5	0.31	0.20	0.48
3147443	940129	21:45:14.0	34.306	-118.479	7.80	3.0	2.21	1.12	4.38
3147518	940129	21:08:43.7	34.282	-118.615	3.08	2.5	0.52	0.31	0.89
3147511	940130	00:12:28.4	34.270	-118.477	13.46	2.6	0.57	0.46	0.72
3147524	940130	00:50:16.5	34.270	-118.481	13.20	2.5	0.39	0.30	0.51
3147583	940130	03:03:44.5	34.323	-118.530	2.59	2.5	0.44	0.30	0.64
3147604	940130	04:59:39.8	34.250	-118.474	13.15	2.5	0.90	0.59	1.39
3147629	940130	06:35:35.9	34.369	-118.566	4.99	2.7	0.48	0.32	0.72
3147650	940130	08:19:05.8	34.278	-118.498	5.17	2.9	1.88	1.09	3.25
3147655	940130	09:19:56.1	34.317	-118.561	1.93	3.3	1.80	1.27	2.56
3147663	940130	09:56:01.6	34.319	-118.558	4.07	2.5	0.19	0.15	0.23
3147842	940130	10:44:40.2	34.379	-118.566	3.53	3.3	4.70	1.55	14.25
3147712	940130	13:22:39.9	34.340	-118.543	5.10	2.7	0.62	0.38	1.03
3147773	940130	17:01:42.5	34.310	-118.440	5.90	2.8	0.59	0.44	0.78
3147908	940130	23:22:21.9	34.330	-118.618	14.86	2.5	0.30	0.22	0.41
3148013	940131	04:27:46.8	34.370	-118.515	1.86	2.5	0.12	0.09	0.15
3148020	940131	04:55:50.0	34.295	-118.615	3.86	3.4	8.92	5.62	14.16
3148026	940131	05:20:15.6	34.294	-118.616	4.05	2.9	4.35	1.72	11.00
3148120	940131	11:41:15.3	34.283	-118.437	6.75	2.8	0.62	0.46	0.83
3148420	940131	17:38:14.5	34.326	-118.619	14.20	2.7	0.31	0.20	0.50
3148401	940201	06:08:19.8	34.238	-118.597	19.49	3.0	2.49	0.60	10.34
3148411	940201	07:40:19.8	34.235	-118.615	4.67	3.6	12.10	9.90	14.78
3148450	940201	09:59:10.6	34.336	-118.688	3.80	3.2	3.29	1.46	7.38
3148482	940201	12:51:58.7	34.313	-118.507	12.24	2.7	0.71	0.26	1.91
3148529	940201	18:23:36.0	34.340	-118.616	6.79	2.9	1.74	1.13	2.66
3148553	940201	21:15:22.2	34.254	-118.620	8.08	2.7	0.76	0.59	0.98
3148691	940202	07:30:17.3	34.318	-118.455	7.79	2.6	0.59	0.44	0.81
3148720	940202	11:24:37.5	34.293	-118.613	2.06	3.8	8.16	6.25	10.64
3148722	940202	11:51:53.8	34.379	-118.512	1.41	2.8	0.36	0.30	0.43
3148756	940202	15:55:17.1	34.392	-118.576	5.08	2.8	1.33	0.97	1.83
3148988	940203	08:21:21.6	34.305	-118.438	6.37	2.9	1.91	1.07	3.42
3149105	940203	16:23:35.4	34.298	-118.440	8.64	3.9	10.34	6.76	15.81
3149297	940204	04:49:45.8	34.297	-118.412	6.00	3.0	2.31	1.74	3.06
3149315	940204	06:33:39.2	34.280	-118.618	3.01	3.5	13.94	9.08	21.40
3149474	940204	14:26:05.7	34.270	-118.408	3.54	3.3	9.22	5.94	14.32
3149484	940204	16:25:39.8	34.310	-118.610	5.63	2.5	0.42	0.24	0.74

Table 4.2 cont.

CUSP	Origin time (GMT)		Epicenter		Depth		$\Delta\sigma$ (bar)		
ID	yymmdd	time	lat	lon	(km)	M_L	$\Delta\sigma$	min	max
3149534	940204	20:15:51.6	34.306	-118.450	7.87	3.0	2.33	1.52	3.58
3149674	940205	07:11:45.2	34.240	-118.613	17.88	2.5	0.49	0.34	0.69
3149890	940205	08:17:18.8	34.376	-118.634	12.79	2.7	0.37	0.26	0.54
3149688	940205	08:51:06.5	34.374	-118.636	13.55	3.5	0.71	0.20	2.48
3149689	940205	08:58:34.7	34.372	-118.642	14.91	2.8	0.29	0.16	0.53
3149732	940205	09:53:44.0	34.373	-118.636	13.76	2.8	0.48	0.29	0.80
3149757	940205	11:19:46.3	34.311	-118.528	1.95	2.8	1.70	1.01	2.88
3149876	940205	19:54:59.5	34.304	-118.528	1.68	2.5	0.46	0.34	0.62
3149895	940205	21:18:41.0	34.109	-118.491	10.89	3.0	2.59	0.92	7.27
3150067	940206	10:00:20.9	34.374	-118.662	11.57	3.2	3.58	2.54	5.05
3150211	940206	13:21:45.5	34.284	-118.484	9.64	3.6	11.89	6.00	23.58
3150110	940206	14:19:54.4	34.289	-118.476	7.58	2.6	0.47	0.21	1.08
3150453	940207	22:52:30.3	34.331	-118.627	14.26	2.8	0.73	0.47	1.15
3150519	940208	06:30:06.8	34.296	-118.513	10.01	2.7	2.04	1.36	3.07
3150524	940208	07:06:54.9	34.343	-118.606	5.70	2.5	0.26	0.19	0.34
3150555	940208	11:16:05.5	34.341	-118.541	6.32	3.0	1.57	0.98	2.52
3150570	940208	14:23:55.4	34.360	-118.720	11.28	2.7	0.70	0.51	0.96
3150980	940210	07:43:06.8	34.366	-118.509	2.91	3.3	1.55	1.15	2.09
3150991	940210	09:47:51.2	34.331	-118.638	7.76	2.5	0.84	0.58	1.21
3151009	940210	11:16:12.3	34.374	-118.505	5.77	3.4	1.65	1.33	2.06
3151159	940211	00:53:36.8	34.369	-118.512	2.55	2.9	1.04	0.73	1.50
3151199	940211	06:41:13.6	34.310	-118.455	7.32	2.8	1.45	0.26	7.97
3151279	940211	14:23:10.2	34.360	-118.580	7.16	2.5	0.24	0.09	0.61
3151277	940211	14:07:52.8	34.331	-118.487	6.52	3.7	3.02	1.31	6.92
3151303	940211	15:52:49.2	34.402	-118.770	10.05	3.1	1.17	0.93	1.48
3151446	940212	06:58:48.6	34.329	-118.609	12.39	2.6	0.59	0.41	0.84
3151517	940212	15:10:30.2	34.319	-118.545	2.90	2.9	0.42	0.33	0.52
3151637	940213	00:43:18.7	34.196	-118.572	20.29	2.7	1.62	1.09	2.40
3151716	940213	19:43:06.9	34.253	-118.548	1.55	2.5	0.97	0.61	1.56
3152209	940214	20:32:57.3	34.211	-118.560	18.49	3.2	3.16	1.33	7.50
3152329	940215	00:22:22.7	34.259	-118.634	7.87	2.8	1.24	0.46	3.39
3152583	940215	02:53:23.2	34.262	-118.466	11.99	2.5	0.32	0.26	0.41
3152435	940215	09:42:48.2	34.370	-118.645	14.22	3.0	0.28	0.18	0.44
3152592	940215	12:31:55.1	34.289	-118.457	8.57	3.2	2.97	2.18	4.05
3152456	940215	13:51:49.0	34.242	-118.559	2.04	2.8	1.26	0.93	1.71
3152649	940216	07:58:42.2	34.100	-118.510	5.50	3.2	4.08	1.89	8.84
3152719	940216	18:00:38.2	34.283	-118.447	3.02	3.0	2.59	1.90	3.53
3153233	940218	09:13:28.1	34.237	-118.579	17.85	3.7	12.15	8.95	16.49
3153329	940218	15:44:23.1	34.299	-118.462	9.02	3.1	0.98	0.74	1.30
3153583	940219	02:54:08.0	34.239	-118.484	12.94	2.6	0.48	0.35	0.67
3155156	940225	13:56:13.6	34.316	-118.429	4.27	3.7	24.23	14.78	39.74
3155364	940226	13:03:51.2	34.340	-118.724	14.54	2.8	1.08	0.60	1.96

Table 4.2 cont.

CUSP	Origin time (GMT)		Epicenter		Depth		$\Delta\sigma$ (bar)		
ID	yymmdd	time	lat	lon	(km)	M_L	$\Delta\sigma$	min	max
3156198	940303	09:53:49.7	34.375	-118.499	2.22	3.0	1.31	0.84	2.04
3156974	940306	18:19:11.2	34.354	-118.524	2.94	2.6	0.26	0.17	0.39
3157314	940308	12:53:01.2	34.239	-118.466	11.91	3.3	9.42	5.06	17.53
3157439	940309	09:17:50.2	34.384	-118.624	14.31	2.9	0.57	0.36	0.92
3158234	940313	11:12:08.5	34.244	-118.610	19.96	2.7	4.76	1.81	12.54
3158492	940315	01:13:41.6	34.270	-118.440	10.58	2.6	0.35	0.21	0.58
3158543	940315	10:44:21.5	34.328	-118.479	5.73	3.0	0.53	0.36	0.77
3158836	940316	19:21:59.7	34.301	-118.424	7.40	2.7	0.18	0.12	0.26
3159080	940318	17:58:17.6	34.250	-118.460	12.18	2.6	2.85	1.15	7.11
3159301	940320	06:48:31.1	34.351	-118.697	13.49	3.0	1.57	0.91	2.72
3160313	940325	01:58:45.4	34.320	-118.559	3.48	2.8	0.68	0.43	1.07
3160535	940326	15:13:31.7	34.355	-118.696	11.87	2.9	1.94	1.07	3.50
3161512	940402	14:10:47.7	34.365	-118.653	13.59	3.4	3.51	2.17	5.69
3161587	940403	04:41:19.8	34.375	-118.579	5.28	2.6	0.72	0.43	1.22
3162063	940406	09:18:59.0	34.349	-118.539	4.65	3.0	0.37	0.26	0.53
3164591	940423	14:15:54.9	34.280	-118.700	16.45	2.7	1.35	0.68	2.67
3164710	940424	15:54:43.5	34.308	-118.621	14.11	2.9	1.60	0.88	2.92
3167759	940516	08:40:46.5	34.328	-118.620	15.09	3.8	20.30	12.01	34.30
3167761	940516	09:10:39.6	34.328	-118.621	14.37	2.6	0.61	0.33	1.13
3168049	940518	14:01:20.5	34.261	-118.586	16.47	2.5	9.38	2.19	40.17
3168156	940519	03:02:18.2	34.237	-118.611	18.71	2.7	5.40	1.98	14.74
3168612	940522	01:46:49.8	34.239	-118.498	14.58	2.5	0.41	0.22	0.74
3168758	940523	08:54:38.8	34.369	-118.726	15.22	2.5	0.37	0.21	0.67
3169789	940530	12:24:21.9	34.268	-118.598	17.91	2.5	2.60	0.98	6.94
3175511	940711	06:49:15.3	34.265	-118.688	15.85	3.8	70.07	34.53	142.21
3175686	940711	06:50:49.4	34.266	-118.688	16.00	3.7	14.63	8.64	24.77
3176380	940717	15:29:09.5	34.239	-118.596	19.35	3.5	5.26	3.21	8.62
3176769	940720	11:34:47.6	34.345	-118.562	15.50	2.7	0.54	0.31	0.94
3178350	940730	05:34:33.7	34.266	-118.683	15.16	2.6	28.95	4.26	196.59
3178640	940801	14:48:51.0	34.226	-118.595	18.96	2.5	1.11	0.51	2.42

Table 4.2 cont.

Chapter 5 Static Stress Change Triggering of Earthquakes

5.1 Introduction

Major earthquakes can have a significant effect on the stress field in the surrounding crust. Rotations of the principal stress axes due to the M_W7.3 Landers and M_W6.7 Northridge earthquakes were demonstrated in Chapter 1. It has been proposed that these earthquake-induced stress changes can play a role in triggering aftershock sequences and subsequent major events.

Numerous studies have focused on static stress change, particularly Coulomb stress change, as a possible triggering mechanism for aftershocks [*Reasenberg and Simpson*, 1992; *Beroza and Zoback*, 1993; *King et al.*, 1994; *Stein et al.*, 1994; *Kilb et al.*, 1997; *Toda et al.*, 1998; *Anderson and Johnson*, 1999]. The Coulomb stress triggering model is based on the idea that mainshock-induced static stress changes may move a candidate fault towards or away from the Coulomb failure envelope. The Coulomb stress change, ΔCS, on a fault plane is:

$$\Delta CS = \Delta\tau + \mu(\Delta\sigma + \Delta p) \tag{5.1}$$

where $\Delta\sigma$ is the normal stress change (tension positive), Δp is the pore pressure change, $\Delta\tau$ is the shear stress change in the direction of slip, and μ is the coefficient of static friction. Positive ΔCS means that the fault has been moved towards failure, negative ΔCS that it has been moved away from failure. Coulomb stress change is often written as:

$$\Delta CS = \Delta\tau + \mu'\Delta\sigma \tag{5.2}$$

where μ' is an effective coefficient of friction meant to incorporate the change in

fluid pressure. However, *Beeler et al.* [1998] demonstrated that this approximation is generally not correct.

Quantitative tests of the static stress change triggering model for aftershocks have given mixed results. *Reasenberg and Simpson* [1992] demonstrated a correlation between static stress changes and seismicity rate changes for the 1989 Loma Prieta, California, earthquake. However, *Beroza and Zoback* [1993] and *Kilb et al.* [1997] also studied the Loma Prieta sequence and concluded that the diverse aftershock mechanisms could not be adequately explained by static stress changes. A correlation between static stress change and seismicity rate change was again found for the 1995 Kobe, Japan, earthquake [*Toda et al.*, 1998], but *Anderson and Johnson* [1999] found that the aftershocks of the Superstition Hills, California, earthquake are no more consistent with triggering than the pre-mainshock seismicity. More work is clearly necessary in order to understand whether static stress changes trigger aftershocks.

In this chapter, the Coulomb stress change triggering model is quantitatively tested for the 1992 Landers and 1994 Northridge earthquake sequences [*Hauksson et al.*, 1993, 1995a]. Specifically, I test whether the number of aftershocks consistent with triggering is significantly greater than the number that would appear consistent simply by chance. I also investigate whether parameters such as aftershock magnitude, distance from the mainshock fault plane, magnitude of the static stress change, or time after the mainshock affect how well the model explains the observed aftershocks. *Hardebeck et al.* [1998] present a similar study. The work in this chapter is based on a larger and higher-quality data set. Pore pressure changes are also modeled more correctly, using Equation 5.1, while *Hardebeck et al.* [1998] used Equation 5.2.

5.2 Method

The percent of aftershocks consistent with Coulomb stress triggering, also called the Coulomb Index (CI), is computed for the first month of aftershocks of each sequence. This provides a simple quantitative measurement of the performance of the Coulomb stress triggering model. The CI of the observed sequence is also compared to the

distribution of CI values for a suite of random, synthetic sequences. If the CI of the observed sequence is large enough to be sufficiently unlikely to have come from the distribution for random sequences, the success of the model is considered statistically significant.

5.2.1 Observed Sequences

The aftershock data sets for Landers and Northridge comprise all events in the focal mechanism catalog, described in Chapter 1, that occurred within the first month following the mainshock, including events which are not strictly aftershocks. Stress change due to the mainshock at the location of each aftershock is calculated by modeling the mainshock slip as a dislocation in an elastic halfspace, using the program ELFPOINT by Robert W. Simpson, based on the subroutines of *Okada* [1992]. The thrust faulting M_W=6.7 Northridge mainshock is modeled using the slip distribution of *Wald et al.* [1996]; and the right-lateral M_W=7.3 Landers mainshock using the slip distribution of *Wald and Heaton* [1994]. Two other events of the Landers sequence, the M_W=6.1 Joshua Tree preshock and the M_W=6.2 Big Bear aftershock were modeled as square dislocations with 0.35 m slip and 12-15 km diameter.

The computed stress change tensor is resolved on to both nodal planes of each focal mechanism, and the Coulomb stress change is found using Equation 5.1. The change in pore pressure is found from the relationship [*Rice and Cleary*, 1976]:

$$\Delta p = -\beta \Delta \sigma_{kk}/3. \tag{5.3}$$

This equation assumes that the system is undrained. Since pore pressure diffusion is very slow, on a length scale of about 1 m over 5 years, the undrained assumption seems reasonable when studying the first few years of an aftershock sequence. I use the parameter values β=0.7, and μ=0.6 [*Byerlee*, 1978].

The CI is defined as the percent of events consistent with triggering. This includes all events which experienced a positive ΔCS on both nodal planes, and one-half of the events with a positive ΔCS on only one plane, since there is a 50% chance that the

nodal plane with positive ΔCS is the true nodal plane. Error bars for the CI are found using a bootstrap technique. The data set is resampled 100 times, with replacement, and the CI for the resampled sequences found. The mechanisms are also varied within their formal 1σ confidence regions. The fraction of events with only one positive ΔCS plane that is counted towards the CI is chosen from a binomial distribution for the data set size and an expected value of 0.5.

The CI is found for the entire data set, and also for subsets based on event magnitude, distance from the mainshock fault, magnitude of stress change, time, and, for the Northridge sequence, hypocentral depth. The magnitude of the stress change is defined as $\Delta\tau_{max}$, the maximum shear stress change on a plane of any orientation.

5.2.2 Synthetic Sequences

The choice of random synthetic sequences, which are to be compared with the observed sequences, is inevitably subjective. Many studies use synthetic sequences in which the locations of the earthquakes are the same as in the observed sequence, but the mechanisms are redistributed. However, these synthetic sequences don't sample regions where no aftershocks occurred, and a truly random sequence should be allowed to sample all of the relevant space. Other studies use pre-event seismicity as a comparison data set. However, the geometry of pre-event seismicity is usually very different from the geometry of the aftershock sequence, and these geometrical differences may map into differences in CI which are unrelated to triggering. Also, pre-event seismicity may be affected by processes leading up to the mainshock.

My solution is to create synthetic sequences with the basic geometry of an aftershock sequence (i.e., clustered around the mainshock fault plane), but without limiting events to the regions in which aftershocks occurred. The three spatial coordinates for each synthetic event are chosen randomly and independently from the probability distributions shown in Figure 5.1. The probability distributions were designed to produce sequences with plausible depth distribution for the region and

substantial clustering along the mainshock fault plane. The locations of ~25% of the events in each sequence are chosen by adding small perturbations to the locations of previously chosen events to introduce clustering into the sequences.

The three mechanism parameters are chosen randomly and independently from the probability distributions in Figure 5.1. These distributions are smoothed versions of the parameters for the observed sequences. The magnitude of each event is randomly chosen from a Gutenberg-Richter distribution, and the time chosen randomly assuming an Omori Law decay in seismicity rate. One hundred synthetic sequences are created for Landers and for Northridge. The CI for each sequence is found the same way as for the observed sequences, and the distribution of CI values for random sequences is determined.

5.2.3 Statistical Test

The distribution of CI values for the synthetic sequences is used to determine how confident one can be that the CI of the observed sequence is too large to have occurred simply by chance. This is equivalent to the confidence level at which one can reject the null hypothesis that the observed sequence CI is indistinguishable from that of the synthetic sequences. For example, if the CI of the observed sequence is at the 95th percentile of the distribution of CI values for the synthetic sequences, the confidence level is 95%. A weighted average of the confidence level, over the error bar of the CI of the observed sequence, is also found, and this is the confidence level reported.

5.3 Results

For both sequences, the Coulomb stress triggering model explains more than half of all the events (Figures 5.2 and 5.3 and Tables 5.1 and 5.2), 63±2% for Landers and 57±2% for Northridge. In both cases, this number is at the 99th percentile of the synthetic sequence distribution, so the null hypothesis that the observed sequence is indistinguishable from the synthetic sequences can be rejected with a high level of

confidence. This suggests that Coulomb stress changes played a significant role in the triggering of the aftershock sequences.

The distance to the fault and the magnitude of the stress change, which are inversely related, clearly affect the performance of the stress triggering model. For both sequences, the CI for events within 2-5 km of the mainshock fault is low. Proximity to the fault corresponds to high stress change, and the model performs particularly poorly for stress changes >100 bar. Events with such large stress changes are located very close to the fault and must be affected by small-scale slip heterogeneity, which cannot be well resolved, and by discontinuities in the modeled slip distributions due to fault discretization. The performance of the model is also poor for events very far from the fault, or equivalently, for small stress changes. The model appears to work best for stress changes >0.1 bar. This is presumably because the stress changes at large distances from the fault are too small to trigger a detectable number of earthquakes.

The Northridge sequence also exhibits a pattern with depth, with significantly better model performance a shallow depths. At all depths less than 10 km, the CI of the observed events is at least at the 95th percentile of the synthetic sequence CI distribution, whereas below 10 km depth, it is under the 90th percentile. If the shear strength of faults increases with depth due to increased confining pressure, it could be that static stress triggering cannot occur as easily at depth because the stress changes are a smaller fraction of the failure stress. However, the results of Chapter 2 suggest a gradual increase in fault strength down to ~15 km depth, and very low strength at greater depths.

Other spatial variations in the performance of the Coulomb stress triggering model can be seen in Figures 5.4 and 5.5. In the Northridge sequence, the major cluster of off-fault seismicity, to the NW of the mainshock, is explained very well by the Coulomb stress triggering model. In the Landers sequence, there are off-fault clusters, such as those near Barstow and Ridgecrest, which are explained well. However, there is also a cluster of events along the Pisgah Fault, to the east of the Landers rupture, which are predominately inconsistent with the modeled stress changes. The 1999 M_W7.1

Hector Mine earthquake occurred close to this cluster.

The focal mechanism of an individual event is clearly important in whether or not it is consistent with Coulomb stress triggering. However, no general difference is observed between the mechanism distributions of events consistent and inconsistent with triggering by static stress change (Figure 5.6).

A decrease in CI with time after the mainshock is to be expected, since postseismic relaxation, aseismic creep, subsequent earthquakes, and tectonic loading will modify the stress field and diminish the influence of the mainshock-induced stress changes. No significant change in CI is observed over the first month of either sequence, so I have determined CI versus time for both sequences through the end of 1999 (Figure 5.7 and Tables 5.3 and 5.4). The CI for pre-event seismicity is included for comparison. All events within about one fault length (80 km for Landers, 20 km for Northridge) were used. For Northridge, there appears to be a step in CI at the time of the mainshock, from CI≈45 to CI≈55, but it is difficult to resolve given the low levels of pre-event seismicity. There does not appear to be a decreasing trend in CI over the 6 years following the mainshock.

The CI in the Landers region shows a more clear evolution through time. Prior to the Landers sequence, CI≈40, whereas CI≈60-70 after the mainshock. It is important to note that the step from CI≈40 to CI≈60 took place at the time of the Joshua Tree preshock, even though only stress changes due to the Landers mainshock were modeled. The Joshua Tree sequence occurred on the southern extension of the Landers trend, an area which was reloaded by the mainshock [*Hauksson*, 1994], so it is not surprising that the CI is high. However, this observation illustrates that events which were not triggered can appear consistent with triggering due to geometric effects, which should encourage caution when interpreting results of triggering studies. There is a suggestion of a gradual decrease in CI over the 7 years following the Landers mainshock. A step back down to approximately the pre-event CI level occurs at the time of the 1999 M_W7.1 Hector Mine earthquake, located ~20 km from the Landers rupture. It is unfortunate that we will not be able to observe how the gradual decrease in CI after Landers would have continued. However, the step in CI

at the time of Hector Mine does illustrate the effects of subsequent major events on static stress triggering.

5.4 Discussion

The observed CI for the Landers and Northridge sequences indicate that Coulomb stress change plays a role in the triggering of aftershocks, but is probably not the only triggering mechanism. The CI of the observed sequences are usually significantly higher than the CI of comparable synthetic sequences, which suggests that some of the events were triggered by static stress changes. However, even for the parameter ranges where the model works the best, ~20-35% of the events are inconsistent with triggering. The number of events actually triggered, N_{trig}, can be estimated from the number of events consistent with triggering, N_{cons}. If the data set consists of N events, and P is the probability of an untriggered event appearing consistent with triggering (i.e., the CI of the synthetic sequences):

$$N_{cons} = N_{trig} + P(N - N_{trig}) \tag{5.4}$$

and therefore:

$$N_{trig} = \frac{N_{cons} - PN}{1 - P}. \tag{5.5}$$

For the best observed performance of the model (Figure 5.2), $N_{cons} \approx 0.8N$, and $P \approx 0.5$, so $N_{cons} \approx 0.6N$. This suggests that even in the best case, ~40% of the aftershocks were not triggered by Coulomb stress changes. An additional triggering mechanism appears to be necessary.

The Coulomb stress triggering model also fails to explain the occurrence of the 1999 M_W7.1 Hector Mine earthquake, a right-lateral strike-slip earthquake which occurred only ~20 km from the Landers rupture. The proximity of the two events in space and time suggests a triggering relationship, yet a pair of subparallel strike-slip earthquakes appears to be at odds with the Coulomb stress triggering model because the first earthquake should relieve shear stress on the fault plane of the second.

The Coulomb stress change due to Landers at the Hector Mine hypocenter, projected onto the preferred fault plane [*Scientists from the USGS, SCEC, and CDMG*, 2000], is -0.9 bar. Since the trend of the rupture varies along strike and the exact orientation of the initial rupture is not certain, I have modeled Coulomb stress change on planes of various orientation at four different depths (Figure 5.8). If the preferred orientation of the Hector Mine event is correct to within $\sim 15^o$ and the hypocentral depth, 5±3 km [*Scientists from the USGS, SCEC, and CDMG*, 2000], is correct to within ~4 km, the Coulomb stress change is still negative. Only for a larger value of μ (Figure 5.9) and a hypocentral depth of at least 9 km does a positive ΔCS occur for any fault orientation within 10^o of the preferred orientation.

One possible explanation for the apparent failure of the triggering model for Hector Mine is that the intervening 7 years of seismicity has significantly altered the stress field and diminished the effects of Landers. However, the high CI observed up until the time of the Hector Mine event (Figure 5.7) suggests that the post-Landers events had not had a major impact on the stress field over most of the region. Another possible explanation is that inaccuracies in the Landers slip distribution may be leading to errors in the modeled stress changes in the vicinity of Hector Mine. If significant left-lateral coseismic slip occurred along the aftershock trends conjugate to the northern Landers rupture, this could lead to positive ΔCS for the Hector Mine mainshock and the Landers aftershocks along the Pisgah Fault (Kenneth Hudnut, personal communication, 2000). The third alternative is that the Hector Mine earthquake was triggered by a mechanism other than static Coulomb stress change, such as unclamping of the fault, dynamic stress changes or pore pressure changes.

The difference between the results presented here and in *Hardebeck et al.* [1998], especially for the Northridge sequence, which *Hardebeck et al.* [1998] found to have a CI indistinguishable from that of the synthetic sequences, should also be cause for concern. The only difference between the two studies is that this work uses a larger and higher quality data set and a more correct representation of pore pressure changes. This implies that the results of quantitative studies are not stable with respect to the data set and/or the details of the modeling.

5.5 Conclusions

The Coulomb stress change triggering model was tested for the aftershock sequences of the 1992 Landers and 1994 Northridge earthquakes. The model is generally successful, since the number of aftershocks consistent with the model is larger than would be expected to appear consistent purely by chance. The model works best for events at intermediate distances from the mainshock, where the stress changes are between 0.1 bar and 100 bar. Stress changes very near the rupture plane are difficult to model because they depend on the small-scale features of slip which generally cannot be resolved, and they are affected by slip discontinuities due to the discretization of the fault. Far from the mainshock, the stress changes are presumably too small to trigger a detectable number of events.

Although the model performs better than it should by chance, at least 40% of the events appear not to have been triggered by static stress changes. This, along with the failure of the model to explain the apparent triggering of the M_W7.1 Hector Mine earthquake by Landers, implies that static stress change is not the only important mechanism in aftershock triggering. Dynamic stress changes and pore pressure changes may also play a role.

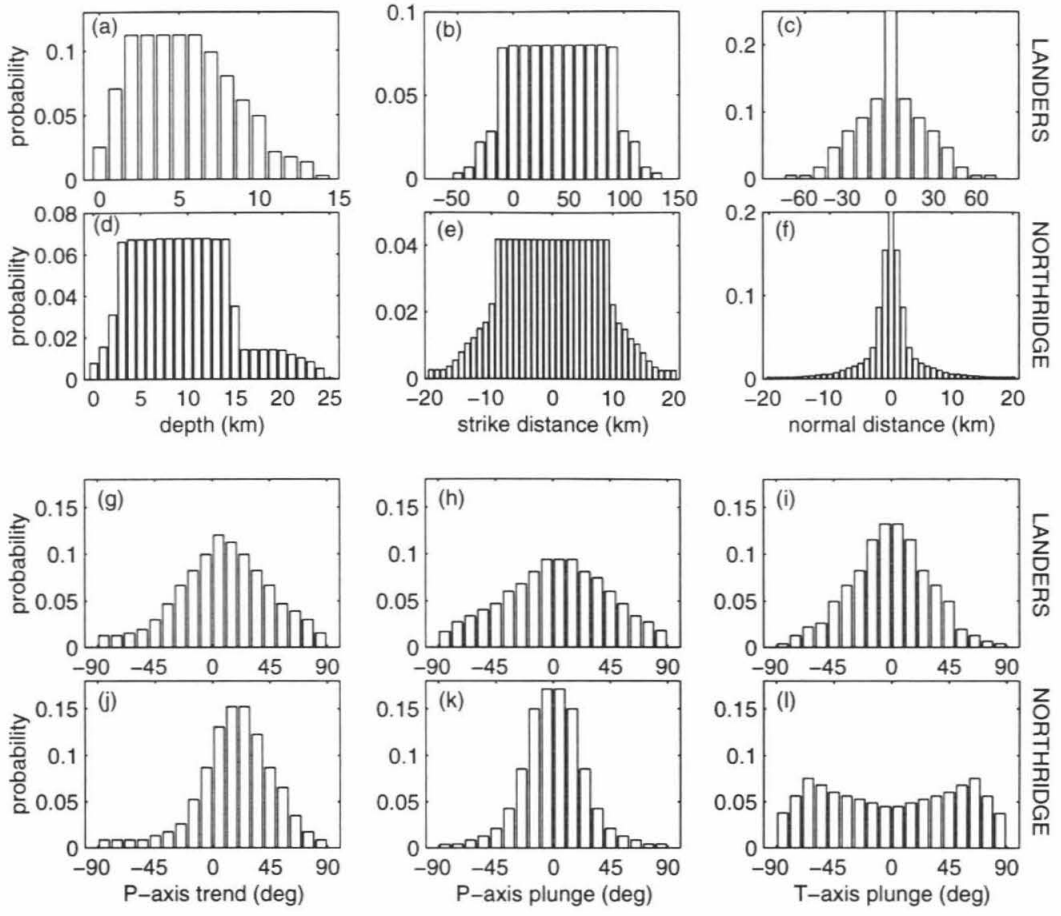

Figure 5.1: Probability distributions used to choose the spatial coordinates and focal mechanism parameters for the synthetic sequences. **(a)-(f)** Spatial coordinates. The "strike distance" is the along-strike distance measured from the center of the Northridge mainshock or the southern end of the Landers mainshock. The "normal distance" is the distance in the direction normal to the fault, measured from the nearest mainshock fault segment or its extension. **(g)-(l)** Focal mechanism parameters. The P-axis trend is measured clockwise from north; and the plunge, down from horizontal. The T-axis plunge is positive for a clockwise rotation around the P-axis.

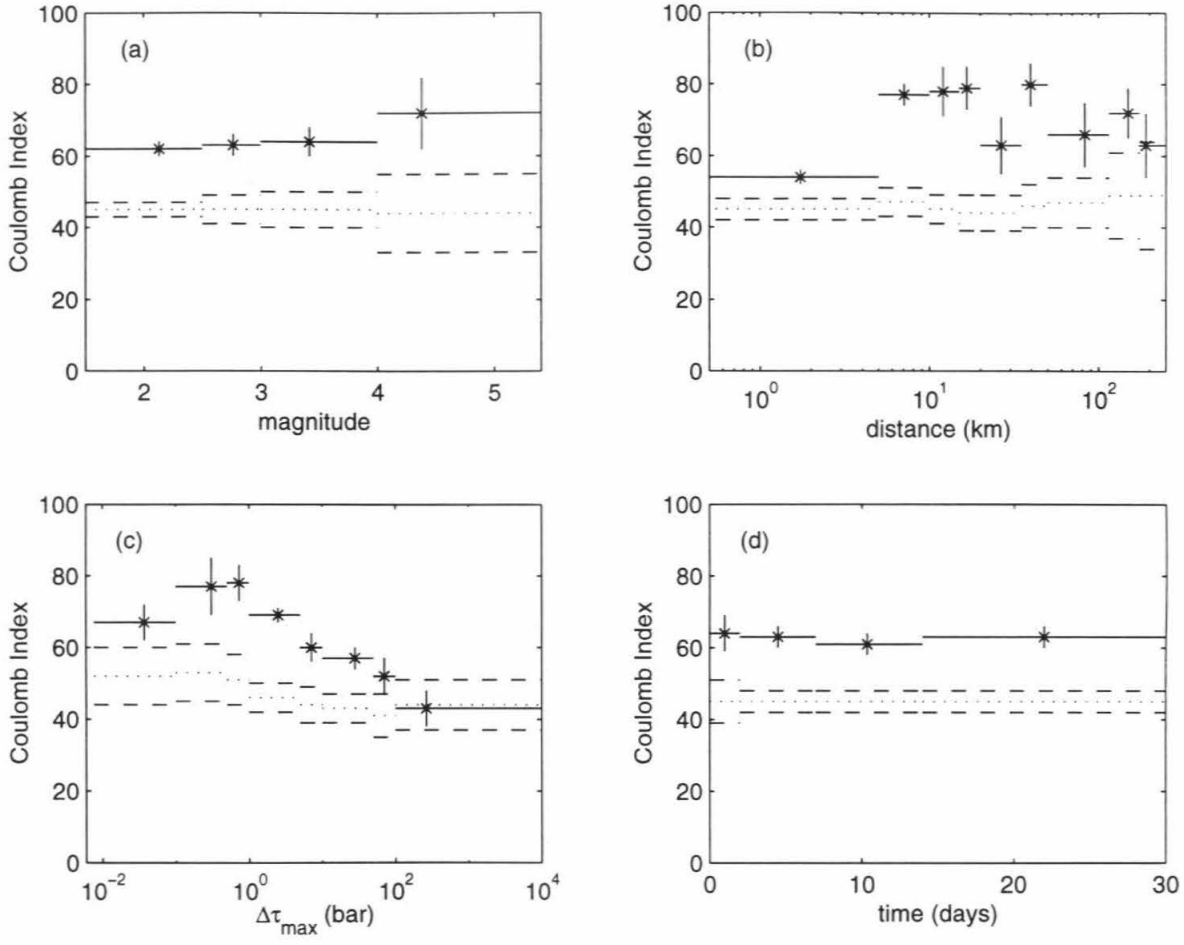

Figure 5.2: The Coulomb Index (CI), the percentage of events consistent with the Coulomb stress triggering model, for the Landers sequence. The asterisks indicate the CI for a bin versus the average parameter value in that bin. The vertical error bars indicate the 2σ error estimates; and the horizontal bars, the bins. The dotted and dashed lines indicate the mean CI for the synthetic sequences and the 2σ level of their distribution, respectively. **(a)** CI versus aftershock magnitude. **(b)** CI versus distance from the nearest point on the mainshock fault plane. **(c)** CI versus the magnitude of the stress change, represented by $\Delta\tau_{max}$, the maximum shear stress change on any plane. **(d)** CI versus time after the mainshock.

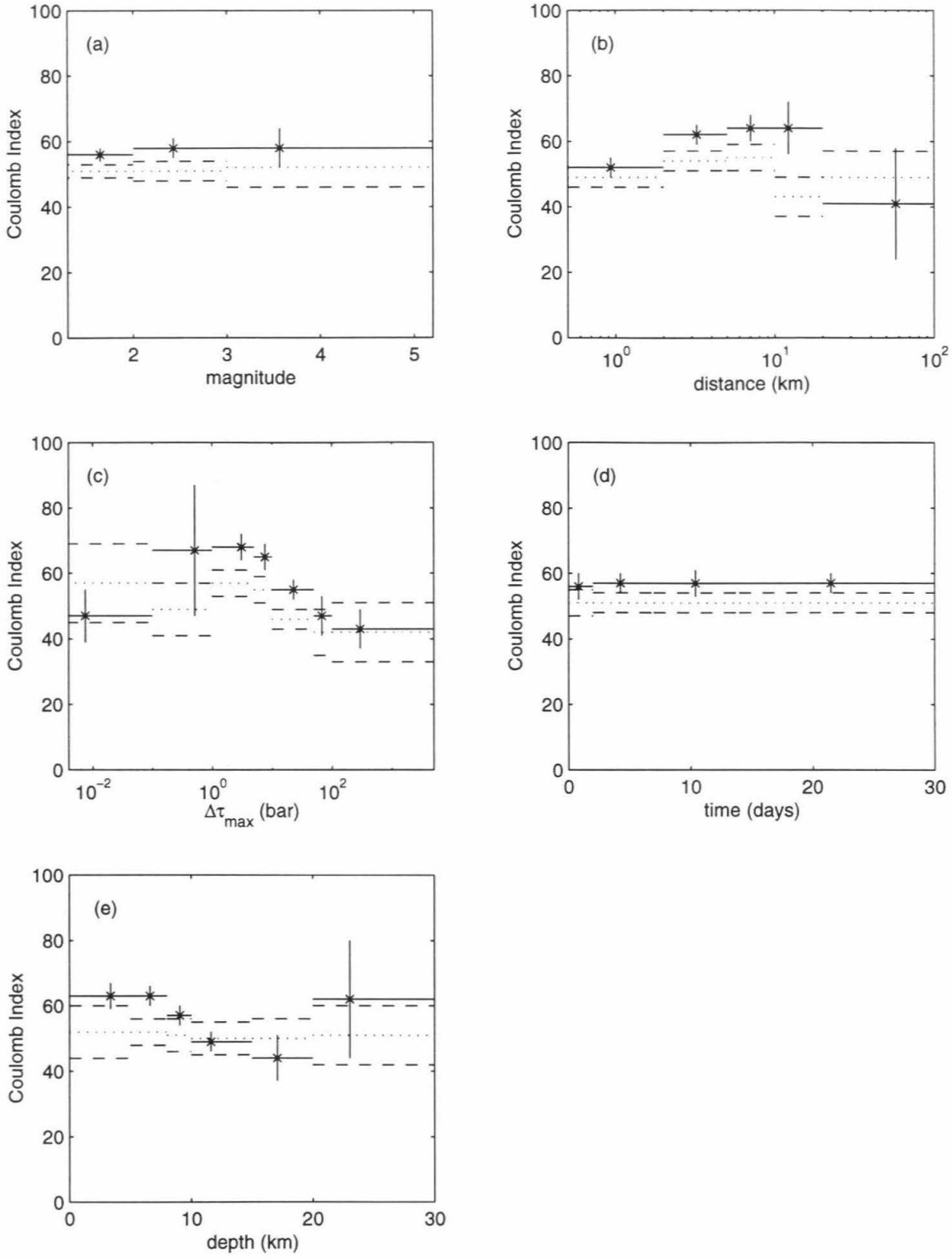

Figure 5.3: The Coulomb Index for the Northridge sequence, symbols as in Figure 5.2. **(a)** CI versus aftershock magnitude. **(b)** CI versus distance from the mainshock. **(c)** CI versus the magnitude of the stress change. **(d)** CI versus time. **(e)** CI versus aftershock hypocentral depth.

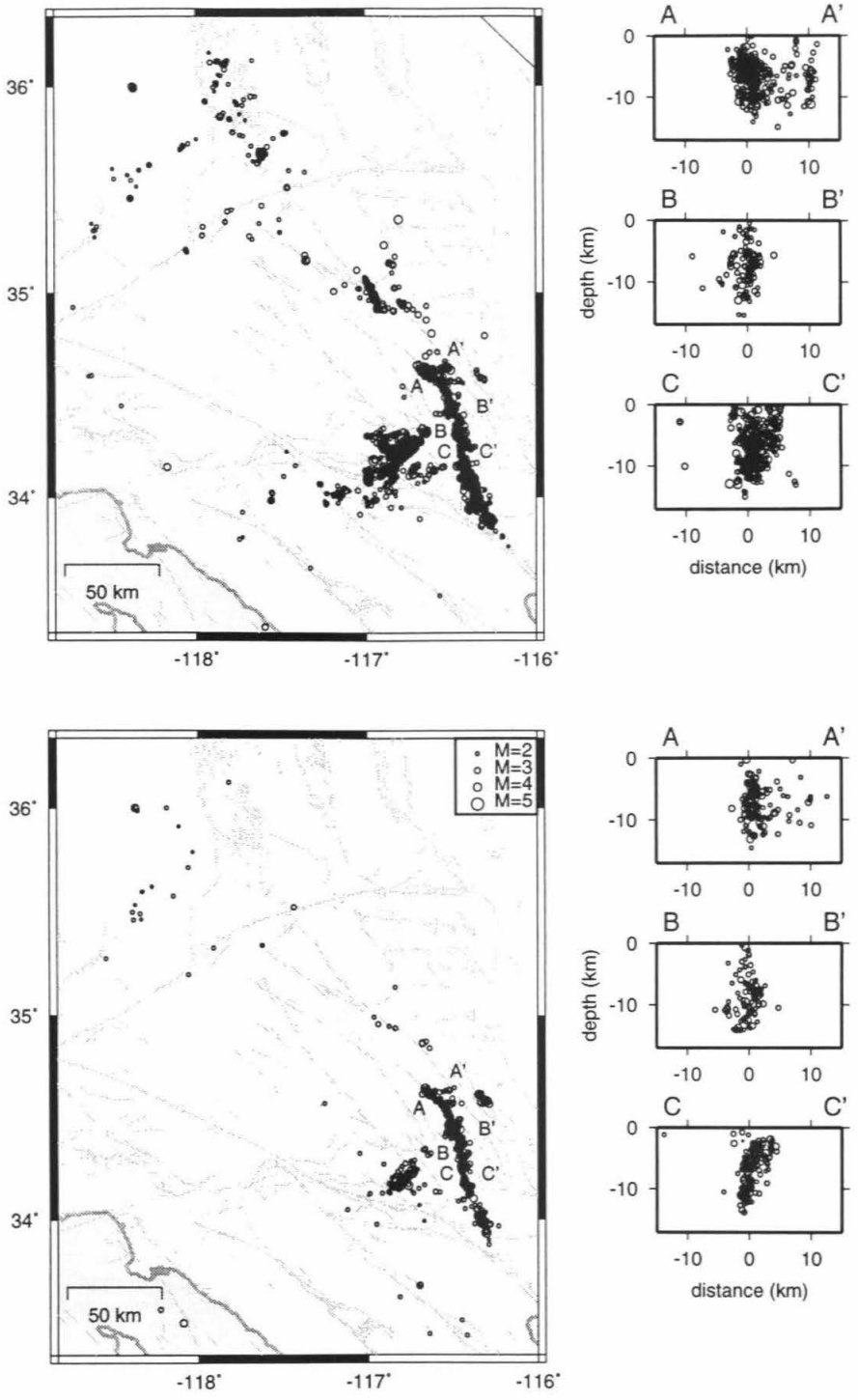

Figure 5.4: Earthquakes occurring within one month after the Landers mainshock. Events in the top panel have at least one nodal plane consistent with Coulomb stress triggering. Events with both planes inconsistent with triggering are shown in the bottom panel. Major faults shown in gray. The aftershocks clearly delineate the mainshock fault plane.

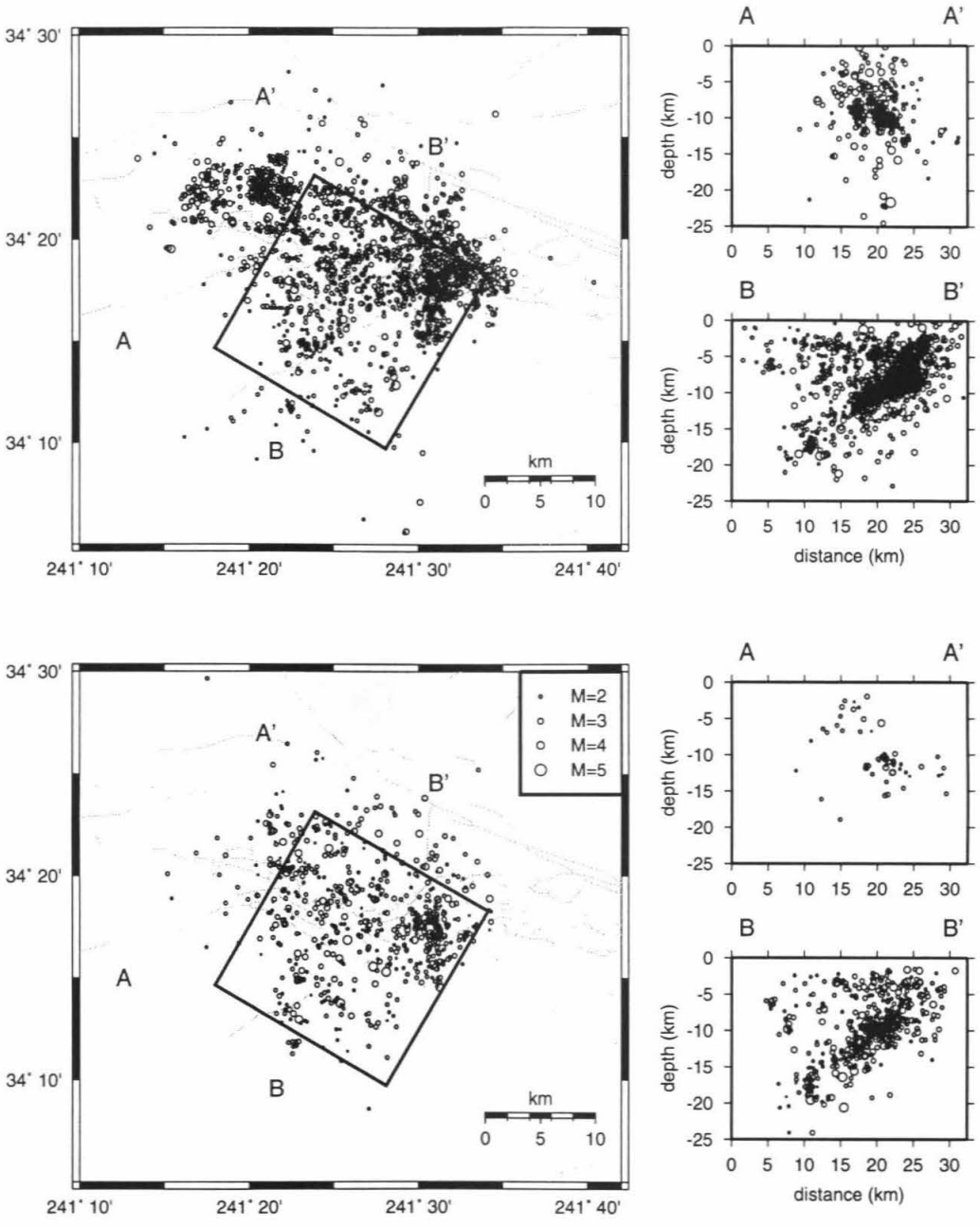

Figure 5.5: Earthquakes occurring within one month after the Northridge mainshock. Events in the top panel have at least one nodal plane consistent with Coulomb stress triggering. Events with both planes inconsistent with triggering are shown in the bottom panel. Major faults shown in gray. The black rectangle indicates the surface projection of the mainshock fault plane.

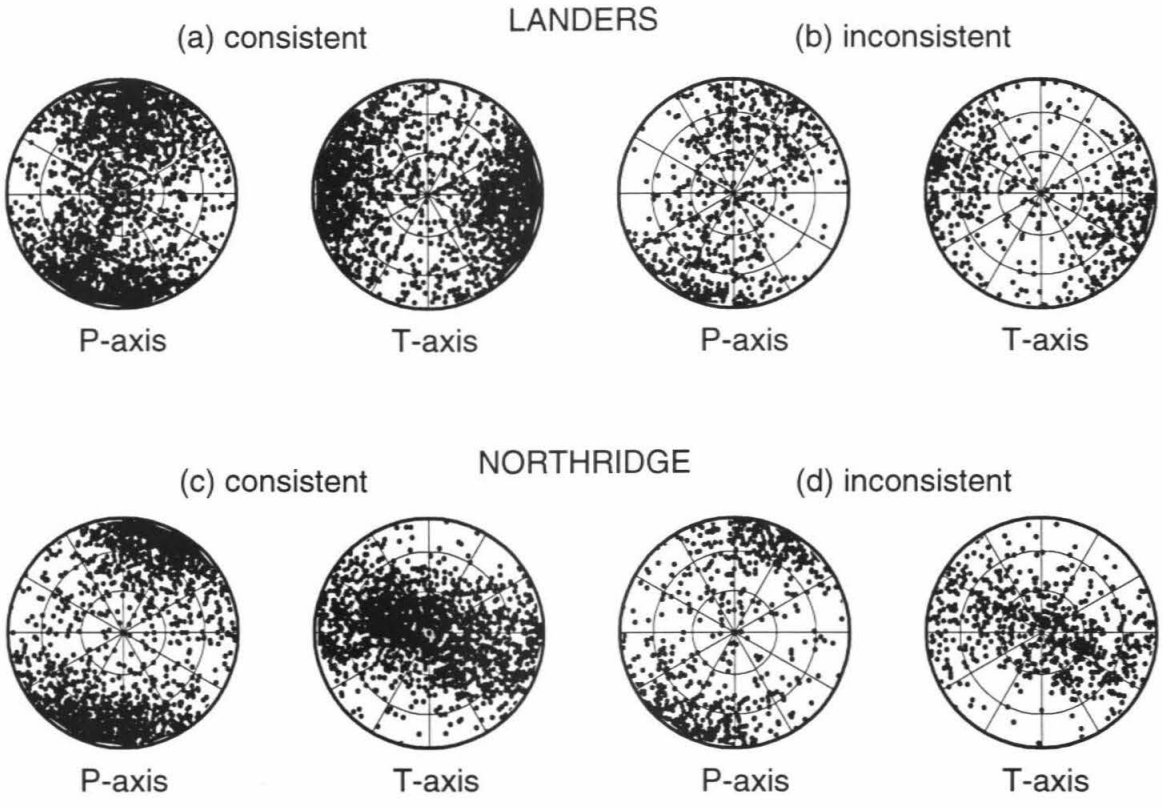

Figure 5.6: Stereographic plots of the P and T axes of the first month of aftershocks. **(a)** Landers aftershocks with at least one nodal plane consistent with triggering. **(b)** Landers aftershocks with both nodal planes inconsistent. **(c)** Northridge aftershocks with at least one plane consistent. **(d)** Northridge aftershocks with both planes inconsistent.

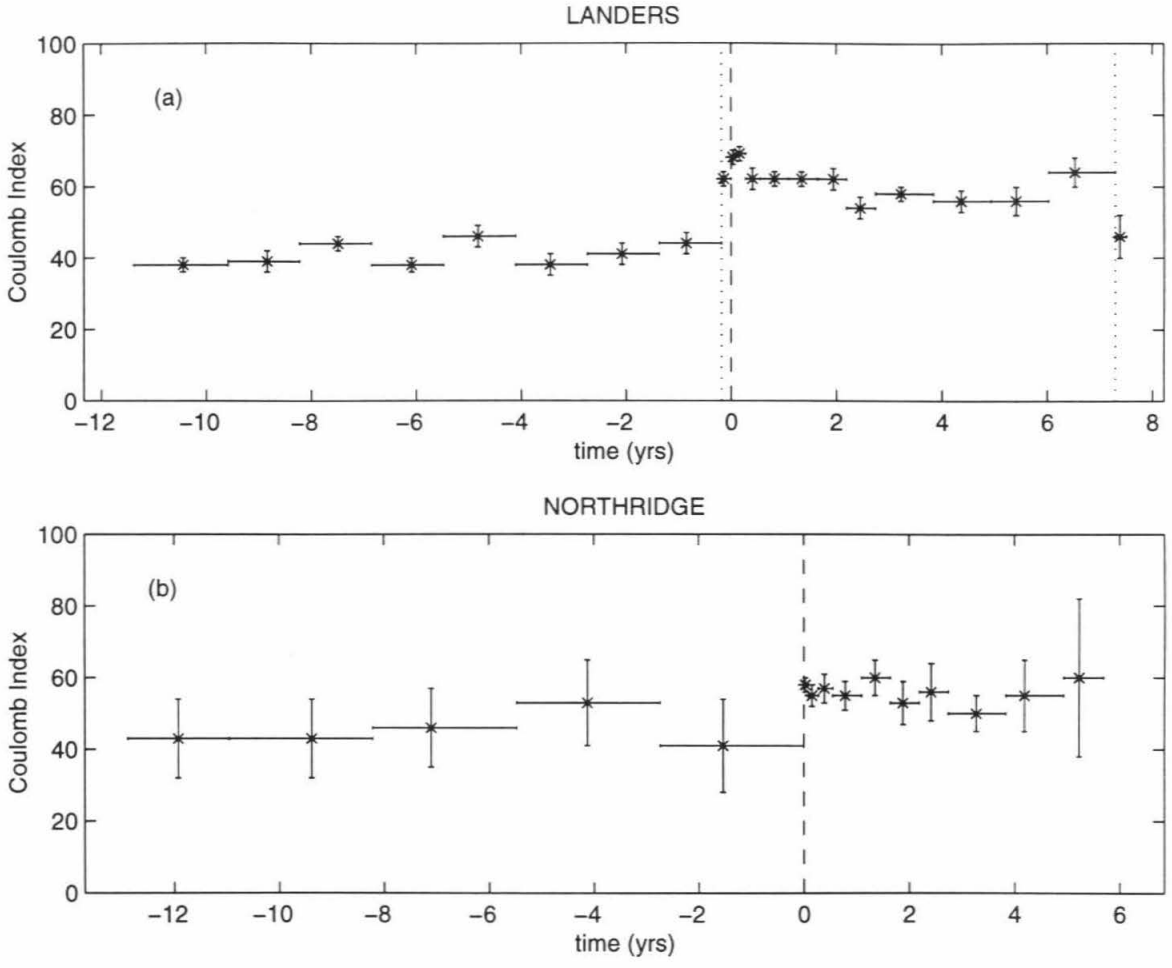

Figure 5.7: Coulomb Index (CI) versus time, for all events within one fault length of the mainshock (80 km for Landers, 20 km for Northridge). The asterisks indicate the CI for a bin versus the average event time in that bin. The vertical error bars indicate the 2σ error estimates; and the horizontal bars, the bins. **(a)** CI versus time for Landers. The vertical dashed line indicates the time of the mainshock. The vertical dotted lines indicate the times of the Joshua Tree foreshock and the Hector Mine earthquake. **(b)** CI versus time for Northridge. The vertical dashed line indicates the time of the mainshock.

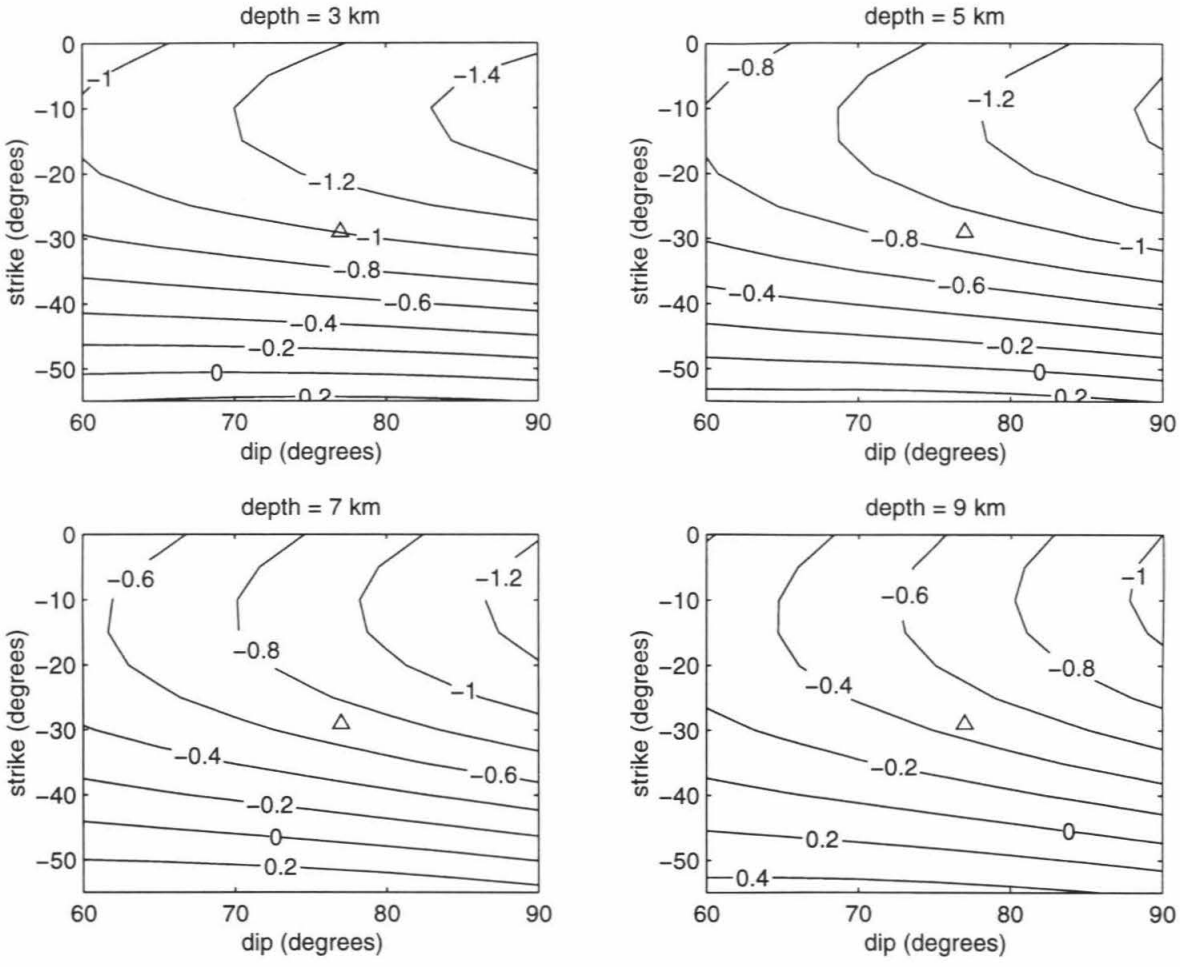

Figure 5.8: Contours of Coulomb stress change due to the Landers mainshock on the Hector Mine hypocenter for various fault plane orientations and hypocentral depths. The open triangle indicates the preferred fault plane orientation [*Scientists from the USGS, SCEC, and CDMG*, 2000]; the preferred depth is 5±3 km. The contours are in bars. The coefficient of friction, μ, is assumed to be 0.6.

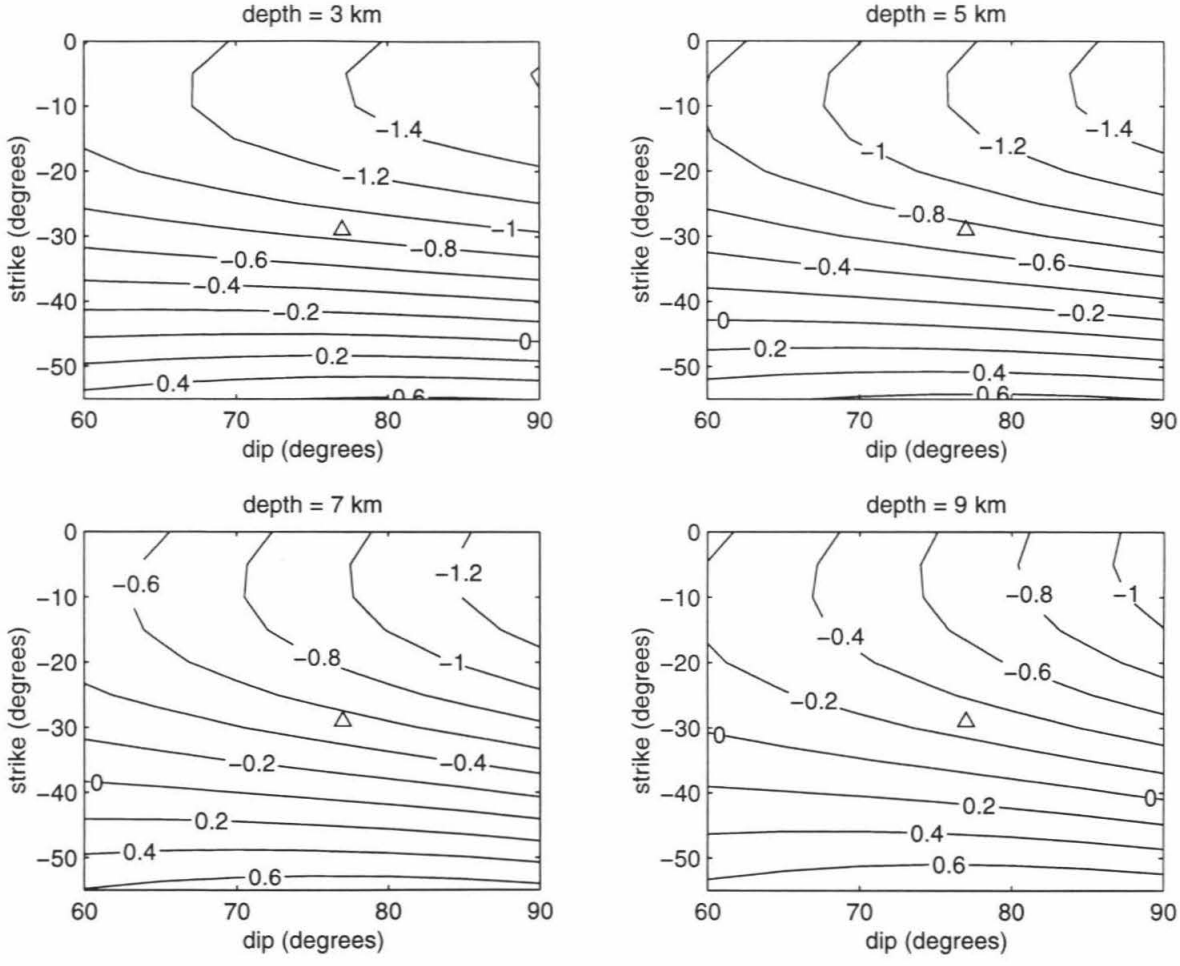

Figure 5.9: The same as Figure 5.8, except with μ=0.85.

Data Set or Parameter Value	Number of Events	Observed CI ($\pm 2\sigma$)	Synthetic CI ($\pm 2\sigma$)	Confidence Level
all	3204	63 ± 2	45 ± 2	99%
$M \leq 2.5$	1980	62 ± 2	45 ± 2	99%
$2.5 < M \leq 3$	754	63 ± 3	45 ± 4	99%
$3 < M \leq 4$	407	64 ± 4	45 ± 5	99%
$M > 4$	63	72 ± 10	44 ± 11	99%
$D \leq 5$ km	1843	54 ± 2	45 ± 3	99%
$5 < D \leq 10$	549	77 ± 3	47 ± 4	99%
$10 < D \leq 15$	128	78 ± 7	45 ± 4	99%
$15 < D \leq 20$	131	79 ± 6	44 ± 5	99%
$20 < D \leq 35$	130	63 ± 8	44 ± 5	99%
$35 < D \leq 50$	146	80 ± 6	46 ± 6	99%
$50 < D \leq 115$	75	66 ± 9	47 ± 7	98%
$115 < D \leq 175$	116	72 ± 7	49 ± 12	99%
$D > 175$	86	63 ± 9	49 ± 15	90%
$\Delta\tau_{max} \leq 0.1$ bar	228	67 ± 5	52 ± 8	98%
$0.1 < \Delta\tau_{max} \leq 0.5$	74	77 ± 8	53 ± 8	99%
$0.5 < \Delta\tau_{max} \leq 1$	218	78 ± 5	51 ± 7	99%
$1 < \Delta\tau_{max} \leq 5$	1069	69 ± 2	46 ± 4	99%
$5 < \Delta\tau_{max} \leq 10$	369	60 ± 4	44 ± 5	99%
$10 < \Delta\tau_{max} \leq 50$	685	57 ± 3	43 ± 4	99%
$50 < \Delta\tau_{max} \leq 100$	304	52 ± 5	41 ± 6	98%
$\Delta\tau_{max} > 100$	257	43 ± 5	44 ± 7	35%
$t \leq 2$ days	294	64 ± 5	45 ± 6	99%
$2 < t \leq 7$	780	63 ± 3	45 ± 3	99%
$7 < t \leq 14$	847	61 ± 3	45 ± 3	99%
$7 < t \leq 30$	1283	63 ± 3	45 ± 3	99%

Table 5.1: The Coulomb Index (CI), the percent of events consistent with triggering, for the first month of Landers aftershocks. M indicates the aftershock magnitude, D the distance from the mainshock fault, $\Delta\tau_{max}$ the magnitude of stress change (the maximum shear stress change on a plane of any orientation), and t the time since the mainshock. Also shown is the mean and standard deviation of the distribution of CI values for a suite of random, synthetic sequences, and the confidence level at which one can reject the null hypothesis that the observed CI came from this distribution.

Data Set or Parameter Value	Number of Events	Observed CI ($\pm 2\sigma$)	Synthetic CI ($\pm 2\sigma$)	Confidence Level
all	2737	57 ± 2	51 ± 2	99%
$M \leq 2$	1507	56 ± 2	51 ± 2	98%
$2 < M \leq 3$	1008	58 ± 3	51 ± 3	99%
$M > 3$	222	58 ± 6	52 ± 6	90%
$D \leq 2$ km	1219	52 ± 3	49 ± 3	91%
$2 < D \leq 5$	835	62 ± 3	54 ± 3	98%
$5 < D \leq 10$	415	64 ± 4	55 ± 4	98%
$10 < D \leq 20$	98	64 ± 8	43 ± 6	99%
$D > 20$	27	41 ± 17	49 ± 8	19%
$\Delta\tau_{max} \leq 0.1$ bar	158	47 ± 8	57 ± 12	6%
$0.1 < \Delta\tau_{max} \leq 1$	23	67 ± 20	49 ± 8	93%
$1 < \Delta\tau_{max} \leq 5$	330	68 ± 4	57 ± 4	98%
$5 < \Delta\tau_{max} \leq 10$	603	65 ± 4	55 ± 4	98%
$10 < \Delta\tau_{max} \leq 50$	1265	55 ± 3	46 ± 3	99%
$50 < \Delta\tau_{max} \leq 100$	234	47 ± 6	42 ± 7	81%
$\Delta\tau_{max} > 100$	124	43 ± 6	42 ± 9	58%
$t \leq 2$ days	459	56 ± 4	51 ± 4	92%
$2 < t \leq 7$	761	57 ± 3	51 ± 3	98%
$7 < t \leq 14$	653	57 ± 4	51 ± 3	97%
$t > 14$	864	57 ± 3	51 ± 3	98%
$z \leq 5$ km	487	63 ± 4	52 ± 8	95%
$5 < z \leq 8$	635	63 ± 3	52 ± 4	99%
$8 < z \leq 10$	730	57 ± 3	51 ± 5	95%
$10 < z \leq 15$	693	49 ± 3	50 ± 5	25%
$15 < z \leq 20$	168	44 ± 7	50 ± 6	7%
$z > 20$	24	62 ± 18	51 ± 9	84%

Table 5.2: The Coulomb Index (CI), the percent of events consistent with triggering, for the first month of Northridge aftershocks. M indicates the aftershock magnitude, D the distance from the mainshock fault, $\Delta\tau_{max}$ the magnitude of stress change (the maximum shear stress change on a plane of any orientation), t the time since the mainshock, and z the aftershock hypocentral depth. Also shown is the mean and standard deviation of the distribution of CI values for a suite of random, synthetic sequences, and the confidence level at which one can reject the null hypothesis that the observed CI came from this distribution.

Time (yy/mm/dd) Begining	End	Number of Events	CI	($\pm 2\sigma$)	notes
81/02/13	82/11/27	1851	38	± 2	pre-Landers
82/11/27	84/04/11	739	39	± 3	
84/04/11	85/08/23	1526	44	± 2	
85/08/23	87/01/04	1857	38	± 2	
87/01/04	88/05/19	956	46	± 3	
88/05/19	89/10/01	996	38	± 3	
89/10/01	91/02/15	796	41	± 3	
91/02/15	92/04/23	516	44	± 3	
92/04/23	92/06/28	2225	62	± 2	Joshua Tree sequence
92/06/28	92/07/28	2982	68	± 2	Landers sequence
92/07/28	92/10/06	2102	69	± 2	
92/10/06	93/01/14	980	62	± 3	
93/01/14	93/08/02	1310	62	± 2	
93/08/02	94/02/18	1173	62	± 2	
94/02/18	94/09/06	927	62	± 3	
94/09/06	95/03/25	824	54	± 3	
95/03/25	96/04/28	1146	58	± 2	
96/04/28	97/06/02	677	56	± 3	
97/06/02	98/07/07	599	56	± 4	
98/07/07	99/10/16	447	64	± 4	
99/10/16	99/12/26	225	46	± 6	Hector Mine sequence

Table 5.3: The Coulomb Index (CI) for earthquakes occurring within 80 km of the Landers mainshock, versus time.

Time (yy/mm/dd)		Number of			
Begining	End	Events	CI	($\pm 2\sigma$)	notes
81/03/02	83/02/06	53	43	± 11	pre-Northridge
83/02/06	85/11/01	56	43	± 11	
85/11/01	88/07/27	58	46	± 11	
88/07/27	91/04/22	54	53	± 12	
91/04/22	94/01/17	48	41	± 13	
94/01/17	94/02/16	2535	58	± 2	post-Northridge
94/02/16	94/04/27	1048	55	± 3	
94/04/27	94/08/05	494	57	± 4	
94/08/05	95/02/21	519	55	± 4	
95/02/21	95/09/09	270	60	± 5	
95/09/09	96/03/27	193	53	± 6	
96/03/27	96/10/13	103	56	± 8	
96/10/13	97/11/17	228	50	± 5	
97/11/17	98/12/22	60	55	± 10	
98/12/22	99/09/25	20	60	± 22	

Table 5.4: The Coulomb Index (CI) for earthquakes occurring within 20 km of the Northridge mainshock, versus time.

Appendix A An Evaluation of Stress Orientation Inversion Methods

A.1 Introduction

The results of Chapters 1, 2, and 3 depend on stress orientations obtained from the inversion of earthquake focal mechanisms. Therefore, it is important to thoroughly test the inversion method. It is also important to test stress inversion techniques because there is a long-standing debate as to which of two competing methods produces the best results.

The linear inversion method [*Michael*, 1984, 1987b] which I use is unnamed, but I will refer to it as LSIB (Linear Stress Inversion with Bootstrapping) for convenience. The other commonly used inversion method is a grid search method called FMSI (Focal Mechanisms Stress Inversion) [*Gephart and Forsyth*, 1984; *Gephart*, 1990a]. These two methods typically obtain similar stress orientations for similar focal mechanism data sets. However, the uncertainty estimates are often quite different, with the confidence regions given by FMSI usually much larger than those of LSIB.

The uncertainty estimates have important implications for understanding spatial and temporal variations in the stress field. In southern California, for example, many spatial variations and temporal changes related to major earthquakes have been observed (*Hauksson* [1990]; *Kerkela and Stock* [1996]; *Michael* [1987b]; *Hauksson* [1994]; *Zhao et al.* [1997], and Chapters 1, 2, and 3), which are statistically significant according to the uncertainty estimates of LSIB and other techniques which utilize bootstrap error estimation. However, when an inversion method similar to FMSI is used, very few stress variations are found to be larger than the estimated uncertainties, and the stress field in southern California can be concluded to be generally homogeneous [*Abers and Gephart*, 1997].

Jones [1988] and *Wyss and Lu* [1995] used identical data sets to study stress orientations along the San Andreas Fault in southern California, and both found that the stress state was different along different segments of the fault. However, these differences appear to be significant at the 95% confidence level if LSIB is used [*Jones*, 1988], but not if FMSI is used [*Wyss and Lu*, 1995].

To resolve whether or not the observed stress field heterogeneity in southern California and along the San Andreas Fault is real, one must determine which of the uncertainty estimates best reflects the precision with which stress orientations can be determined from focal mechanisms.

The two inversion methods cannot be directly compared because they are conceptually very different. For this reason, I compare the performance of the two methods on a suite of synthetic data sets. The focus is on the accuracy of the results and the appropriateness of the confidence regions computed by each method.

A.2 Inversion Methods

All methods for inverting focal mechanisms for stress orientation rest on the assumption that earthquakes slip in the direction of the resolved shear stress on the fault plane. The orientation of the fault plane is usually not considered to be information about the stress state, as it may be a randomly-oriented preexisting plane of weakness. The goal of an inversion is to find the stress state which minimizes the discrepancy between the resolved shear stress direction and the slip direction, for all earthquakes in the data set.

Only geometrical information is used, so the isotropic and deviatoric stress magnitudes can't be estimated, and there are only four independent model parameters. Typically, three parameters are chosen to indicate the orientations of the three principal stress axes, and the fourth parameter

$$R = \frac{\sigma_1 - \sigma_2}{\sigma_1 - \sigma_3} \tag{A.1}$$

indicates the relative magnitudes of the stress axes, where σ_1, σ_2, and σ_3 are the magnitudes of the maximum, intermediate, and minimum compressive stresses, respectively. For a reliable inversion, the orientations of the fault planes must be adequately diverse to sample the entire stress tensor.

There are two basic assumptions in the inversion procedures. The first is that the four stress parameters are constant over the spatial and temporal extent of the data set. The validity of this assumption can be tested for a particular data set using the misfits of the best-fitting stress model [*Michael*, 1991]. The second assumption, that slip is in the direction of resolved shear stress, implies isotropic fault planes, without a preferred direction of slip. Real faults may not be isotropic, but, unless there is systematic anisotropy in the set of faults used in an inversion, this simply adds some random noise. *Pollard et al.* [1993] demonstrated that fault length-to-width ratios and proximity to the free surface can also cause discrepancies between the slip direction and the direction of resolved shear stress, but that these errors are small relative to common measurement errors.

A persistent problem with focal mechanism inversions is the ambiguity between the fault and auxiliary planes. For discussion of fault plane selection methods, and the impact of incorrectly chosen planes on inversion results, see *Michael* [1987a] and *Lund and Slunga* [1999].

A.2.1 Linear Inversion Method

The linear inversion method (LSIB) solves for the stress tensor using a linear, least-squares inversion [*Michael*, 1984]. The stress inversion problem is nonlinear, but can be linearized by assuming that the magnitude of the shear traction on each fault plane is approximately the same. This assumption has some physical basis because the planes which fail in earthquakes are likely to be near some failure stress.

The inversion setup is:

$$\begin{pmatrix} \bar{\bar{A}}_1 \\ \bar{\bar{A}}_2 \\ \vdots \end{pmatrix} \bar{\Sigma} = \begin{pmatrix} \hat{s}_1 \\ \hat{s}_2 \\ \vdots \end{pmatrix} \tag{A.2}$$

where $\bar{\bar{A}}_j$ is a matrix determined from the orientation of the jth fault plane, $\bar{\Sigma}$ is a vector of the stress tensor parameters, and $\hat{s}_j$ is a unit vector in the slip direction of the jth event. The least-squares inversion minimizes the difference between $\hat{s}_j$ and $\bar{\tau}_j = \bar{\bar{A}}_j \bar{\Sigma}$, the vector of resolved shear stress on the jth plane.

Confidence regions are determined using a bootstrap technique [*Michael*, 1987b]. The data set is resampled, with replacement, hundreds or thousands of times to simulate repeated samples of the population from which the data came, and each resampling is inverted for the stress tensor. The $X\%$ of inversion results closest to the initial result, where closeness is defined by the normalized tensor dot product for stress tensor representations with zero isostatic component, are used to define the $X\%$ confidence region. (The symbol X is used in this chapter to represent the confidence level when statements are made which hold for any level of confidence.) This technique is appropriate for data containing errors because the observed variation in the data is used to estimate the confidence regions. I use 2000 bootstrap resamplings, which is adequate to produce stable confidence regions up to the 95% level [*Michael*, 1987b]. To address the fault plane ambiguity of the focal mechanisms, each nodal plane has a 50% probability of being chosen during bootstrap resampling.

The assumptions of this method are that the tractions on all fault planes are of similar magnitude and that the data set is adequately representative of the population and exhibits the full range of error.

A.2.2 Grid Search Method

The other widely-used method, FMSI, uses a grid search over stress field parameter space to find the stress tensor which minimizes the misfit between model and data [*Gephart and Forsyth*, 1984; *Gephart*, 1990a]. The misfit computed for each event

is the minimum angle of rotation of the focal mechanism, about any axis, necessary to bring the slip direction into alignment with the resolved shear stress on the fault plane. Fault plane ambiguity is addressed by using the nodal plane with the smaller misfit. The L1 norm is used to find the total misfit, Σ, for a given stress state.

I perform an initial search over all of parameter space using a coarse grid with 10^o spacing, and a second finer search with 5^o spacing in the vicinity of the best-fit solution.

Confidence regions are estimated from the distribution of misfit values. The statistics are based on those derived for the L1 norm by *Parker and McNutt* [1980]. For N measurements $x_1, x_2, \ldots, x_N$, where each measurement x_j is a normally-distributed random variable with mean 0 and standard deviation σ_j, the random variable

$$m = \sum_{j=1}^{N} \frac{|x_j|}{\sigma_j} \tag{A.3}$$

has an expected value of

$$E[m] = \left(\frac{2}{\pi}\right)^{1/2} N \tag{A.4}$$

and a variance of

$$var[m] = \sigma^2 = \left(1 - \frac{2}{\pi}\right) N. \tag{A.5}$$

This distribution is approximately Gaussian for $N \geq 10$. If $x_1, x_2, \ldots, x_N$ represent the individual mechanism misfits due to data errors, Equations A.4 and A.5 describe the probability distribution for the total misfit of the correct stress state.

In order to use these statistics, however, the standard deviation of the misfit due to data errors, σ_{est} (assuming $\sigma_j \approx \sigma_{est}$, for all j), needs to be estimated. Assuming that the total misfit value for the best-fitting stress state, Σ_{min}, is the expected value of the total misfit for the correct stress state, then

$$\Sigma_{min} = E\left[\sum_{j=1}^{N} |x_j|\right] = E[m\sigma_{est}] = \sigma_{est} E[m] = \sigma_{est}\left(\frac{2}{\pi}\right)^{1/2} N \tag{A.6}$$

and therefore

$$\sigma_{est} = \frac{\Sigma_{min}}{(2/\pi)^{1/2} N}. \tag{A.7}$$

Since the model has four parameters, FMSI uses

$$\sigma_{est} = \frac{\Sigma_{min}}{(2/\pi)^{1/2} (N-4)}, \tag{A.8}$$

which makes a noticeable difference in the confidence regions only for small data sets.

The $X\%$ confidence region is defined by stress states with misfits less than Σ_X, where there is a $(100-X)\%$ chance that the correct stress state could have a misfit greater than Σ_X due to data errors. This is equivalent to a $(100-X)\%$ probability of obtaining $m > M_X \equiv \Sigma_X/\sigma_{est}$ from the normal distribution of m, so

$$M_X = z_X \sigma + E[m] \tag{A.9}$$

where z_X is the number of standard deviations corresponding to $X\%$ of the area under the positive half of a normal distribution (since no misfits are less than Σ_{min}), e.g., z_{95}=1.96.

The threshold value is found by substituting Equations A.4 and A.5 into Equation A.9:

$$\frac{\Sigma_X}{\sigma_{est}} = z_X \left[\left(1 - \frac{2}{\pi}\right) N\right]^{1/2} + \left(\frac{2}{\pi}\right)^{1/2} N \tag{A.10}$$

and combining with Equation A.8

$$\Sigma_X = \left(\frac{z_X(\pi/2-1)^{1/2} N^{1/2} + N}{N-4}\right) \Sigma_{min}. \tag{A.11}$$

The assumptions which go into these confidence regions are that the individual event misfits due to data errors are normally distributed with a constant standard deviation, and that the total misfit of the best-fit solution, Σ_{min}, is the expected value of the total misfit of the correct solution, $\sigma_{est} E[m]$.

A.3 Testing the Inversion Methods

I examine the accuracy of the two inversion methods and the appropriateness of their uncertainty estimates by testing them on a suite of synthetic focal mechanism data sets. The design of synthetic data is inevitably subjective, but I attempt to create synthetic data sets which resemble real noisy data as much as possible.

A.3.1 Synthetic Data Sets

Each synthetic data set consists of a collection of focal mechanisms all consistent with a single specified stress state. The orientation of the principal stress axes is chosen randomly from a uniform spatial distribution, and a value is selected for R.

The fault plane orientations are chosen at random from a uniform spatial distribution. I make the somewhat counterintuitive choice of uniformly distributed planes based on the observation that small earthquakes, in contrast with larger events, tend to occur on diverse fault planes. It is these smaller events which are typically used as stress indicators. The choice of uniformly distributed planes is at odds with LSIB's assumption of similar magnitude shear stress on all planes, and should therefore be the toughest test of this technique. The rake of each event is chosen to be in the direction of resolved shear stress on the fault plane.

Random errors are introduced into the data sets by rotating each mechanism about some axis. The axes are chosen from a uniform spatial distribution. An exponential probability distribution is used to select rotation angles. Random polarity and location errors lead to errors in first-motion focal mechanisms with an exponential, rather than normal, distribution (Figure A.1). Additionally, studies using real data find that the residuals for the best-fitting stress state are often exponentially distributed [*Gephart and Forsyth*, 1984; *Gephart*, 1990b]. The fault plane or the auxiliary plane is randomly selected for inclusion in the data set, with a 50% probability of each.

Data sets with varying amounts of error, number of events and values of R are created, to observe whether these parameters affect the inversion results. Mechanism

errors of 5^o, 10^o, 15^o, 20^o, 30^o and 40^o are used. These numbers represent the parameter μ, where the exponential probability distribution function is defined as $\frac{1}{\mu}e^{-x/\mu}$. Values of 0, 0.2, 0.4, 0.5, 0.6, 0.8, and 1 are used for R. Data sets include 20, 50, 100, or 300 events. Fifty data sets are created for most combinations of values for these three parameters.

A.3.2 Testing

The accuracy of the inversion methods, and the appropriateness of their uncertainty estimates, are tested by inverting each of the synthetic data sets using both methods. First, I test the accuracy of the inversion results, defined as the angle between the correct and best-fitting stress orientations and the difference in R value.

I then test the appropriateness of the uncertainty estimates. If the confidence regions are appropriate, the correct stress state should fall within the $X\%$ confidence region for approximately $X\%$ of the data sets, for all X. The number of times the correct stress state falls into the $X\%$ confidence region, plotted versus X, should approximate a straight line. If the confidence regions are systematically too large or too small, it will fall above or below this line, respectively, as illustrated in Figure A.2.

When evaluating FMSI, the correct stress state is considered to be inside the $X\%$ confidence region if $\Sigma_{cor} \leq \Sigma_X$, where Σ_{cor} is the total misfit of the nearest grid point to the correct stress state. For LSIB, the correct stress state is considered to be inside the $X\%$ confidence region if it is closer to the best-fit stress state than $(100 - X)\%$ of the bootstrap resampling inversion results, closeness again measured by the normalized tensor dot product.

A.4 Results

A.4.1 Accuracy

The accuracy with which both inversion methods determine the stress parameters (Figure A.3, Figure A.4) is generally good. The accuracy of FMSI is on average slightly better, with a mean orientation error over all the test data sets of 11^o, and a mean R error of 0.09. LSIB has a mean orientation error of 13^o, and a mean R error of 0.11. FMSI is consistently very accurate (error $\leq 5^o$ for 90% of the tests) in favorable conditions, such as large data sets ($N = 300$) or small mechanism error (5^o). However, FMSI's estimates of R are poor for the axisymmetric case ($R = 0$ or $R = 1$).

The accuracy of both methods improves with increasing data set size, as one might expect, with the most improvement occurring between $N = 20$ and $N = 50$. The accuracy deteriorates with increasing mechanism error, as also might be expected. The accuracy of FMSI's results degrade more quickly with increasing mechanism error, making LSIB more accurate for data sets with error greater than $\sim 25^o$.

The two inversion techniques make different choices about the parameter to minimize and how to handle nodal plane ambiguity, but both sets of assumptions are apparently reasonable. The linearization scheme employed by LSIB appears not to have had a major adverse effect on the accuracy of the inversion results, even though the test data sets with uniformly distributed planes should have been particularly tough on the linearization approximation.

The levels of accuracy for LSIB and FMSI indicate that the difference in confidence region size does not stem from a difference in accuracy. One might expect the more accurate method to have the smaller confidence regions, but in this case, it has the larger. This further suggests that either FMSI's confidence regions are too large or LSIB's are too small.

A.4.2 Confidence Regions

In most tests of the confidence regions (Figure A.5, Figure A.6, Figure A.7), LSIB's uncertainty estimates are the more appropriate. The correct stress state generally falls into the $X\%$ confidence region for $(X\pm10)\%$ of the inversions, indicating that LSIB's confidence regions are approximately correct. The exception is for large data sets, $N = 300$, in which case the confidence regions are much too small (Figure A.5). The appropriateness of LSIB's confidence regions does not degrade with increasing mechanism error (Figure A.6), indicating that the bootstrap technique successfully incorporates data errors into the uncertainty estimates.

In most cases, FMSI's confidence regions are much too large, with the correct stress state falling within the $X\%$ confidence region for $\gg X\%$ of the inversions. For example, the given 68% confidence regions often contain the correct result 90-95% of the time. In the axisymmetric case ($R = 0$ or $R = 1$), FMSI's confidence regions are apparently too small when all four model parameters are considered (Figure A.7). However, when only the stress orientations are considered, the confidence regions appear more appropriate. This, along with the observation that FMSI determines axisymmetric values of R with poor accuracy (Figure A.4), indicates that the problem is primarily incorrect estimation of R.

A.5 Discussion

From the above results, it is apparent that the two inversion methods have different strengths and weaknesses. FMSI usually provides more accurate estimates of stress orientation, especially in favorable conditions such as large data sets and high-quality focal mechanisms. LSIB, while less accurate on average, provides a better estimate of uncertainty and is more accurate for data sets containing large errors. Which method is best to use for a particular study depends on the quality of the data and the relative importance of accuracy and error estimation.

An ideal inversion method would combine the strengths of both: a grid search

over parameter space and a non-parametric approach to error estimation. Unfortunately, non-parametric techniques such as bootstrap resampling require repeating the inversion hundreds or thousands of times, and the grid search method is very slow. As computational speed increases, combining grid search with non-parametric error estimation will become more practical. Another possibility is to speed up the search over parameter space using techniques such as genetic algorithms [*Michael*, 2000].

A.5.1 Problems with LSIB

The somewhat lower average accuracy of LSIB may be due in part to the approximation of equal shear stress on all fault planes used in the linearization of the problem. Uniformly distributed fault planes violate this approximation in the extreme, so LSIB's results for the test data sets probably represent the worst-case accuracy. LSIB's handling of the fault plane ambiguity problem, which considers the auxiliary planes only in error estimation, may also adversely affect the inversion accuracy if the data set contains a significant fraction of incorrectly picked planes. Surprisingly, the accuracy for very noisy data is quite good, with average error less than that of FMSI and much less than the data error.

LSIB's confidence regions for large data sets ($N = 300$) are too small. This may be because larger data sets often contain a number of similar focal mechanisms, which are essentially repeated data. These same data will also be repeated in the resampled data sets more often than other data. The full range of population samples, however, should repeat all data with similar frequency.

More representative resampled data sets can be made by sorting the mechanisms into bins based on strike, dip and rake. Only one mechanisms from each non-empty bin is used in the base data set which is resampled during bootstrap error estimation. Although the base data sets contain <300 events, each resampled data set still contains 300 events. The confidence regions found using the modified resampling method are of more appropriate size (Figure A.8).

A.5.2 Problems with FMSI

FMSI's confidence regions are systematically too large. However, it is presently unclear what may be wrong. Here I discuss the validity of the two major assumptions, normally distributed mechanism misfits due to data errors and a minimum observed misfit equal to the expected value of misfit for the best-fit stress state. I also consider the effects of finite grid spacing and nodal plane ambiguity.

Error Distribution

It may be unrealistic to assume that the individual event misfits due to data errors are normally distributed, while the data errors themselves are exponentially distributed. From the procedure followed in Equations A.6-A.11, we see that

$$\frac{\Sigma_X}{\Sigma_{min}} \approx \frac{z_X\sigma + E[m]}{E[m]} \tag{A.12}$$

and that Σ_X will scale with the ratio $\sigma/E[m]$. In the case of normally-distributed misfits,

$$\frac{\sigma}{E[m]} = \frac{(1-2/\pi)^{1/2}N^{1/2}}{(2/\pi)^{1/2}N} \approx 0.76N^{-1/2}. \tag{A.13}$$

In the case of exponentially-distributed misfits, I find numerically that

$$\frac{\sigma}{E[m]} \approx \frac{(0.5N)^{1/2}}{0.7N} \approx N^{-1/2}. \tag{A.14}$$

Assuming an exponential distribution of misfits would therefore result in larger Σ_X and larger confidence regions.

The distribution of event misfits for the correct stress state need not be the same as the mechanism error distribution. For each event, the misfit for the correct stress state cannot be greater than the mechanism error. However, it can be less if the given mechanism is closer to another acceptable mechanism than to the correct mechanism for that event. I estimate the distribution of event misfits for the synthetic data sets by finding the minimum rotation angle between each mechanism and any focal mecha-

nism compatible with the correct stress state. Choosing misfits from this distribution, I find numerically that

$$\frac{\sigma}{E[m]} \approx \frac{(0.6N)^{1/2}}{N} \approx 0.77N^{-1/2}. \tag{A.15}$$

Although the misfits are not normally distributed, the ratio $\sigma/E[m]$, which controls Σ_X and the size of the confidence regions, is very similar to the ratio $\sigma/E[m]$ for a normal distribution. This implies that the assumption of a normal misfit distribution, while not strictly correct, is not the cause of the large confidence regions.

Expected Misfit

The computation of the threshold value of the confidence region, Σ_X, is based on the assumption that the minimum observed total misfit, Σ_{min}, is the expected value of the total misfit due to data errors for the correct stress state, $\sigma_{est}E[m]$. It is unrealistic to expect Σ_{min} to always exactly equal $\sigma_{est}E[m]$, but if Σ_{min} equals $\sigma_{est}E[m]$ on average, Σ_X should be correct on average as well. To explain confidence regions which are systematically too large, Σ_{min} would have to be systematically greater than $\sigma_{est}E[m]$. This would imply that something besides focal mechanism error is contributing to the misfits. Usually, one would conclude that model errors are being mapped into the misfits. However, since the synthetic data sets were created to be consistent with the model assumptions, this should not be the case. It is unclear what an additional source of error could be.

Finite Grid Spacing

The finite gridding of parameter space can affect the apparent appropriateness of the uncertainty estimates in cases where the size of the grid spacing is larger than, or comparable to, the appropriate size of the $X\%$ confidence region. In this case, the $X\%$ confidence region may appear too large even though it encompasses only one grid point. This is not a general explanation for the large confidence regions, however, as the 68% and 95% confidence regions typically contain many grid points. Finite grid

spacing can explain the large confidence regions only for cases of very high accuracy ($N = 300$ or error $= 5^o$) or low levels of confidence.

Fault Plane Ambiguity

Fault plane ambiguity may be responsible for FMSI's difficulty in determining R in the axisymmetric case ($R = 0$ or $R = 1$.) Random slip orientations tend to result in $R \approx 0.5$. The introduction of incorrect data, such as the auxiliary planes of some events, may move the computed value of R towards the middle of its range. If only the correct fault planes are included in the data set, and the misfit is computed only for these planes, the accuracy of R and the appropriateness of the uncertainty estimates improve (Figure A.9, Figure A.10). In general, however, modifying FMSI not to include auxiliary planes in the misfit computation does not improve its performance because the correct fault plane is usually not known.

A.6 Conclusions

The two most commonly used techniques for inverting earthquake focal mechanisms for stress orientation, FMSI [*Gephart and Forsyth*, 1984; *Gephart*, 1990a] and LSIB [*Michael*, 1984, 1987b], were tested on noisy synthetic data sets. Both techniques determine stress orientation accurately. FMSI is generally more accurate for high-quality data, while LSIB is more accurate for very noisy data. The confidence regions produced by LSIB are usually approximately the right size, while those of FMSI are usually too large.

The results for the synthetic data sets indicate that the confidence regions produced by LSIB should be appropriate for real data sets as well, as long as the model assumptions of homogeneous stress and slip in the direction of resolved shear stress generally hold. The numerous stress field variations which have previously been observed in southern California [*Michael*, 1987b; *Jones*, 1988; *Hauksson*, 1990, 1994; *Kerkela and Stock*, 1996], and the stress field variations reported in Chapters 1, 2, and 3, which are significant with respect to LSIB's uncertainty estimates, are therefore

larger than the true inversion uncertainty and probably represent real signals.

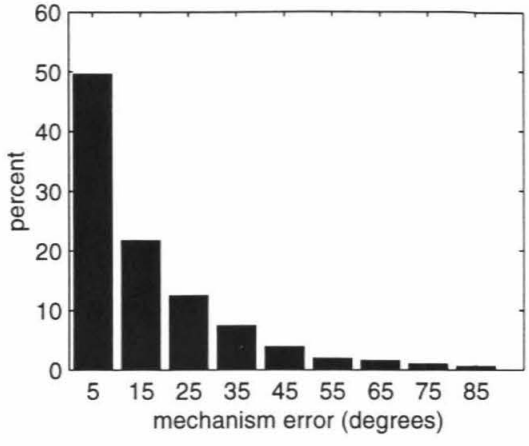

Figure A.1: Histogram of the errors in first-motion focal mechanisms resulting from polarity and takeoff angle errors. Forty-one diverse focal mechanisms were chosen, and first-motion polarities for each were assigned to stations using the station distribution of Southern California Seismic Network (SCSN) stations for 41 actual southern California events. Random errors in polarity and in takeoff angle (i.e., in event location or velocity model) were added. Each first-motion observation has a 20% chance of being reversed. The error in azimuth to each station is normally distributed with a standard deviation of 2^o, and the error in takeoff angle is normally distributed with a standard deviation of 10^o. New focal mechanisms were determined using the FPFIT software package [*Reasenberg and Oppenheimer*, 1985], and the mechanism error computed by determining the minimum rotation angle between the computed and correct mechanisms. This was repeated 100 times for the 41-event data set, and a histogram of mechanism error compiled. Note that the mechanism errors resemble an exponential distribution, not a normal distribution.

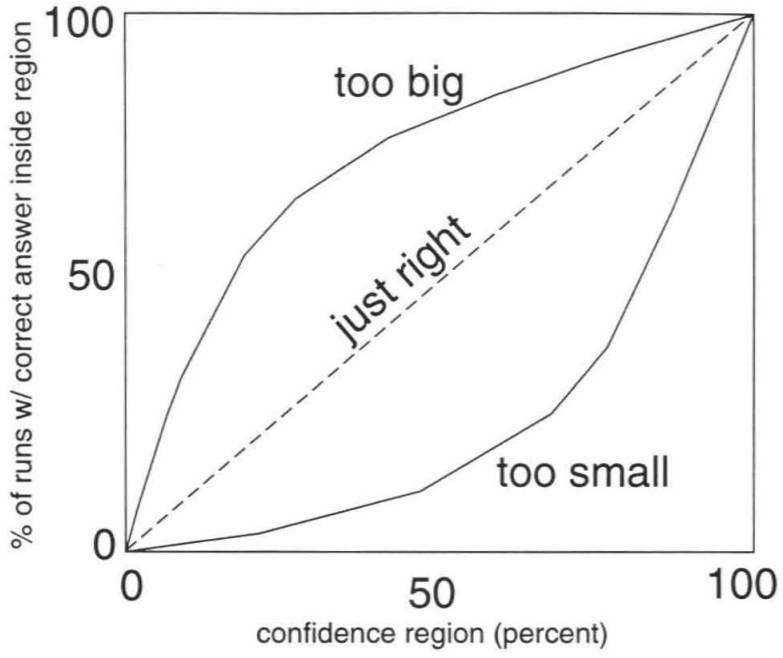

Figure A.2: An illustrative plot of the number of times the correct stress state falls within a given confidence region versus the percent confidence level. If the uncertainty estimates are correct, the plot should approximate a straight line. If the plot falls above this line, this means that the correct answer falls within the $X\%$ confidence region $\gg X\%$ of the time and the confidence regions are too big. Similarly, if the plot falls below the line, the correct answer falls within the $X\%$ confidence region $\ll X\%$ of the time and the confidence regions are too small.

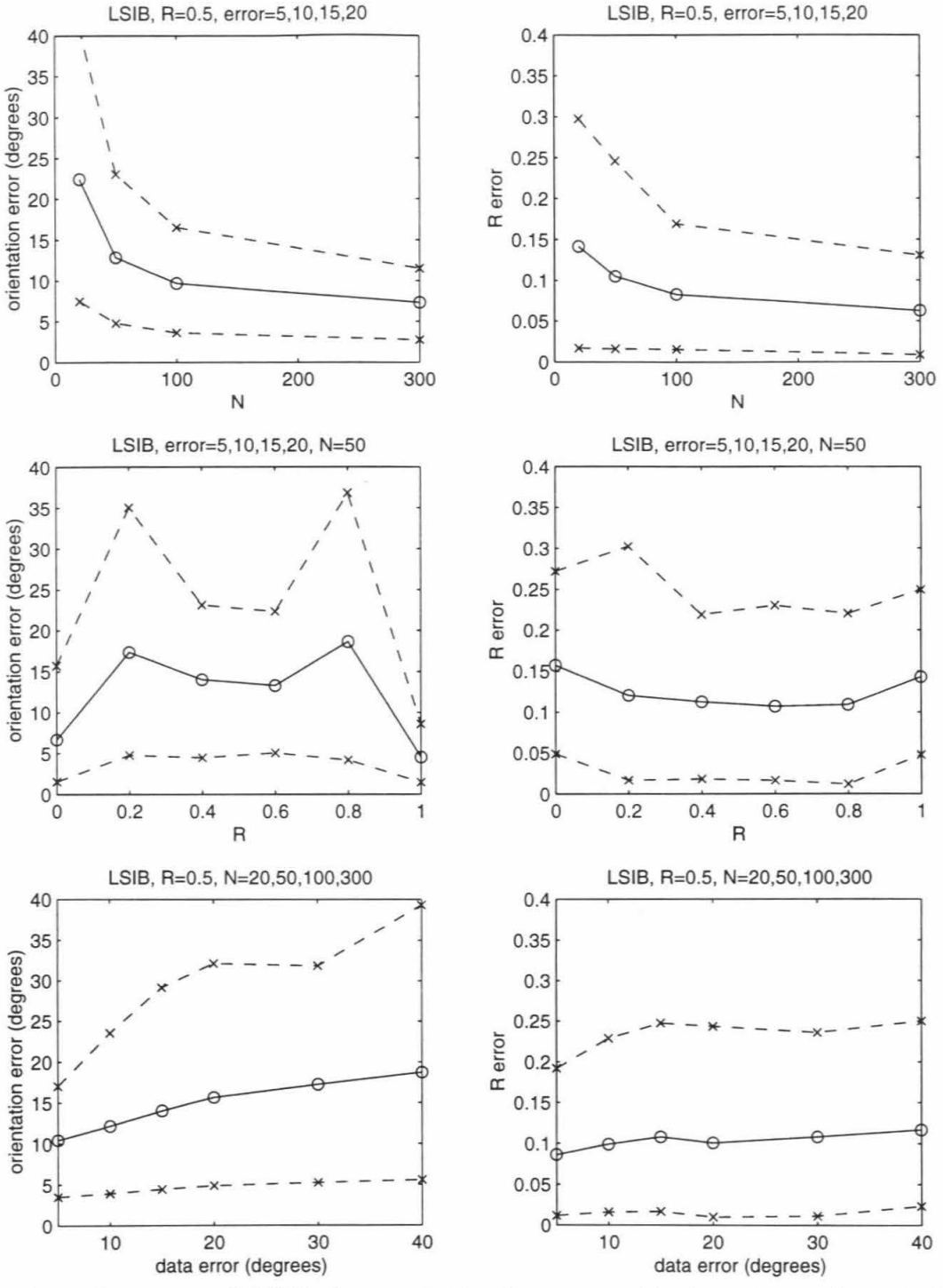

Figure A.3: Accuracy of LSIB, for synthetic data sets with the given values of N (data set size), R, and mechanism error. There are 50 data sets for each combination of parameter values listed. The circles connected by the solid line represent the mean error for the suite of data sets, the crosses connected by the dashed lines encompass the middle 80%.

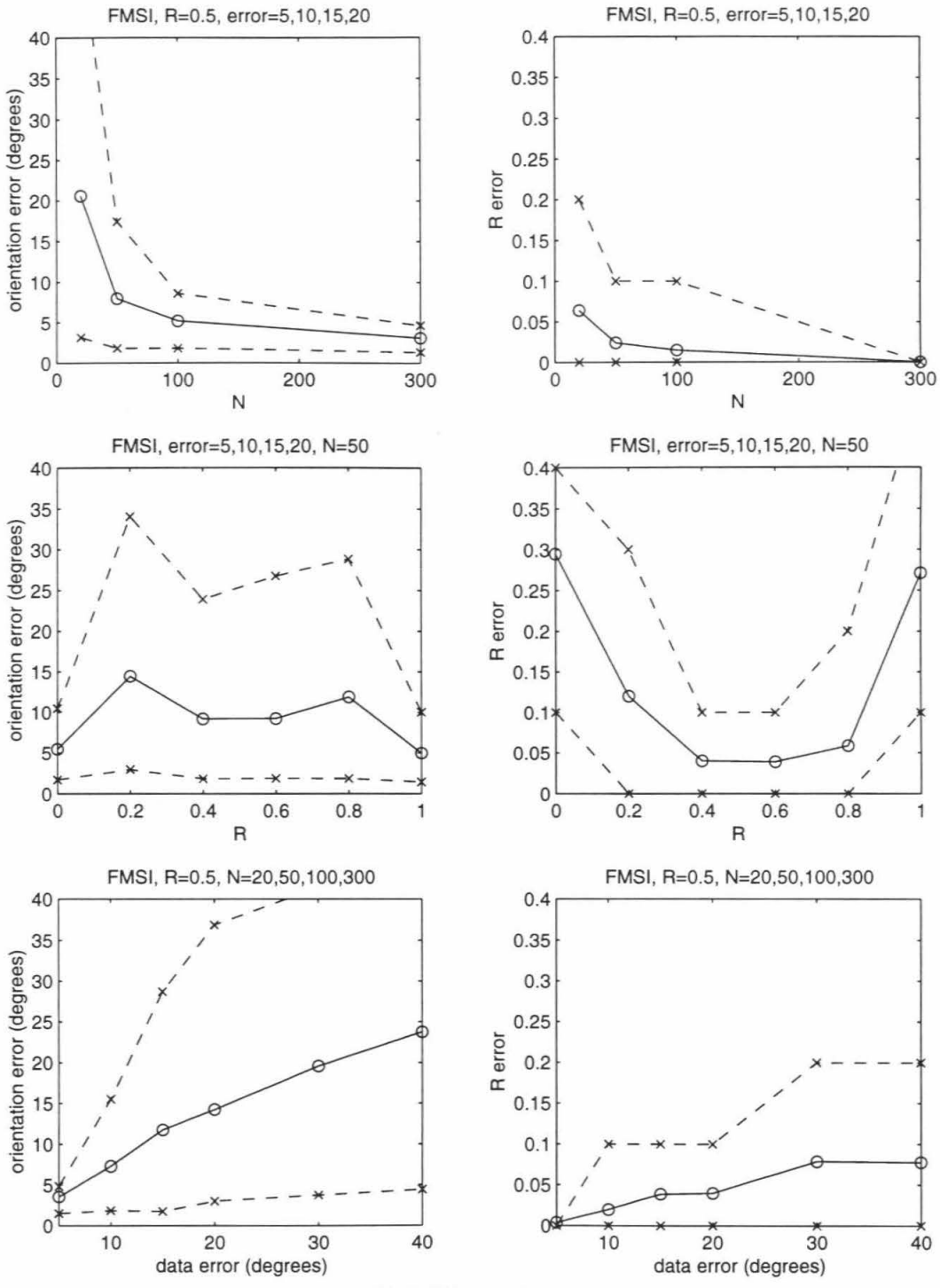

Figure A.4: Accuracy of FMSI, symbols as in Figure A.3.

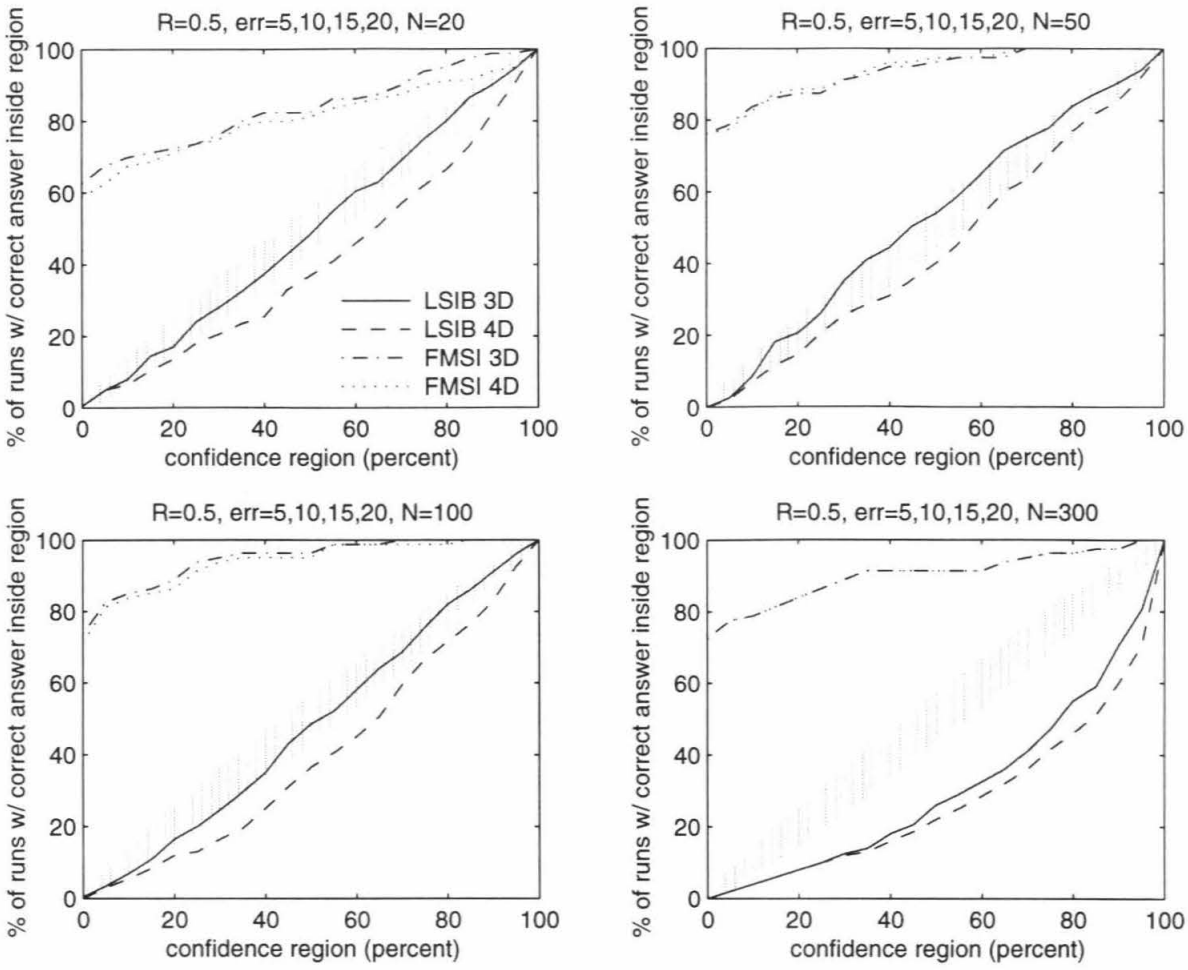

Figure A.5: Confidence region appropriateness for both inversion methods, for varying N (data set size.) The number of times the correct stress state falls within the $X\%$ confidence region is plotted as a function of X. If the confidence regions are appropriate, the function should fall within the shaded area. Results from an experiment with perfect confidence regions would have a 95% probability of falling within the shaded zone, which is the 95% confidence region of the binomial probability distribution for 200 trials with an $X\%$ probability of success each trial. If the confidence regions are too big or too small, the function will fall above or below the shaded area, respectively (see Figure A.2). There are 50 data sets for each combination of parameter values listed. The label 4D indicates that all four model parameters were considered; 3D, only principal axis orientations.

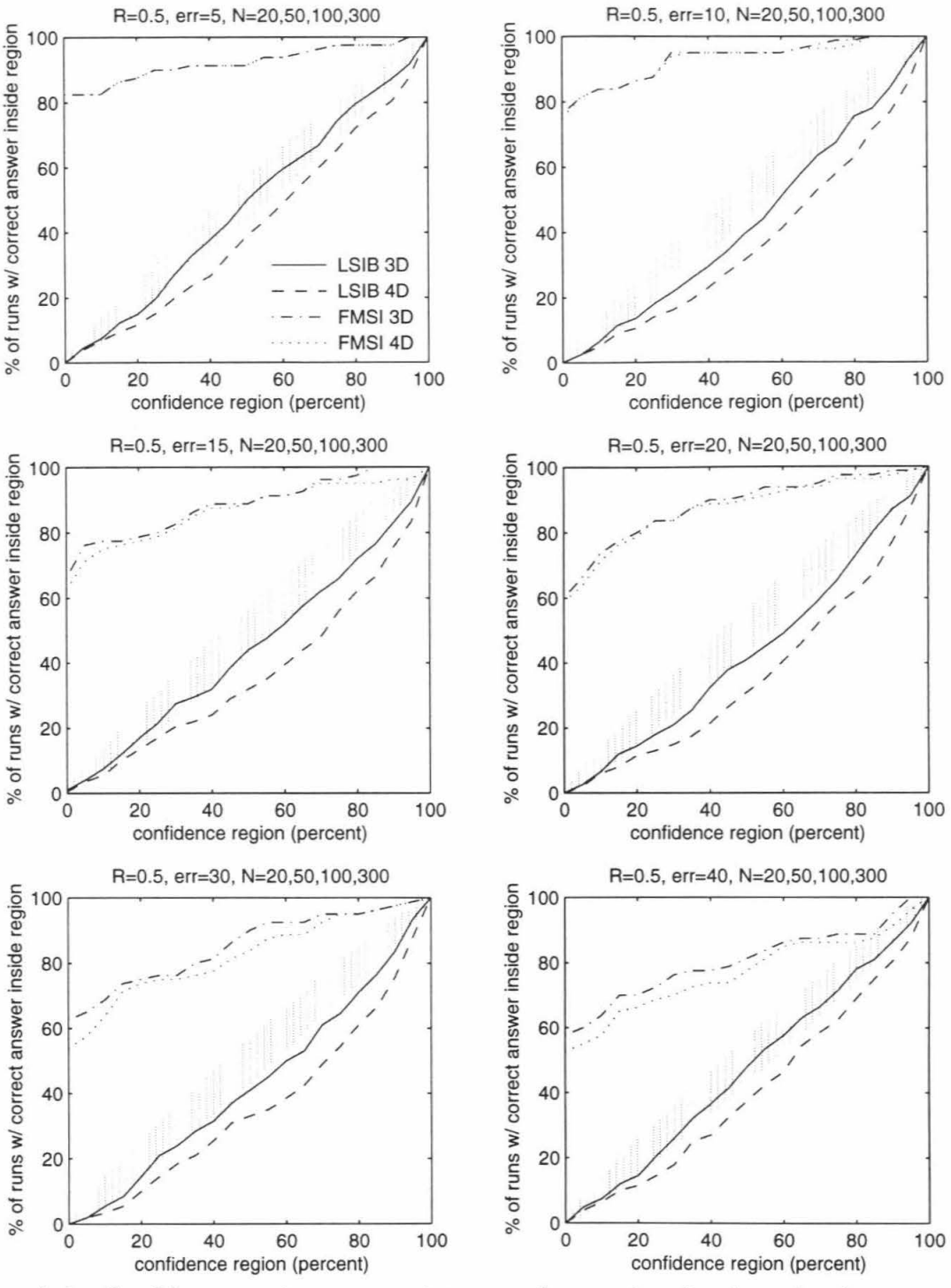

Figure A.6: Confidence region appropriateness, for varying focal mechanism error. Symbols as in Figure A.5.

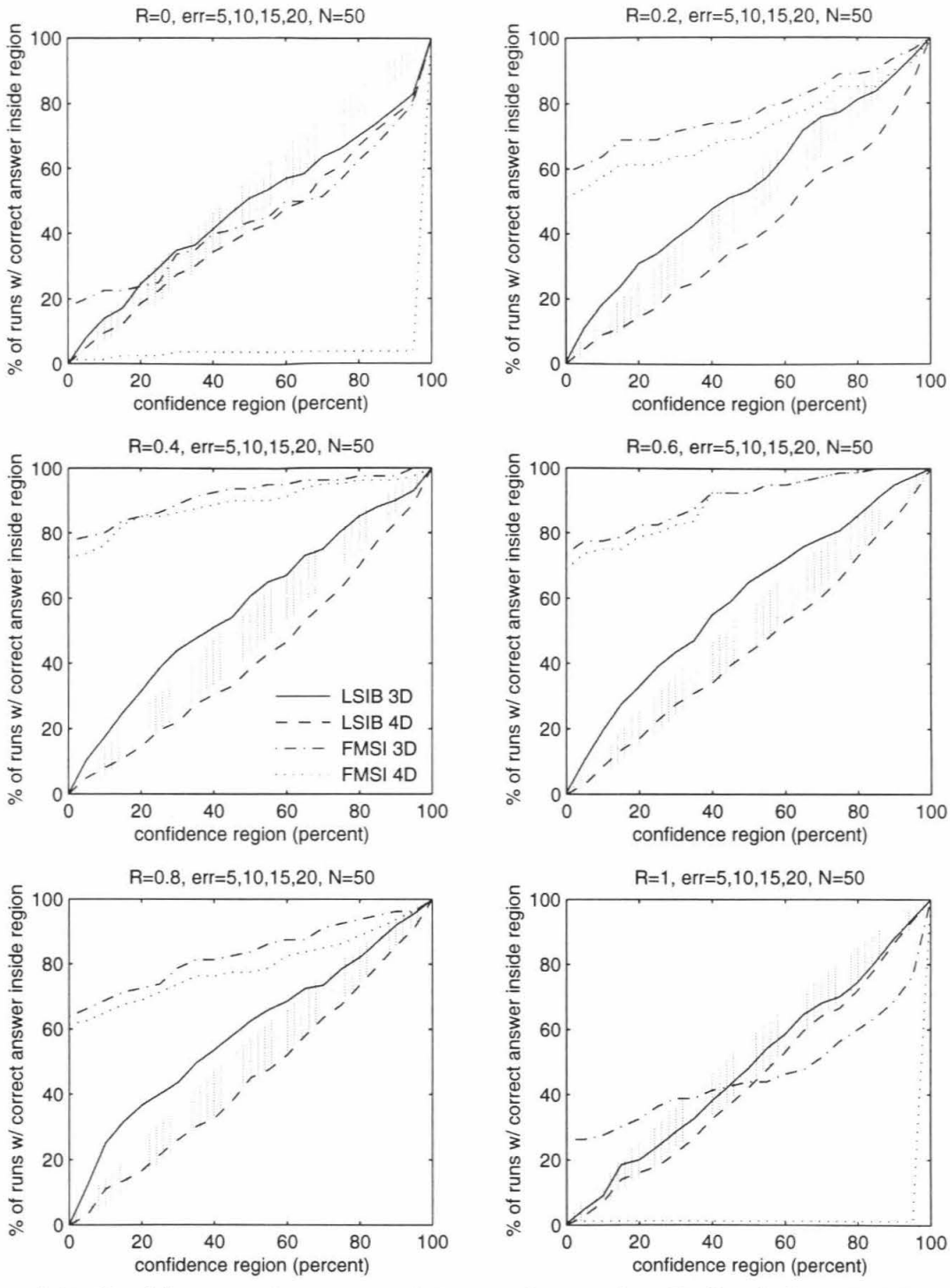

Figure A.7: Confidence region appropriateness, for varying R. Symbols as in Figure A.5.

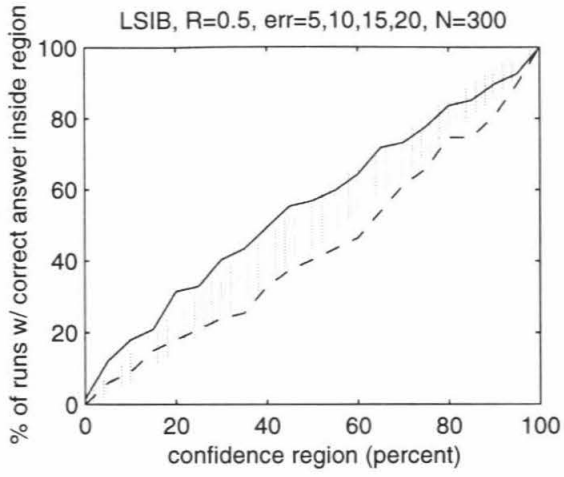

Figure A.8: Confidence region appropriateness for LSIB for $N = 300$ when a modified resampling method is used. The focal mechanisms are sorted into 10^o-wide bins based on strike, dip and rake. Only one mechanism from each non-empty bin is used in the base data set which is resampled during bootstrap error estimation. Although the base data set contains <300 events, each resampled data set still contains 300 events. Symbols as in Figure A.5.

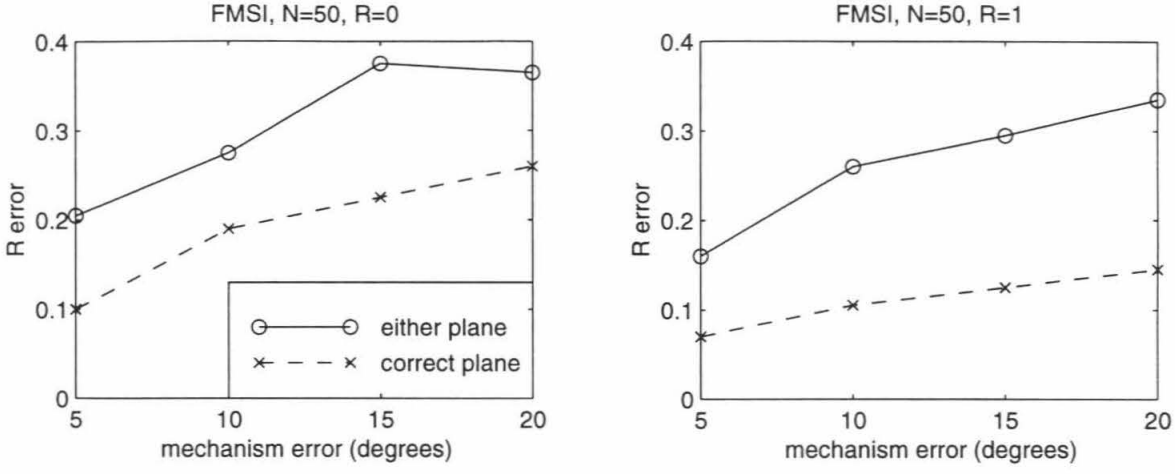

Figure A.9: Average accuracy of R determined by FMSI, for axisymmetric stress tensors (R =0 and R =1) when the fault plane is ambiguous (circles and solid line) and known (crosses and dashed line). There are 50 data sets for each level of error.

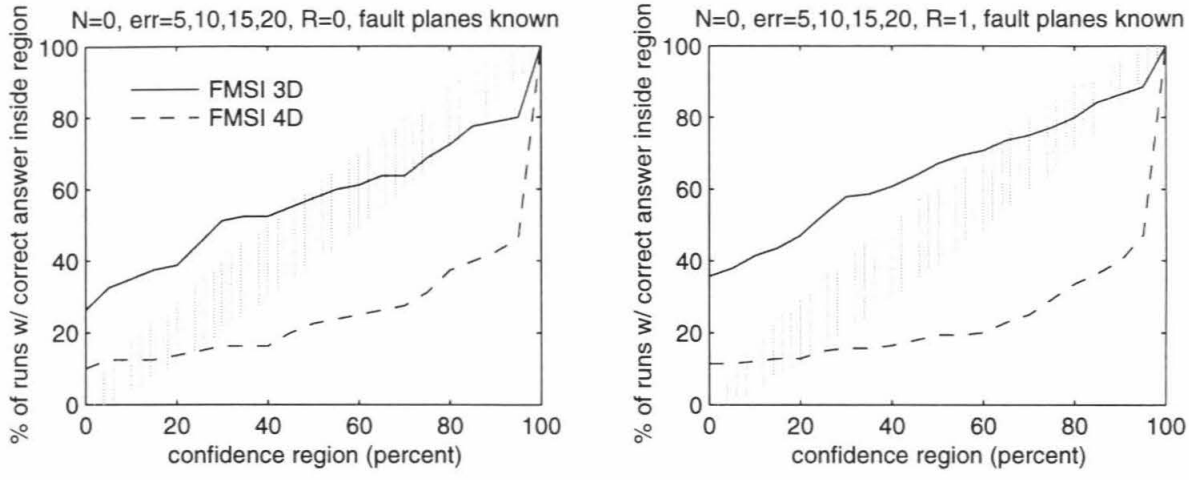

Figure A.10: Confidence region appropriateness for FMSI for the axisymmetric case when the fault plane in known. Solid line, 3D; dashed line, 4D. All other symbols as in Figure A.5. There are 50 data sets for each level of error.

Bibliography

Abercrombie, R., Earthquake source scaling relationships from -1 to 5 M_L, *J. Geophys. Res.*, *100*, 24015–24036, 1995.

Abercrombie, R., and P. Leary, Source parameters of small earthquakes recorded at 2.5 km depth, Cajon Pass, southern California: implications for earthquake scaling, *Geophys. Res. Lett.*, *20*, 1511–1514, 1993.

Abers, G. A., and J. W. Gephart, Stress variations in southern California determined by direct inversion of seismic first motions (MOTSI), *Eos Trans. AGU*, *78*, F451, 1997.

Anderson, E. M., *The Dynamics of Faulting and Dyke Formation with Applications to Britain*, Oliver and Boyd, Edinburgh, 1951.

Anderson, G., and H. Johnson, A new statistical test for static stress triggering: Application to the 1987 Superstition Hills earthquake sequence, *J. Geophys. Res.*, *104*, 20153–20168, 1999.

Andrews, D. J., and Y. Ben-Zion, Wrinkle-like slip pulse on a fault between different materials, *J. Geophys. Res.*, *102*, 552–571, 1997.

Archuleta, R. J., E. Cranswick, C. Mueller, and P. Spudich, Source parameters of the 1980 Mammoth Lakes, California, earthquake sequence, *J. Geophys. Res.*, *87*, 4595–4607, 1982.

Argus, D. F., et al., Shortening and thickening of metropolitan Los Angeles measured and inferred by using geodesy, *Geology*, *27*, 703–706, 1999.

Bakun, W. H., and M. McLaren, Microearthquakes and the nature of the creeping-to-locked transition of the San Andreas fault zone near San Juan Bautista, California, *Bull. Seism. Soc. Am.*, *74*, 235–254, 1984.

Bawden, G., Source parameters for the 1952 Kern County earthquake, California: A joint inversion of leveling and triangulation observations, *submitted to J. Geophys. Res.*, 2000.

Beeler, N. M., R. W. Simpson, and D. A. Lockner, Loading faults to Coulomb failure, *Eos Trans. AGU*, *79*, F639, 1998.

Bellier, O., and M. L. Zoback, Recent state of stress change in the Walker Lane zone, western Basin and Range province, United States, *Tectonics*, *14*, 5564–593, 1995.

Beroza, G. C., and M. D. Zoback, Mechanism diversity of the Loma Prieta aftershocks and the mechanics of mainshock-aftershock interaction, *Science*, *259*, 210–213, 1993.

Boatwright, J., A spectral theory for circular seismic sources: simple estimates of source dimension, dynamic stress drop and radiated seismic energy, *Bull. Seism. Soc. Am.*, *70*, 1–25, 1980.

Brudy, M., M. D. Zoback, K. Fuchs, F. Rummel, and J. Baumgartner, Estimation of the complete stress tensor to 8 km depth in the KTB scientific drill holes: Implications for crustal strength, *J. Geophys. Res.*, *102*, 18453–18475, 1997.

Brune, J. N., Tectonic stress and the spectra of seismic shear waves from earthquakes, *J. Geophys. Res.*, *75*, 4997–5009, 1970.

Brune, J. N., T. L. Henyey, and R. F. Roy, Heat flow, stress, and rate of slip along the San Andreas fault, California, *J. Geophys. Res.*, *74*, 3821–3827, 1969.

Byerlee, J. D., Friction of rock, *Pure Appl. Geophys.*, *116*, 615–626, 1978.

Castillo, D. A., and M. D. Zoback, Systematic stress variations in the southern San Joaquin Valley and along the White Wolf Fault; implications for the rupture mechanics of the 1952 Ms 7.8 Kern County earthquake and contemporary seismicity, *J. Geophys. Res.*, *100*, 6249–6264, 1995.

Deng, J., and L. R. Sykes, Evolution of the stress field in southern California and triggering of moderate-size earthquakes: A 200-year perspective, *J. Geophys. Res.*, *102*, 9859–9886, 1997.

Dokka, R. K., and C. J. Travis, Late Cenozoic strike-slip faulting in the Mojave Desert, California, *Tectonics*, *9*, 311–340, 1990.

Ellsworth, W. L., Earthquake history, 1769-1989, in *The San Andreas Fault System, California, USGS Prof. Paper 1515*, edited by R. E. Wallace, pp. 153–187, U. S. Government Printing Office, Washington, DC, 1990.

Feng, Q., and J. E. Ebel, Determination of rupture duration and stress drop for earthquakes in New England, *Seism. Res. Lett.*, *67*, 38–51, 1996.

Fletcher, J. B., J. Boatwright, L. Haar, T. C. Hanks, and A. McGarr, Source parameters for aftershocks of the Oroville, California, earthquake, *Bull. Seism. Soc. Am.*, *74*, 1101–1123, 1984.

Frankel, A., and H. Kanamori, Determination of rupture duration and stress drop for earthquakes in southern California, *Bull. Seism. Soc. Am.*, *73*, 1527–1551, 1983.

Frankel, A., D. Carver, E. Cranswick, M. Meremonte, T. Bice, and D. Overturf, Site response for Seattle and source parameters of earthquakes in the Puget Sound region, *Bull. Seism. Soc. Am.*, *89*, 468–483, 1999.

Fuis, G. S., and W. D. Mooney, Lithospheric structure and tectonics from seismic-refraction and other data, in *The San Andreas Fault System, California, USGS Prof. Paper 1515*, edited by R. E. Wallace, pp. 207–236, U. S. Government Printing Office, Washington, DC, 1990.

Fujita, E., Y. Iio, and E. Fukuyama, Stress drop distribution of the aftershocks of the 1993 Hokkaido-Nansei-Oki earthquake, *Geophys. Res. Lett.*, *22*, 3083–3086, 1995.

Gephart, J. W., FMSI: A FORTRAN porgram for inverting fault/slikenside and

earthquake focal mechanism data to obtain the regional stress tensor, *Computers and Geosciences*, *16*, 953–989, 1990a.

Gephart, J. W., Stress and the direction of slip on fault planes, *Tectonics*, *9*, 845–858, 1990b.

Gephart, J. W., and D. W. Forsyth, An improved method for determining the regional stress tensor using earthquake focal mechanism data: Application to the San Fernando earthquake sequence, *J. Geophys. Res.*, *89*, 9305–9320, 1984.

Guo, H., A. L. Lerner-Lam, W. Menke, and S. E. Hough, Empirical Green's function study of Loma Prieta aftershocks; determination of stress drop, *U. S. Geol. Surv. Prof. Paper*, *1550-D*, D105–D119, 1997.

Hardebeck, J. L., and E. Hauksson, Role of fluids in faulting inferred from stress field signatures, *Science*, *285*, 236–239, 1999.

Hardebeck, J. L., J. J. Nazareth, and E. Hauksson, The static stress change triggering model: Constraints from two southern California aftershock sequence, *J. Geophys. Res.*, *103*, 24427–24437, 1998.

Hartse, H. E., M. C. Fehler, R. C. Aster, J. S. Scott, and F. L. Vernon, Small-scale stress heterogeneity in the Anza seismic gap, southern California, *J. Geophys. Res.*, *99*, 6801–6818, 1994.

Hauksson, E., Earthquakes, faulting, and stress in the Los Angeles basin, *J. Geophys. Res.*, *95*, 15365–15394, 1990.

Hauksson, E., State of stress from focal mechanisms before and after the 1992 Landers earthquake sequence, *Bull. Seism. Soc. Am.*, *84*, 917–934, 1994.

Hauksson, E., Crustal structure and seismicity distribution adjacent to the Pacific and North America plate boundary in Southern California, *J. Geophys. Res.*, *105*, 13875–13903, 2000.

Hauksson, E., and J. Haase, Three-dimensional V_p and V_p/V_s velocity model of the Los Angeles basin and central Transverse Ranges, California, *J. Geophys. Res.*, *102*, 5423–5453, 1997.

Hauksson, E., L. M. Jones, K. Hutton, and D. Eberhart-Phillips, The 1992 Landers earthquake sequence: Seismological observations, *J. Geophys. Res.*, *98*, 19835–19858, 1993.

Hauksson, E., L. M. Jones, and K. Hutton, The 1994 Northridge earthquake sequence in California: Seismological and tectonic aspects, *J. Geophys. Res.*, *100*, 12335–12355, 1995a.

Hauksson, E., et al., Preliminary report on the 1995 Ridgecrest earthquake sequence in eastern California, *Seismological Research Letters*, *66*, 54–60, 1995b.

Hearn, E. H., and E. D. Humphreys, Kinematics of the southern Walker Lane Belt and motion of the Sierra Nevada block, California, *J. Geophys. Res.*, *103*, 27033–27049, 1998.

Heaton, T. H., Evidence for and implications of self-healing pulses of slip in earthquake rupture, *Phys. Earth Planet. Inter.*, *64*, 1–20, 1990.

Hickman, S. H., M. D. Zoback, and J. H. Healy, Conitnuation of a deep borehole stress measurement profile near the San Andreas Fault 1. hydraulic fracturing stress measurements at Hi Vista, Mojave Desert, California, *J. Geophys. Res.*, *93*, 15183–15195, 1988.

Horiuchi, S., G. Rocco, and A. Hasegawa, Discrimination of fault planes from auxiliary planes based on simultaneous determination of stress tensor and a large number of fault plane solutions, *J. Geophys. Res.*, *100*, 8327–8338, 1995.

Hough, S. E., L. Seeber, A. L. Lerner-Lam, J. C. Armbruster, and H. Guo, The 1989 Loma Prieta, California, earthquake and its effects, *Bull. Seism. Soc. Am.*, *81*, 1737–1753, 1991.

Hubbert, M. K., and W. W. Rubey, Mechanics of fluid-filled porous solids and its application to overthrust faulting, part 1: Role of fluid pressure in mechanics of overthrust faulting, *Bull. Geol. Soc. Am.*, *70*, 115–166, 1959.

Ichinose, G. A., K. D. Smith, and J. G. Anderson, Source parameters of the 15 November 1995 Border Town, Nevada, earthquake sequence, *Bull. Siesm. Soc. Am.*, *87*, 652–667, 1997.

Jennings, P., Fault map of California with volcanoes, thermal springs and thermal wells, 1:750,000 scale, in *Geol. Data Map 1*, Calif. Div. of Mines and Geol., Sacramento, CA, 1975.

Johnson, H. O., D. C. Agnew, and F. K. Wyatt, Present-day crustal deformation in southern California, *J. Geophys. Res.*, *99*, 23951–23974, 1994.

Jones, L., and D. V. Helmberger, Seismicity and stress-drop in the eastern Transverse Ranges, southern California, *Geophys. Res. Lett.*, *23*, 233–236, 1996.

Jones, L. E., and D. V. Helmberger, Earthquake source parameters and fault kinematics in the eastern California shear zone, *Bull. Seism. Soc. Am.*, *88*, 1337–1352, 1998.

Jones, L. M., Focal mechanisms and the state of stress on the San Andreas Fault in southern California, *J. Geophys. Res.*, *93*, 8869–8891, 1988.

Jones, L. M., L. K. Hutton, D. D. Given, and C. R. Allen, The North Palm Springs, California, earthquake sequence of July 1986, *Bull. Seism. Soc. Am.*, *76*, 1830–1837, 1986.

Kanamori, H., and D. L. Anderson, Theoretical basis of some empirical relations in seismology, *Bull. Seism. Soc. Am.*, *65*, 1073–1095, 1975.

Kerkela, S., and J. M. Stock, Compression directions north of the San Fernando Valley determined from borehole breakouts, *Geophys. Res. Lett.*, *23*, 3365–3368, 1996.

Kilb, D., M. Ellis, J. Gomberg, and S. Davis, On the origin of diverse aftershock mechanisms following the 1989 Loma Prieta earthquake, *Geophys. J. Int.*, *128*, 557–570, 1997.

King, G. C. P., R. S. Stein, and J. Lin, Static stress changes and the triggering of earthquakes, *Bull. Seism. Soc. Am.*, *84*, 935–953, 1994.

Lachenbruch, A. H., and J. H. Sass, Heat flow from Cajon Pass, fault strength, and tectonic implications, *J. Geophys. Res.*, *97*, 4995–5015, 1992.

Lindley, G. T., and R. J. Archuleta, Earthquake source parameters and the frequency dependence of attenuation at Coalinga, Mammoth Lakes, and the Santa Cruz Mountains, California, *J. Geophys. Res.*, *97*, 14137–14154, 1992.

Lisowski, M., J. C. Savage, and W. H. Prescott, The velocity field along the San Andreas Fault in central and southern California, *J. Geophys. Res.*, *96*, 8369–8389, 1991.

Liu, Y., S. Crampin, and R. E. Abercrombie, Shear-wave anisotropy and the stress field from borehole recordings at 2.5 km depth at Cajon Pass, *Geophys. J. Int.*, *129*, 439–449, 1997.

Lund, B., and R. Slunga, Stress tensor inversion using detailed microearthquake information and stability constraints: Application to Olfus in southwest Iceland, *J. Geophys. Res.*, *104*, 14947–14964, 1999.

Magistrale, H., and C. Sanders, Evidence from precise earthquake hypocenters for segmentation of the San Andreas Fault in San Gorgonio Pass, *J. Geophys. Res.*, *101*, 3031–3044, 1996.

Melosh, H. J., Dynamical weakening of faults by acoustic fluidization, *Nature*, *379*, 601–606, 1996.

Michael, A. J., Determination of stress from slip data: Faults and folds, *J. Geophys. Res.*, *89*, 11517–11526, 1984.

Michael, A. J., Use of focal mechanisms to determine stress: A control study, *J. Geophys. Res.*, *92*, 357–368, 1987a.

Michael, A. J., Stress rotation during the Coalinga aftershock sequence, *J. Geophys. Res.*, *92*, 7963–7979, 1987b.

Michael, A. J., Spatial variations in stress within the 1987 Whittier Narrows, California, aftershock sequence: new techniques and results, *J. Geophys. Res.*, *96*, 6303–6319, 1991.

Michael, A. J., A genetic algorithm stress inversion method, *Seism. Res. Lett.*, *71*, 228, 2000.

Moore, D. E., D. A. Lockner, R. Summers, S. Ma, and J. D. Byerlee, Strength of chrysotile-serpentinite gouge under hydrothermal conditions; can it explain a weak San Andreas Fault?, *Geology*, *24*, 1041–1044, 1996.

Mori, J., H. Kanamori, and R. Abercrombie, Scaling of stress drop and energy from Northridge aftershocks, *Eos Trans. AGU*, *77*, F481, 1996.

Morrow, C., B. Radney, and J. Byerlee, Frictional strength and the effective pressure law of montmorillonite and illite clays, in *Fault Mechanics and Transport Properties of Rock*, edited by B. Evans and T.-F. Wong, pp. 69–88, Academic Press, San Diego, CA, 1992.

Mount, V. S., and J. Suppe, Present-day stress orientations adjacent to active strike-slip faults; California and Sumatra, *J. Geophys. Res.*, *97*, 11995–12013, 1992.

Nur, A., H. Ron, and G. C. Beroza, The nature of the Landers-Mojave earthquake line, *Science*, *261*, 201–203, 1993.

Okada, Y., Internal deformation due to shear and tensile faults in a half-space, *Bull. Seism. Soc. Am.*, *82*, 1018–1040, 1992.

O'Neill, M. E., Source dimensions and stress drops of small earthquakes near Parkfield, California, *Bull. Seism. Soc. Am.*, *74*, 27–40, 1984.

Parker, R. L., and M. K. McNutt, Statistics for the one-norm misfit measure, *J. Geophys. Res.*, *85*, 4429–4430, 1980.

Pollard, D. D., S. D. Saltzer, and A. M. Rubin, Stress inversion methods: are they based on faulty assumptions?, *J. Structural Geol.*, *15*, 1045–1054, 1993.

Press, W. H., B. P. Flannery, S. A. Teukolsky, and W. T. Vetterling, *Numerical Recipes: The Art of Scientific Computing*, Cambridge Univ. Press, Cambridge, UK, 1986.

Reasenberg, P., and D. Oppenheimer, FPFIT, FPPLOT and FPPAGE: FORTRAN computer programs for calculating and displaying earthquake fault-plane solutions, *U. S. Geol. Surv. Open File Rep.*, *85-730*, 109, 1985.

Reasenberg, P., and R. W. Simpson, Response of regional seismicity to the static stress change produced by the Loma Prieta earthquake, *Science*, *255*, 1687–1690, 1992.

Rice, J. R., Fault stress states, pore pressure distributions, and the weakness of the San Andreas Fault, in *Fault Mechanics and Transport Properties of Rock*, edited by B. Evans and T.-F. Wong, pp. 475–503, Academic Press, San Diego, CA, 1992.

Rice, J. R., and M. P. Cleary, Some basic stress diffusion solutions for fluid-saturated elastic porous media with compressible constituents, *Rev. Geophys.*, *14*, 227–241, 1976.

Scholz, C. H., Evidence for a strong San Andreas Fault, *Geology*, *28*, 163–166, 2000.

Scientists from the USGS, SCEC, and CDMG, Preliminary report on the 16 October 1999 M 7.1 Hector Mine, California, earthquake, *Seism. Res. Lett.*, *71*, 11–23, 2000.

Seeber, L., and J. G. Armbruster, The San Andreas Fault system through the Transverse Ranges as illuminated by earthquakes, *J. Geophys. Res.*, *100*, 8285–8310, 1995.

Shamir, G., and M. D. Zoback, Stress orientation profile to 3.5 km depth near the San Andreas Fault at Cajon Pass, California, *J. Geophys. Res.*, *97*, 5059–5080, 1992.

Shen-Tu, B., W. E. Holt, and A. J. Haines, The contemporary kinematics of the western United States determined from earthquake moment tensors, very long baseline interferometry, and GPS observations, *J. Geophys. Res.*, *103*, 18087–18117, 1998.

Sieh, K., et al., Near-field investigation of the Landers earthquake sequence, April to July 1992, *Science*, *260*, 171–176, 1993.

Simpson, R. W., Quantifying Anderson's fault types, *J. Geophys. Res.*, *102*, 17909–17919, 1997.

Smith, K. D., and K. F. Priestley, Aftershock stress release along active fault planes of the 1984 Round Valley, California, earthquake sequence applying a time-domain stress drop method, *Bull. Seism. Soc. Am.*, *83*, 144–159, 1993.

Sonder, L. J., Effects of density contrasts on the orientation of stresses in the lithosphere: Relation to principal stress directions in the Transverse Ranges, California, *Tectonics*, *9*, 761–771, 1990.

Song, X. J., and D. V. Helmberger, Northridge aftershocks, a source study with TERRAscope data, *Bull. Seism. Soc. Am.*, *87*, 1024–1034, 1997.

Stein, R. S., and W. Thatcher, Seismic and aseismic deformation associated with the 1952 Kern County, California, earthquake and relationship to the Quaternary history of the White Wolf Fault, *J. Geophys. Res.*, *86*, 4913–4928, 1981.

Stein, R. S., G. C. P. King, and J. Lin, Stress triggering of the 1994 M=6.7 Northridge, California, earthquake by its predecessors, *Science*, *265*, 1432–1435, 1994.

Stock, J. M., and J. H. Healy, Conitnuation of a deep borehole stress measurement profile near the San Andreas Fault 2. hydraulic fracturing stress measurements at Black Butte, Mojave Desert, California, *J. Geophys. Res.*, *93*, 15196–15206, 1988.

Thatcher, W., and T. C. Hanks, Source parameters of southern California earthquakes, *J. Geophys. Res.*, *78*, 8547–8576, 1973.

Toda, S., R. S. Stein, P. A. Reasenberg, J. H. Dieterich, and A. Yoshida, Stress transferred by the 1995 M_W=6.9 Kobe, Japan, shock: Effect on aftershocks and future earthquake probabilities, *J. Geophys. Res.*, *103*, 24543–24565, 1998.

Townend, J., and M. D. Zoback, Implications of earthquake focal mechanisms for the frictional strength of the San Andreas Fault system, *submitted to Geological Society of London Conference on Weak Faults*, 2000.

Turcotte, D. L., and G. Schubert, *Geodynamics: Applications of Continuum Physics to Geological Problems*, John Wiley & Sons, New York, 1982.

Unruh, J. R., R. J. Twiss, and E. Hauksson, Seismogenic deformation field in the Mojave block and implications for tectonics of the eastern California shear zone, *J. Geophys. Res.*, *101*, 8335–8361, 1996.

Wald, D. J., and T. H. Heaton, Spatial and temporal distribution of slip for the 1992 Landers, California earthquake, *Bull. Seism. Soc. Am.*, *84*, 668–691, 1994.

Wald, D. J., D. V. Helmberger, and S. H. Hartzell, Rupture process of the 1987 Superstition Hills earthquake from the inversion of strong-motion data, *Bull. Seism. Soc. Am.*, *80*, 1079–1098, 1990.

Wald, D. J., T. H. Heaton, and K. W. Hudnut, The slip history of the 1994 Northridge, California, earthquake determined from strong-motion, teleseismic, GPS, and leveling data, *Bull. Seism. Soc. Am.*, *86*, S49–S70, 1996.

Walls, C., T. Rockwell, K. Mueller, Y. Bock, S. Williams, J. Pfanner, J. Dolan, and P. Fang, Escape tectonics in the Los Angeles metropolitan region and implications for seismic risk, *Nature*, *394*, 356–360, 1998.

Weldon, R. J., and J. E. Springer, Active faulting near the Cajon Pass well, southern

California: Implications for the stress orientations near the San Andreas Fault, *Geophys. Res. Lett.*, *15*, 993–996, 1988.

Wilde, M., and J. Stock, Compression directions in southern California (from Santa Barbara to Los Angeles Basin) obtained from borehole breakouts, *J. Geophys. Res.*, *102*, 4969–4983, 1997.

Wyss, M., and Z. Lu, Plate boundary segmentation by stress directions: Southern San Andreas fault, California, *Geophys. Res. Lett.*, *22*, 547–550, 1995.

Yin, Z.-M., and G. C. Rogers, Rotation of the principal stress directions due to earthquake faulting and its seismological implications, *Bull. Seism. Soc. Am.*, *85*, 1513–1517, 1995.

Zhao, D., and H. Kanamori, The 1994 Northridge earthquake: 3-D crustal structure in the rupture zone and its relation to the aftershock locations and mechanisms, *Geophys. Res. Lett.*, *22*, 763–766, 1995.

Zhao, D., H. Kanamori, and D. Wiens, State of stress before and after the 1994 Northridge earthquake, *Geophys. Res. Lett.*, *24*, 519–522, 1997.

Zoback, M. D., and J. H. Healy, In situ stress measurements to 3.5 km depth in the Cajon Pass scientific research borehole: implications of the mechanics of crustal faulting, *J. Geophys. Res.*, *97*, 5039–5057, 1992.

Zoback, M. D., et al., New evidence on the state of stress of the San Andreas fault system, *Science*, *238*, 1105–1111, 1987.

Zoback, M. L., First- and second-order patterns of stress in the lithosphere: the World Stress Map project, *J. Geophys. Res.*, *975*, 11703–11728, 1992.